AD-E300529

(12)LEVEL III

DNA 4697T

ADA071368

DUST CLOUD MODELING AND PROPAGATION EFFECTS FOR RADAR AND COMMUNICATIONS CODES

General Electric Company — TEMPO

Center for Advanced Studies

816 State Street

Santa Barbara, California 93102

1 November 1978

Topical Report for Period 15 October 1977—1 November 1978

CONTRACT No. DNA 001-78-C-0043

DDC FILE COPY

D D C
RECEIVED
JUL 19 1979
RECEIVED
B

Prepared for

Director

DEFENSE NUCLEAR AGENCY

Washington, D. C. 20305

Destroy this report when it is no longer
needed. Do not return to sender.

REPORT DOCUMENTATION PAGE		READ INSTRUCTIONS BEFORE COMPLETING FORM
1. REPORT NUMBER DNA 4697T	2. GOVT ACCESSION NO.	3. RECIPIENT'S CATALOG NUMBER
4. TITLE (and Subtitle) DUST CLOUD MODELING AND PROPAGATION EFFECTS FOR RADAR AND COMMUNICATIONS CODES		5. TYPE OF REPORT & PERIOD COVERED Topical Report for Period 15 Oct 77—1 Nov 78
		6. PERFORMING ORG. REPORT NUMBER GE78TMP-81
7. AUTHOR(s) James H. Thompson		8. CONTRACT OR GRANT NUMBER(s) DNA 001-78-C-0043
9. PERFORMING ORGANIZATION NAME AND ADDRESS General Electric Company—TEMPO, Center for Advanced Studies, 816 State Street Santa Barbara, California 93102		10. PROGRAM ELEMENT, PROJECT, TASK AREA & WORK UNIT NUMBERS NWED Subtask S99QAXHE043-36
11. CONTROLLING OFFICE NAME AND ADDRESS Director Defense Nuclear Agency Washington, D.C. 20305		12. REPORT DATE 1 November 1978
		13. NUMBER OF PAGES 124
14. MONITORING AGENCY NAME & ADDRESS(if different from Controlling Office)		15. SECURITY CLASS (of this report) UNCLASSIFIED
		15a. DECLASSIFICATION DOWNGRADING SCHEDULE

16. DISTRIBUTION STATEMENT (of this Report)

Approved for public release; distribution unlimited.

17. DISTRIBUTION STATEMENT (of the abstract entered in Block 20, if different from Report)

18. SUPPLEMENTARY NOTES

19. KEY WORDS (Continue on reverse side if necessary and identify by block number)

Nuclear Weapons Effects   Nuclear Pedestal
Dust
Index of Refraction
Dielectric Constant
Nuclear Stem

20. ABSTRACT (Continue on reverse side if necessary and identify by block number)

This report describes new and improved models for dust generated by a low-altitude nuclear burst and the effects of this dust on radar and communications propagation. These models were developed for the WEPH code and are applicable for use in radar or communication codes. Developed in this report are:

- An improved Mie calculation,
- An extended model of the dust particle size distributions,

DD FORM 1473 EDITION OF 1 NOV 65 IS OBSOLETE

20. ABSTRACT (Continued)

- Methods for calculating the complex index of refraction for dust particles, and
- Dust models for the nuclear stem and pedestal regions.

CONTENTS

1

ILLUSTRATIONS

TABLES

SECTION 1
INTRODUCTION

Currently the weapon environment codes ROSCOE and WEPH include a model for the dust that is entrained by a near-surface nuclear fireball, which was developed originally for the RANC code. Since the development of the original model, additional theory and new experimental data from high explosive (HE) nuclear simulation test events have become available on dust. This report presents new and improved models for dust and propagation effects developed from the new information for the WEPH code. Although developed for the WEPH code, these models are applicable to other engineering codes modeling the effects of dust on radar and communications systems.

We begin by discussing possible areas for new and improved dust models. We then choose a number of these areas for detailed development in this report.

The Mie theory is used to calculate the extinction and backscatter coefficients for the dust particles. The Mie theory gives the exact solutions for the scattering and absorption of an electromagnetic wave incident on a uniform spherical particle. The solutions are given as infinite series of complex terms. The current Mie program in the systems codes uses a simple forward recursion scheme to calculate the successive Mie terms, which are summed until convergence is reached. However, in some cases the forward recursion technique is not stable. For example, when the incident radiation wavelength is small compared to the dust particle size, a large number of terms are required in the Mie series, and the forward recursion scheme can lose accuracy at the higher terms. For the largest dust particle now modeled—10 cm—the current Mie routine should be stable up to about 10 to 20 GHz. In the past most radar and

5

communications frequencies were lower than this, but some current systems of interest have frequencies well above this range.

For the WOE code, a different Mie technique was developed that is stable and avoids all errors inherent in the forward recursion technique. The method uses a stable backward recursion algorithm and uses a continued fraction scheme to accurately evaluate the starting high-order term. This technique is valid for all orders and can thus be used for any frequency and any particle size. The current Mie routine can be replaced by the new improved routine. The new routine is compact; the computer running time is only slightly longer than the old routine, but does require about 300 to 400 extra storage locations.

The WEPH code calculates only the attenuation of radiation passing through a dust region. Radar codes such as RANC and ROSCOE also calculate the backscatter, ie, clutter, due to the dust regions. The current model formulation for the clutter power due to scattering from a dust region is the following:

$$ C = \frac{P\lambda^2 F_I}{(4\pi)^2} \int_\phi \int_\theta \int_R \frac{G_T(\theta,\phi)G_R(\theta,\phi)}{4\pi R^2} \, \overline{\sigma}_B N_{TV} \, \sin\phi \; dR \; d\theta \; d\phi $$

where

P	= peak transmitter power (watts)
F_I	= pulse compression ratio, or pulse integration improvement factor
R	= range to the scattering region (m)
θ,ϕ	= angular coordinates with respect to the radar pointing direction (rad)
$G_T(\theta,\phi)$	= transmitter antenna gain function (including system loss factors)
$G_R(\theta,\phi)$	= receiver antenna gain function (including system loss factors)
N_{PT}	= volumetric number density of dust particles (m^{-3})
$\overline{\sigma}_B$	= average backscatter cross section per dust particle (m^2).

6

This current backscatter formulation implicitly assumes that the optical thickness of the dust cloud is very thin, the total one-way attenuation being less than about 1 to 2 dB. For typical fireball dust clouds and radar frequencies, the optical thinness assumption is valid. But the dust attenuation rapidly increases as the frequency increases, and, for some high-frequency radars, the dust clouds may no longer be optically thin. The full formulation for a region of any optical thickness is

$$C = \frac{P\lambda^2 F_I}{(4\pi)^2} \int_\phi \int_\theta \int_R \frac{G_T(\theta,\phi)G_R(\theta,\phi)}{4\pi R^2} \bar{\sigma}_B N_{TV} \, e^{-2\tau} \sin\phi \; dR \, d\theta \, d\phi$$

where

τ = optical depth at range R (due to all sources of attenuation).

If only the dust particles contribute to the attenuation, then

$$\tau = \int_0^R \bar{\sigma}_E N_{TV} dR' \quad ,$$

where

$\bar{\sigma}_E$ = average extinction cross section per dust particle (m^2).

The additional term $e^{-2\tau}$ in the clutter power equation accounts for the two-way attenuation of the radar beam to and from the scattering volume.

Although the extended formulation accounts for finite optical thicknesses, it is still a single scatter solution (as is the current back-scatter calculation). The contributions due to radiation that is multiple scattered are ignored. If the extinction is due almost entirely to scattering (little or no absorption), then for an optically thick region the backscatter due to the multiple scattered radiation can easily dominate the single scattered radiation. To first order, multiple scattering can be accounted for by adding a build-up factor, $B_U(\theta,\phi)$, to the single scatter integration (see, for example, Reference 1). $B_U(\theta,\phi)$ depends upon the optical thickness of the dust cloud in the direction corresponding to angular coordinates θ,ϕ, and upon the dust particle size distribution.

It would be a relatively easy task to include the e^{-2t} attenuation term in the backscatter formulation. It would require considerably more effort to include the multiple scatter build-up factor, $B_{U}(\cdot,\cdot)$.

The current dust model assumes that the size distribution of the dust particles can be described by a power law probability distribution with a power exponent of 4. Four is a typical value for dust particles from loose unconsolidated soils such as desert alluvium. Dust generated from a nuclear cratering explosion in rock and cohesive soils has a power exponent of about 3.5. Very fine soils may have a value near 5.

Another very common size distribution is the log-normal distribution. This distribution is often used for small particles and for condensates such as recondensed weapon debris and water droplets. Since the atmospheric nuclear test ban, a number of high explosive (HE) surface or shallow buried devices have been detonated to simulate nuclear explosions. Analysis of the dust particle size statistics from a number of these HE events and from previous nuclear test events indicates that the smaller dust particles follow a log-normal distribution, while the larger particles follow a power law distribution. A hybrid size distribution can be defined which consists of a log-normal joined to a power law distribution.

The complex index of refraction determines the scattering and absorption properties of a dust particle. The present dust model allows for three different soil types (wet clay, dry sand, and soil with an ice coating). A built-in table gives the refraction index for each soil type. These indices are taken as constants, independent of the incident radiation frequency. For optically thin dust regions and system frequencies less than about 10 GHz, a constant index of refraction is a reasonable approximation. For thick regions or higher frequencies, the frequency dependence of the index of refraction becomes important. The present model can be extended to include the frequency dependence.

The current dust model considers only the dust entrained in the fireball cloud. In addition to the fireball cloud, there are two other

regions that contain dust—the stem and pedestal regions. The stem is the column of dust reaching from the ground up toward the main cloud (the "stem" of the mushroom cloud). The pedestal is that relatively low lying dusty region extending outward along the surface from ground zero. The pedestal is formed by a combination of the thermal pulse from the fireball and the outrunning shock wave. There are photographic data from nuclear test events on the growth histories of the stem and pedestal regions. In addition there have been many theoretical investigations of both regions. There is now sufficient information available for the development of a dust model for these two subsidiary dust regions.

Consider a radiation ray path through a dust region. If the dust is distributed nonuniformly in the region, then the attenuation and back-scatter effects will be accompanied by fluctuations about the mean values, ie, scintillations. For instance, at 10 GHz in the UHF/SHF transmission experiment on the dust cloud from the DICE THROW HE explosion, fluctuations of ±8 dB about the mean attenuation of 20 dB were observed at early times. There were corresponding fluctuations in the phase. The DICE THROW cloud was highly turbulent during these observed fluctuations.

There has been a large theoretical effort devoted to the transport of radiation through regions of randomly varying dielectric constant. This corresponds to transport through turbulent air. In the field of nuclear effects, transport through striated plasma regions has been studied and modeled. However, transport through a turbulent dust region is significantly more complicated. Very little theoretical work exists on the distribution of dust in a turbulent region. Dust particles both absorb and scatter the incident radiation; the scattering is typically wide-angle scattering.

The level of effort required to develop dust scintillation models is not known, but may be considerable. A theoretical investigation would require the mass loading and sizes of the dust inhomogenities, and their number, location, and velocity probability distributions. All these parameters must be known as a function of time. Then the transport

through a random wide angle scattering region has to be calculated. Rather than carrying out a full theoretical study, it may be possible to develop crude first-order models based on experimental data and simplified transport physics.

In this report we choose the following four areas for detailed development:

- Mie scattering theory
- Size distributions of dust particles
- Complex index of refraction of dust particles
- Dust models for the stem and pedestal regions.

The backscatter and scintillation areas are not discussed further in this report.

SECTION 2
MIE SCATTERING THEORY

The Mie theory gives the exact solutions for the scattering and absorption of an electromagnetic wave incident on a uniform spherical particle. The solutions are given as infinite series of complex terms. Many techniques have been developed to numerically evaluate the Mie equations. The simplest technique is to use a forward recursion scheme to evaluate the successive terms. This is the technique used in the present WEPH code. However, in some cases the forward recursion technique is not stable. To avoid the instability of the forward recursion technique, many backward recursion schemes have been developed. For the WOE code, Reference 1, a new backward recursion Mie code was developed. This Mie code is stable, accurate at all orders, and can be used for any frequency and particle size. The following description of the new Mie calculation is largely taken from the WOE code documentation, Reference 1. Appendix A is a listing of the new Mie computer routines.

We first present the formulas for the Mie solution (see any standard text for a derivation) and then the method used to solve the equations. Define the following quantities:

a = diameter of the spherical particle (cm)

λ = wavelength of the incident radiation (m)

$\alpha = 10^{-2} \frac{\pi a}{\lambda}$

= dimensionless size parameter (the factor 10^{-2} converts a from cm to m)

$m = m_R - i m_I$

= complex index of refraction of the sphere (note that here

11

we are using m instead of n, since by custom n is used as the order in the Mie formulas)

$Y = m\alpha$

σ_{SCA} = scattering cross section of the sphere (m^2)

σ_{ABS} = absorption cross section of the sphere (m^2)

σ_{BKS} = backscatter cross section of the sphere (m^2)

$$Q_{SCA} = 10^4 \frac{\sigma_{SCA}}{\pi(a/2)^2}$$

= scattering efficiency (ratio of scattering cross section to physical cross section) of the sphere. The factor 10^4 converts the sphere area in cm^2 to m^2.

$$Q_{ABS} = 10^4 \frac{\sigma_{ABS}}{\pi(a/2)^2}$$

= absorption efficiency of the sphere

$Q_{EXT} = Q_{ABS} + Q_{SCA}$ = extinction efficiency

$$Q_{BKS} = 10^4 \frac{\sigma_{BKS}}{\pi(a/2)^2}$$

= backscatter efficiency

$S(\theta)$ = scattering function $(m^2 \ sr^{-1})$. $S(\theta) \ d\Omega$ is the fraction of the incident unpolarized energy per unit area that is scattered into solid angle $d\Omega$ centered about the direction that makes an angle θ with the direction of the incident radiation (θ is the scattering angle). Note that $\sigma_{BKS} = 4\pi S(\pi)$.

Currently the WEPH code only uses the extinction parameters (to calculate total attenuation). We include the scattering and absorption parameters and the scattering function in our present discussion of the Mie solutions for completeness, and to allow for use in other DNA engineering codes.

The equations for the Mie solution are:

$$Q_{SCA} = \frac{2}{\alpha^2} \sum_{n=1}^{\infty} (2n + 1) \left[|a_n|^2 + |b_n|^2 \right] \qquad (1)$$

$$Q_{EXT} = \frac{2}{\alpha^2} \sum_{n=1}^{\infty} (2n + 1) \, \text{Re} \, (a_n + b_n) \qquad (2)$$

(where Re signifies the real part of)

$$Q_{ABS} = Q_{EXT} - Q_{SCA} \qquad (3)$$

$$Q_{BKS} = \frac{4}{\alpha^2} \left| \sum_{m=1}^{\infty} (n + \tfrac{1}{2})(-1)^n (a_n - b_n) \right|^2 \qquad (4)$$

$$S(\theta) = \frac{1}{2} \left(\frac{\lambda}{2\pi} \right)^2 \left\{ |S_1(\theta)|^2 + |S_2(\theta)|^2 \right\} \, , \qquad (5)$$

where

$$a_n = \frac{\alpha \Psi_n'(Y)\Psi_n(\alpha) - Y\Psi_n(\alpha)\Psi_n(Y)}{\alpha \Psi_n'(Y)\xi_n(\alpha) - Y\xi_n(\alpha)\Psi_n(Y)} \qquad (6)$$

$$b_n = \frac{Y\Psi_n'(Y)\Psi_n(\alpha) - \alpha \Psi_n'(\alpha)\Psi_n(Y)}{Y\Psi_n'(Y)\xi_n(\alpha) - \alpha \xi_n(\alpha)\Psi_n(Y)} \qquad (7)$$

$$S_1(\theta) = \sum_{n=1}^{\infty} \frac{2n + 1}{n(n + 1)} \left\{ a_n \pi_n(\cos \theta) + b_n \tau_n(\cos \theta) \right\} \qquad (8)$$

$$S_2(\theta) = \sum_{n=1}^{\infty} \frac{2n + 1}{n(n + 1)} \left\{ b_n \pi_n(\cos \theta) + a_n \tau_n(\cos \theta) \right\} \qquad (9)$$

and

$$\Psi_n(z) = \left(\frac{\pi z}{2} \right)^{1/2} J_{n+1/2}(z) \qquad (10)$$

$$\xi_n(z) = \left(\frac{\pi z}{2} \right)^{1/2} \left[J_{n+1/2}(z) + i(-1)^n J_{-n-1/2}(z) \right] \qquad (11)$$

13

$$\pi_n(\cos \theta) = P_n'(\cos \theta) \tag{12}$$

$$\tau_n(\cos \theta) = \cos \theta \, \pi_n(\cos \theta) - \sin^2\theta \, \frac{d}{d \cos \theta} \pi_n(\cos \theta) \quad . \tag{13}$$

The J's are spherical Bessel functions of complex argument and half-integer order. The P's are Legendre polynomials. Ψ and ξ are Riccati-Bessel functions, and π and τ are associated Legendre polynomials. Define an arbitrarily oriented plane containing the scattering sphere and the incident radiation. Then for scattered radiation within the plane, the complex amplitude function $S_1(\theta)$ describes the scattering for an incident plane wave with vertical polarization (E perpendicular to the scattering plane; $S_2(\theta)$ is for horizontal polarization (E parallel to the scattering plane).

As might be expected from the complexity of the Mie equations, the numerical evaluation of Q_{SCA}, Q_{EXT}, and $S(\theta)$ for a given m and α is not, in general, a trivial task. The terms in the infinite series have to be evaluated and summed. The number of terms that have to be evaluated before the series converge depends primarily upon the size parameter α. Roughly, the number of Mie terms required is 1.5α; for large particles and small wavelengths, several hundred terms are often required before convergence.

The evaluation of the various orders of ξ_n, π_n, and τ_n are straight-forward. We can use the well known recurrence relations of Bessel functions and Legendre polynomials to obtain

$$\xi_n(\alpha) = \frac{2n - 1}{\alpha} \xi_{n-1}(\alpha) - \xi_{n-2}(\alpha) \quad , \tag{14}$$

with initial values

$$\xi_0(\alpha) = \sin \alpha + i \cos \alpha \tag{15}$$

$$\xi_{-1}(\alpha) = \cos \alpha - i \sin \alpha \tag{16}$$

$$\pi_n(\cos \theta) = \frac{2n - 1}{n - 1} \cos \theta \, \pi_{n-1}(\cos \theta) - \frac{n}{n - 1} \pi_{n-2}(\cos \theta) \tag{17}$$

14

$$\tau_n(\cos\theta) = \cos\theta\left[\pi_n(\cos\theta) - \pi_{n-2}(\cos\theta)\right]$$

$$- (2n-1)\sin^2\theta\,\pi_{n-1}(\cos\theta) + \tau_{n-2}(\cos\theta) \quad . \quad (18)$$

The initial values are

$$\pi_0(\cos\theta) = 0$$

$$\tau_0(\cos\theta) = 0$$

$$\pi_1(\cos\theta) = 1$$

$$\tau_1(\cos\theta) = \cos\theta$$

$$\pi_2(\cos\theta) = 3\cos\theta$$

$$\tau_2(\cos\theta) = 3\cos(2\theta) \quad .$$

With the initial values, we can use the forward recurrence relations to generate the required terms to any order. The forward recursion technique for these three functions is stable and accurate.

To complete our numerical evaluation, we define the complex function

$$A_n(Y) = \frac{\Psi'(Y)}{\Psi(Y)} \quad . \quad (19)$$

with this definition, the Mie formulas for a_n and b_n can be written:

$$a_n = \frac{\left(\dfrac{A_n(Y)}{m} + \dfrac{n}{\alpha}\right)\mathrm{Re}\left\{\xi_n(\alpha)\right\} - \mathrm{Re}\left\{\xi_{n-1}(\alpha)\right\}}{\left(\dfrac{A_n(Y)}{m} + \dfrac{n}{\alpha}\right)\xi_n(\alpha) - \xi_{n-1}(\alpha)} \quad (20)$$

$$b_n = \frac{\left(mA_n(Y) + \dfrac{n}{\alpha}\right)\mathrm{Re}\left\{\xi_n(\alpha)\right\} - \mathrm{Re}\left\{\xi_{n-1}(\alpha)\right\}}{\left(mA_n(Y) + \dfrac{n}{\alpha}\right)\xi_n(\alpha) - \xi_{n-1}(\alpha)} \quad . \quad (21)$$

The primary difficulty in the evaluation of the Mie formulas lies in the evaluation of $A_n(Y)$. Using the properties of the Bessel functions,

15

we can write $A_n(Y)$ as

$$A_n(Y) = -\frac{n}{Y} + \frac{J_{n-1/2}(Y)}{J_{n+1/2}(Y)} \quad . \tag{22}$$

Thus, if we can evaluate the Bessel functions, say by forward recursion, $A_n(Y)$, can be evaluated. Alternately, we can use the recurrence relations for the ratios of the Bessel functions and write the recursion equation for $A_n(Y)$ itself as

$$A_n(Y) = -\frac{n}{Y} + \left(\frac{n}{Y} - A_{n-1}(Y)\right)^{-1} \tag{23}$$

with initial condition

$$A_o(Y) = \frac{\cos Y}{\sin Y} \quad . \tag{24}$$

The forward recursion technique for the evaluation of $A_n(Y)$ is very susceptible to error in at least four cases (Reference 2):

- When the argument is small
- When the argument is large, requiring a large number of orders
- When the imaginary value is larger than the real value
- For certain anomalous values.

The use of forward recursions to generate the consecutive orders of Bessel functions is a classic example of unstable numerical methods.

The current WEPH Mie calculation uses an asymptotic analytic formula whenever the argument is small and thus avoids the first error case; the others still remain, however.

Many other techniques have been devised to generate the required Bessel functions or ratios. Most techniques involve some type of backward recursion. The values of the Bessel functions or the ratios are evaluated at a high order, and the backward recursion relation is used to evaluate the lower orders. The backward recursion does not suffer

16

from the instability of the forward method. However, care must be taken
to preserve accuracy; some techniques lose accuracy even when using
double precision arithmetic. Recently Lentz (Reference 2) has developed
an algorithm for evaluating the Bessel functions and ratios that elim-
inates the weaknesses of the earlier methods. Lentz's algorithm uses a
new technique of evaluating continued fractions that starts at the be-
ginning rather than the tail and has a built-in error check. Using the
method, any $A_n(Y)$ can be generated completely independently of all pre-
ceding values with high accuracy. Readers are referred to Lentz's
article for details.

We use Lentz's method to generate $A_n(Y)$ for n of order $\approx 1.5x$ and
then use the backward recursion relationship,

$$A_{n-1}(Y) = \frac{n}{Y} - \left(\frac{n}{Y} + A_n(Y)\right)^{-1} \quad , \tag{25}$$

to generate all lower orders. Using the forward recursion relations for
the other functions, the a_n and b_n are calculated and the infinite series
summed until convergence. In almost all cases, convergence is reached
before reaching the highest precomputed order of $A_n(Y)$. Otherwise
Lentz's method is used to generate any additional needed terms.

Utilizing the Lentz algorithm, we have written a very compact com-
puter routine that evaluates the exact Mie equations for Q_{SCA}, Q_{BKS},
Q_{EXT} (and thus Q_{ABS}), and $S(\theta)$. The running time is quite reasonable
for an exact calculation. For $\alpha = 1.2$, three orders are required for
convergence, and the running time is 1 millisecond on a CDC 7600 com-
puter. For $\alpha = 100$, 103 orders are required with a running time of 25
milliseconds. For inclusion in the WEPH code, a simpler routine has
been assembled which calculates only Q_{EXT} and Q_{BKS}; this routine runs
considerably faster than the full calculation case. Listings of both
the full Mie calculation routine and the reduced routine are given
in Appendix A.

SECTION 3
SIZE DISTRIBUTIONS OF DUST PARTICLES

The two most common probability distributions used to describe par-
ticulate (whether dust, smoke, haze, fog, rain, or debris) size statistics
are the power law and the log-normal distributions. The power law prob-
ability distribution is

$$P_p(a) = \frac{(p-1)\ a^{-p}}{a_{min}^{-(p-1)} - a_{max}^{-(p-1)}} \qquad a_{min} \leq a \leq a_{max} \qquad (26)$$

where

a = particle diameter (cm)

$P_p(a)\ da$ = fraction of the particles with diameters between
n and a + da

p = power law exponent

a_{min} = minimum particle diameter in the distribution (cm)

a_{max} = maximum particle diameter in the distribution (cm).

The log-normal distribution is

$$P_L(a) = \frac{e^{-\frac{1}{2}\left[\frac{\ln\ a/a_m}{\ln\ S}\right]^2}}{\sqrt{2\pi}\ a\ \ln\ S} \qquad 0 \leq a \leq \infty \qquad (27)$$

where

a_m = mean particle diameter (cm)

S = standard deviation parameter.

The two distributions given are probability distributions, ie,

$$\int_{a_{min}}^{a_{max}} P_p(a) \, da = \int_0^\infty P_L(a) \, da = 1 \quad .$$

Let

N_{TP} = total number of particles in the power law distribution

N_{TL} = total number of particles in the log-normal distribution,

then

$$f_p(a) = N_{TP} P_p(a) \tag{28}$$

$$f_L(a) = N_{TL} P_p(a) \tag{29}$$

are the number distributions for the two cases, where

$f_p(a) \, da$ = number of particles in the power law distribution which have diameters between a and a + da.

Let

M_T = total mass of particulates (g)

ρ_b = bulk density of the particulate material (g cm^{-3}),

then

$$N_{TP} = \frac{M_T}{\frac{\pi}{6} \rho_b (a^3)_p} \tag{30}$$

$$N_{TL} = \frac{M_T}{\frac{\pi}{6} \rho_b (a^3)_L} \quad , \tag{31}$$

where

$$\overline{(a^3)_p} = \int_{a_{min}}^{a_{max}} a^3 P_p(a) \, da$$

$$= \frac{p-1}{a_{min}^{-(p-1)} - a_{max}^{-(p-1)}} \begin{cases} \ell n \, \dfrac{a_{max}}{a_{min}} & p = 4 \\[2em] \dfrac{1}{4-p}\left[a_{max}^{4-p} - a_{min}^{4-p} \right] & p \neq 4 \end{cases} \tag{32}$$

$$\overline{(a^3)}_L = \int_0^\infty a^3 P_L(a) \, da = a_m^3 \, e^{\frac{9}{2} [\ln S]^2} \quad . \tag{33}$$

Condensates, such as water droplets or the particles reformed from the weapon vaporized material, are generally well described by the log-normal size distribution. Some typical values used in previous particulate models are $a_m = 1.4 \times 10^{-5}$ cm (0.14 μm), $S = 1.9$ for recondensed weapon material particulates and $a_m = 5 \times 10^{-4}$ cm (5 μm), $S = 2.0$ for water droplets within a nuclear cloud.

Dust and crater ejecta particulates are generally better described by a power law distribution, at least for particles greater than a few hundredths of a centimeter in diameter. Experimental data from a number of HE (high explosive) and nuclear tests, References 3 and 4, indicate that typical values for the power law exponent are $p \sim 3.5$ for rock and cohesive soils (such as clay or shale) and $p \sim 4$ for loose unconsolidated soils (such as desert alluvium or sand). Fine soils may have $p \sim 5$.

The log-normal distribution is well behaved mathematically at both limits of small and large particle diameters. The power law distribution is not well behaved at either limit. As a_{min} goes to zero both the probability distribution $P_p(a_{min})$ and the total number of particles N_{TP} go to infinity. As a_{max} goes to infinity, the probability distribution $P(a_{max})$ goes to a well behaved zero, but N_{TP} goes to zero for a finite M_T. There are several techniques employed to eliminate mathematical difficulties at the endpoints. The most common technique, and the one we implicitly assumed when we defined the power law, is simply to cut the distribution off at some lower and upper limits, a_{min} and a_{max}. Another technique is to assume an upper limit, a_{max}, but to attach a mathematically well behaved tail at the lower end of the distribution. This lower limit tail can be some artificial mathematical expression chosen for computational convenience, or, as is often the case, can be a fit to the actual experimental data in the small particle limit.

SAI, Reference 4, reviewed the experimental data on dust particle size distributions from nuclear test events. They then analyzed in detail the more recent (and more complete) dust size data from HE tests. Their conclusion was that the small size particles have a log-normal size distribution, while the larger particles have a power law size distribution. The size division between small and large particles occurs at a particle diameter of about 0.018 cm (180 μm). We will develop the equations for the hybrid size distribution of a log-normal small-limit tail attached to a power law distribution.

The hybrid probability distribution is given by

$$P_H(a) = \begin{cases} C_1 P_L(a) & 0 \leq a \leq a_{min} \\ \\ C_2 P_p(a) & a_{min} \leq a \leq a_{max} \end{cases} \tag{34}$$

where C_1 and C_2 are normalization constants which ensure that

$$\int_0^{a_{max}} P_H(a) \, da = 1 \tag{35}$$

$$C_1 P_L(a_{min}) = C_2 P_p(a_{min}) \quad , \tag{36}$$

ie, the constants ensure that the total probability distribution is properly normalized to unity and that the log-normal and the power law distributions join at a_{min}. C_1 and C_2 are given by

$$C_1 = \frac{P_p(a_{min})}{P_L(a_{min})} C_2 \tag{37}$$

$$C_2 = \left[1 + F_U\left(\frac{\ln \frac{a_{min}}{am}}{\ln S} \right) \frac{P_p(a_{min})}{P_L(a_{min})} \right]^{-1} \quad , \tag{38}$$

where

$$F_U(x) = \frac{1}{\sqrt{2\pi}} \int_{-\infty}^{x} e^{-\frac{1}{2}t^2} dt \qquad (39)$$

= cumulative probability of the standardized normal
random probability distribution.

For the hybrid distribution,

$$\overline{(a^3)}_H = \int_0^{a_{max}} a^3 P_H(a) \, da = C_1 \int_0^{a_{min}} a^3 P_L(a) \, da + C_2 \int_{a_{min}}^{a_{max}} a^2 P_p(a) \, da$$

$$= C_1 \overline{(a^3)}_L F_U \left(\frac{\ell n \frac{a_{min}}{am}}{\ell n \, S} - 3 \ell n \, S \right) + C_2 \overline{(a^3)}_p \qquad (40)$$

and the total number of particles for a given mass M_T is

$$N_{TH} = \frac{M_T}{\frac{\pi}{6} \rho_b \overline{(a^3)}_H} \qquad . \qquad (41)$$

For the hybrid distribution, the fraction of the total number of particles
in the power law segment and the log-normal segment is

$$f_{NP} = \frac{(N_{TH})_P}{N_{TH}} = C_2 \qquad (42)$$

$$f_{NL} = \frac{(N_{TH})_L}{N_{TH}} = 1 - C_2 \qquad . \qquad (43)$$

The fractions of the total dust mass which lie in the two segments are

$$f_{MP} = \frac{(M_T)_P}{M_T} = C_2 \frac{\overline{(a^3)}_P}{\overline{(a^3)}_H} \qquad (44)$$

$$f_{ML} = \frac{(M_T)_L}{M_T} = 1 - f_{MP} \qquad . \qquad (45)$$

For cohesive soils Reference 4 recommends the following values for the hybrid distribution parameters:

a_m = 0.002 cm (20 μm)

S = 2

a_{min} = 0.018 cm (180 μm)

a_{max} = 1 cm

p = 3.5 .

The current WEPH model assumes that for nuclear bursts the size distribution is a power law distribution best represented as that of unconsolidated soils and takes

$$P_p(a) = \frac{3}{a_{min}^{-3} - a_{max}^{-3}} \, a^{-4} \quad , \text{ie, } p = 4$$

a_{min} = 0.001 cm (10 μm)

a_{max} = 10 cm .

The 10-cm a_{max} value is for surface and very near surface (ie, cratering) bursts. As the burst height is increased, cratering ceases, the lofting power of the nuclear induced winds decreases, and a_{max} is also assumed to decrease.

We can improve the size distribution model by adopting either a general power law distribution (arbitrary p, not just p = 4), or the general hybrid distribution. As we shall show later, the attenuation and backscatter effects of the hybrid distribution are not significantly different from the corresponding power law distribution except for extremely high frequencies (greater than about 100 GHz). For the present, we adopt the generalized power law distribution. If in the future the higher frequencies become important, the hybrid distribution can be easily implemented into the WEPH code. The changes required in the code to generalize the fixed p = 4 size model to a general p

23

are trivial.   Appendix B gives a list of the generalized model equations
and a listing of the generalized PGROUP subroutine, which calculates the
extinction and backscatter cross sections.   To illustrate the variation
of effects with changing size distribution parameter, Figure 1 shows the
extinction cross section per gram of material as a function of p for dry
sandy soil for a number of frequencies.

For a given amount of dust mass, what is the difference in extinction
and backscatter properties for the hybrid and the corresponding power law
size distributions?   To illustrate the differences numerically, we adopt
the following parameter values:

Power law size distribution	Hybrid size distribution
a_{min} = 0.001 cm (10 μm)	a_{min} = 0.018 cm (180 μm)
a_{max} = 10 cm	a_{max} = 10 cm
p = 3.5 and 4.0 (ie,	a_m = 0.002 (20 μm)
hard rock and soil	S = 2
particles)	p = 3.5 and 4.0

For both distributions, we take

$$M_T = 10^6 \text{ g}$$

$$\rho_b = 2.5 \text{ g cm}^{-3} \quad .$$

The probability distributions are

$$P_p(a) = \begin{cases} 7.906 \times 10^{-8} \, a^{-3.5} & p = 3.5 \\ 3.000 \times 10^{-9} \, a^{-4} & p = 4.0 \end{cases} \quad 0.001 \leq a \leq 10 \quad .$$

$$(46)$$

The hybrid distribution is
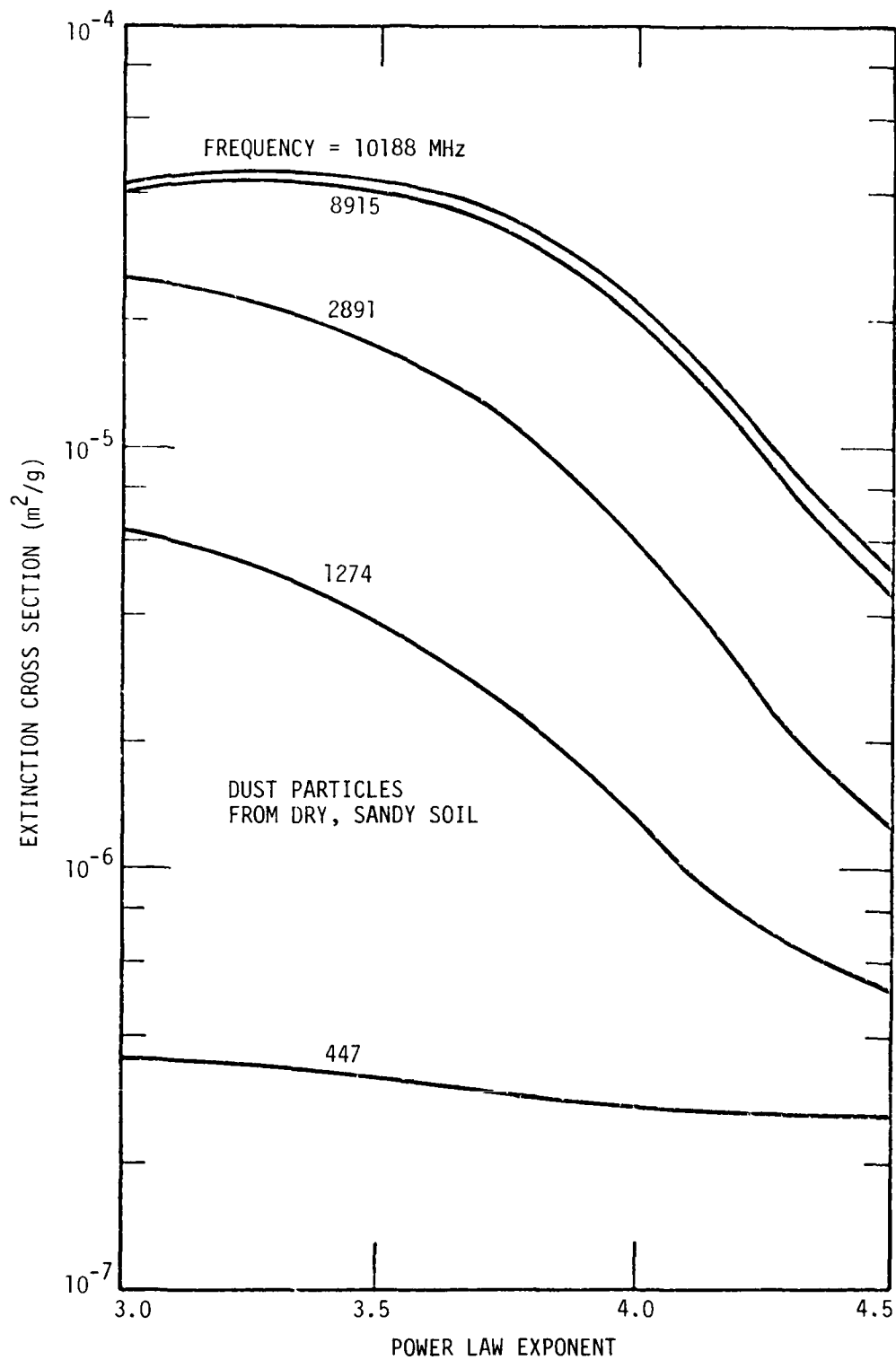
Figure 1. Extinction cross section for dust particles with a power law size distribution.

25

$$P_H(a) = \begin{cases} \begin{cases} \dfrac{0.5750}{a}\, e^{-\frac{1}{2}\left[\dfrac{\ell n\,\dfrac{a}{0.002}}{\ell n\,2}\right]^2} & 0 \leq a \leq 0.018 \\[2em] 1.643 \times 10^{-7} a^{-3.5} & 0.018 \leq a \leq 10 \end{cases} & p = 3.5 \\[4em] \begin{cases} \dfrac{0.5751}{a}\, e^{-\frac{1}{2}\left[\dfrac{\ell n\,\dfrac{a}{0.002}}{\ell n\,2}\right]^2} & 0 \leq a \leq 0.018 \\[2em] 2.204 \times 10^{-8} a^{-4} & 0.018 \leq a \leq 10 \end{cases} & p = 4.0 \end{cases} \qquad (47)$$

Figure 2 shows the power law and hybrid distributions. In addition the entire log-normal probability distribution is shown. We see that the log-normal and hybrid distributions have many particles below the small-limit cutoff of the power law distribution. Both the power law and hybrid distributions have more large particles than the log-normal distribution.

The normalization constants for the hybrid distribution are

$$C_1 = \begin{cases} 0.9991 & p = 3.5 \\ 0.9992 & p = 4.0 \end{cases} \qquad (48)$$

$$C_2 = \begin{cases} 1.512 \times 10^{-3} & p = 3.5 \\ 1.260 \times 10^{-3} & p = 4.0 \end{cases} \qquad (49)$$

The $\overline{(a^3)}$ values for the two distributions are

$$\overline{(a^3)}_p = \begin{cases} 4.950 \times 10^{-7} & cm^3 & p = 3.5 \\ 3.482 \times 10^{-8} & cm^3 & p = 4.0 \end{cases} \qquad (50)$$
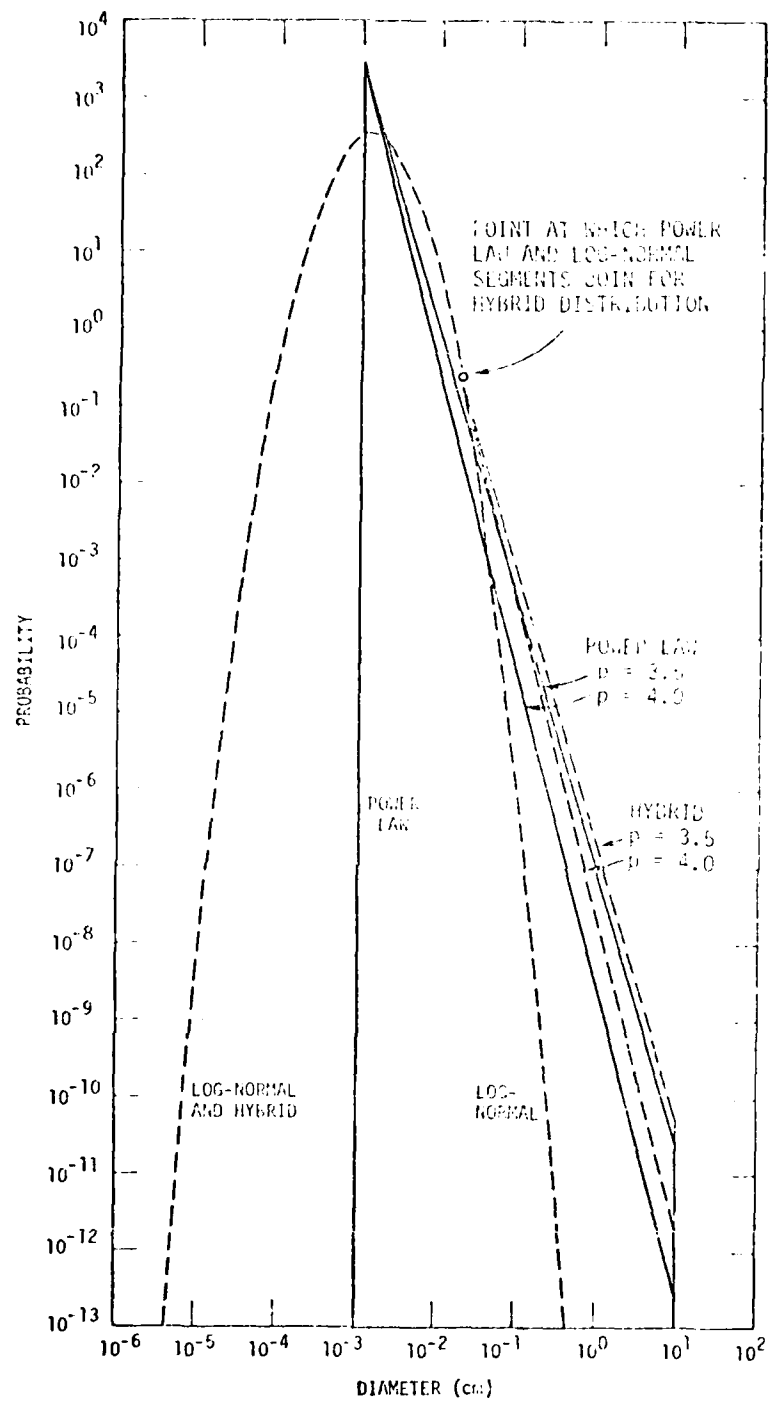
Figure 2. Dust particle size probability distributions.

$$\overline{(a^3)}_H = \begin{cases} 1.055 \times 10^{-6} \text{ cm}^3 & p = 3.5 \\ 1.992 \times 10^{-7} \text{ cm}^3 & p = 4.0 \end{cases} \tag{51}$$

The total number of particles in 10^6 grams of mass is

$$(N_T)_p = \begin{cases} 1.543 \times 10^{12} & p = 3.5 \\ 2.665 \times 10^{13} & p = 4.0 \end{cases} \tag{52}$$

$$(N_T)_H = \begin{cases} 7.241 \times 10^{11} & p = 3.5 \\ 3.835 \times 10^{12} & p = 4.0 \end{cases} \tag{53}$$

The number distributions for the two cases are

$$f_p(a) = (N_T)_p P_p(a) = \begin{cases} 1.220 \times 10^5 a^{-3.5} & p = 3.5 \\ & 0.001 \le a \le 10 \\ 8.295 \times 10^4 a^{-4} & p = 4.0 \end{cases} \tag{54}$$

$$f_H(a) = (N_T)_H P_H(a) = \begin{cases} \begin{cases} \dfrac{4.164 \times 10^{11}}{a} e^{-\frac{1}{2}\left[\frac{\ell n \frac{a}{0.002}}{\ell n 2}\right]^2} & 0 \le a \le 0.018 \\ & \qquad p = 3.5 \\ 1.190 \times 10^5 a^{-3.5} & 0.018 \le a \le 10 \end{cases} \\ \begin{cases} \dfrac{2.206 \times 10^{12}}{a} e^{-\frac{1}{2}\left[\frac{\ell n \frac{a}{0.002}}{\ell n 2}\right]^2} & 0 \le a \le 0.018 \\ & \qquad p = 4 \\ 8.452 \times 10^4 a^{-4} & 0.018 \le a \le 10 \end{cases} \end{cases} \tag{55}$$

We see that although the probability distributions and the total number of particles are different for the power law and the hybrid distributions, the number of particles versus size is virtually identical for particles

28

greater than 0.018 cm (the joining point between the log-normal segment and the power law segment in the hybrid distribution).

$$\frac{f_p(a)}{f_H(a)} = \begin{cases} 0.9752 & p = 3.5 \\ \\ 1.019 & p = 4.0 \end{cases} \qquad a \geq 0.018 \quad . \qquad (56)$$

So any differences in the extinction and backscatter properties are due almost entirely to the smaller particles (those with diameters less than 0.018 cm (180 μm)). The fraction of the total number of particles with diameters less than 0.018 cm and the fraction of the total mass carried by these smaller particles are

$$(f_N)_p = \begin{cases} 0.9993 & p = 3.5 \\ 0.9998 & p = 4.0 \end{cases} \qquad a \leq 0.018 \qquad (57)$$

$$(f_N)_H = \begin{cases} 0.9991 & p = 3.5 \\ 0.9992 & p = 4.0 \end{cases} \qquad a \leq 0.018 \qquad (58)$$

$$(f_M)_p = \begin{cases} 3.278 \times 10^{-2} & p = 3.5 \\ 0.3139 & p = 4.0 \end{cases} \qquad a \leq 0.018 \qquad (59)$$

$$(f_M)_H = \begin{cases} 5.680 \times 10^{-2} & p = 3.5 \\ 0.3004 & p = 4.0 \end{cases} \qquad a \leq 0.018 \quad . \qquad (60)$$

Hence, more than 99.9 percent of the particles are small particles, but they constitute only about 3 to 6 percent of the total mass for a hard rock size distribution (p = 3.5) and about 30 percent for a soil distribution (p = 4.0).

The scattering and absorption cross sections for a particle of diameter a are given by

29

$$\sigma_{SCA} = 10^4 \pi \left(\frac{a}{2}\right)^2 Q_{SCA} \qquad m^2 \tag{61}$$

$$\sigma_{ABS} = 10^4 \pi \left(\frac{a}{2}\right)^2 Q_{ABS} \qquad m^2 \tag{62}$$

where Q_{SCA} and Q_{ABS} are the scattering and absorption efficiencies, respectively. In the long wavelength limit, ie, where

$$\alpha = \frac{10^{-2} \pi a}{\lambda} \ll 1$$

and

λ = wavelength of the incident radiation (m)

then

$$Q_{SCA} \propto a^4$$
$$Q_{ABS} \propto a$$

so that

$$\sigma_{SCA} \propto a^6$$
$$\sigma_{ABS} \propto a^3 \quad .$$

In the short wavelength limit, ie, where

$$\alpha \gg 1 \quad ,$$

then both Q_{SCA} and Q_{ABS} approach constant values and

$$\sigma_{SCA} \propto a^2$$
$$\sigma_{ABS} \propto a^2 \quad .$$

So in the long wavelength limit, it is the largest particles that dominate the total scattering cross section for the whole size distribution. In this limit, the absorption cross section is seen to be proportional to the amount of mass carried by the particles. Most often in the long

wavelength limit, absorption dominates scattering so that the extinction is also determined by the amount of mass. In the short wavelength limit, both absorption and scattering are dominated by particles with diameters about a particular size. This dominant size is generally near $\alpha = 1$.

Hence if the long wavelength limit obtains for the small particles, the extinction and backscatter properties of the power law and the hybrid distributions are virtually identical. The scatter is determined by the larger particles, and both numerical distributions are essentially the same. The absorption contribution of the smaller particles is determined by their total mass, which as we have seen is negligible for hard rock (p = 3.5) and almost identical (31 and 30 percent) for the two distributions for soil (p = 4.0). If the long wavelength limit fails for any of the small particles, then the two distributions will have significantly different extinction and backscatter properties.

The frequency corresponding to $\alpha = 1$ for a particle of diameter 0.018 cm is

$$F = 530 \text{ GHz}.$$

Hence, for frequencies below about 100 GHz, the small particles can be considered to be in the long wavelength limit, and the power law and hybrid distributions produce essentially identical propagation effects. The simpler power law formulation can be used without loss of accuracy. If the frequency of interest rises much above 100 GHz, then the hybrid distribution formulation should be implemented.

SECTION 4
COMPLEX INDEX OF REFRACTION
OF DUST PARTICLES

The complex index of refraction determines the scattering and absorp-
tion properties of a dust particle. In the current WEPH model, there are
three typical soil types built in the program with the indices given in
Table 1. These are representative values for soils at a frequency of 3
GHz (S-band). These values are taken as constants, independent of fre-
quency. At frequencies much lower than S-band, the dust effects are gen-
erally negligible. It was also assumed that the primary interest was for
frequencies below about 10 GHz. Therefore a constant index of refraction
was a reasonable assumption. But with the addition of a stem dust model,
the dust loading may be high enough to significantly affect frequencies
lower than S-band. In addition, radar and communication systems with
frequencies higher than 10 GHz are becoming more common. The frequency
range of interest has broadened sufficiently that the assumption that the
index of refraction is independent of frequency is no longer valid.

Table 1. WEPH soil types.

Soil Type	Index of Refraction
Wet clay	$3.5 - 0.4i$
Dry sand	$1.5 - 0.025i$
Ice-covered soil	$1.78 - 0.0024i$

Also, allowing only three choices of soil types is unduly restrictive.
There is essentially an infinite variety of soils, with a continuous vari-
ation of the index of refraction. The absorption due to dust particles
is proportional to the imaginary part of the complex index of refraction.

32

The three soil choices have imaginary indices roughly an order of magnitude apart. The attenuation for a system could be 1, 10. or '00 dB, depending on the choice made for the soil type. A finer d￟ ion of soil types (and thus attenuations) is called for.

Another major assumption, implicitly expressed, is that the soil index of refraction can also be used for the index of refraction for the individual dust particles. Most soil indices of refraction are derived from measurements made on soil samples which have been removed from the field and carried back to the laboratory. Soil can be considered to consist of three components—solid material, water, and air. The soil indices are determined by the relative fractions of the three components, and by the electrical properties of the solid and water components. *In situ* soil, laboratory soil samples, and individual particles will all have different fractions of the three constitutive components and will thus have different indices of refraction. There are various mixing rules available which relate the index of soil in one state to the index of the same soil in another state. We will make use of the semidisperse model of Reference 5. In addition to relating the indices of different phases of the same soil, the semidisperse model allows the index of refraction to be calculated for a given soil or particle if the dielectric properties and volume fractions of the constituents are known.

For the WEPH code, a more complete method for specifying the index of refraction for dust particles is required. There are a number of possible approaches. The simplest and most general (and the easiest to implement into the code) is to allow the user to specify as input the index of refraction for each input frequency. This input option is the most accurate provided, naturally, that the user knows the index of refraction of the dust particles (not the soil index) for his case of interest. In many cases the user may know various physical or electrical characteristics of the soils but not the indices of the individual particles. Later in this section, we present analytic methods of calculating the dust particle index of refraction knowing

either the characteristics of the dust particle or of the bulk soil.

Another option is to expand the built-in choices of soils. The present choices of three soils with widely spaced imaginary indices can be expanded to, say, ten soils with more closely spaced imaginary indices. The user would choose one of the ten typical soil types, and the built-in index of refraction list would consist of the indices of the dust particles formed from the chosen soil. Moreover, the indices would be frequency dependent.

We now present the semidisperse model. We begin by defining the complex permittivity of a medium. The permittivity appears in the literature in various forms depending on how the permittivity was measured or the physics in which the permittivity appears. The most common form is the relative complex permittivity:

$$\varepsilon^* = \varepsilon' - i\,\varepsilon''$$

$$= K - i\,\frac{\sigma}{\varepsilon_o \omega}$$

$$= K(1 - i\,\tan\delta)\quad, \tag{63}$$

where

ε^* = relative complex permittivity

     = $\varepsilon/\varepsilon_o$

ε = complex permittivity ($F\,m^{-1}$)

ε',K = relative dielectric constant (often reported simply as the dielectric constant)

ε'' = dielectric loss factor

δ = dielectric loss angle (rad). Sometimes the dielectric phase angle θ is given, where $\theta = \pi/2 - \delta$

ω = angular frequency of incident radiation (rad s^{-1})

σ = material conductivity (mho m^{-1})

ε_o = permittivity of free space ($8.85 \times 10^{-12}\ F\,m^{-1}$)

i = $\sqrt{-1}$.

The complex index of refraction is related to the relative complex permittivity by

$$m = \sqrt{\varepsilon^*} \quad . \tag{64}$$

Writing m in terms of its real and imaginary parts as

$$m = m_R - i m_I \quad , \tag{65}$$

then

$$m_R = \sqrt{\frac{\varepsilon'}{2}\left(\sqrt{1 + \left(\frac{\varepsilon''}{\varepsilon'}\right)^2} - 1\right)}$$

$$= \sqrt{\frac{\kappa}{2}\left(\sqrt{1 + \tan^2\delta} - 1\right)}$$

$$= \sqrt{\frac{\kappa}{2}\left(\sqrt{1 + \frac{\sigma^2}{\varepsilon_o^2\kappa^2\omega^2}} - 1\right)} \tag{66}$$

$$m_I = \sqrt{\frac{\varepsilon'}{2}\left(\sqrt{1 + \left(\frac{\varepsilon''}{\varepsilon'}\right)^2} + 1\right)}$$

$$= \sqrt{\frac{\kappa}{2}\left(\sqrt{1 + \tan^2\delta} + 1\right)}$$

$$= \sqrt{\frac{\kappa}{2}\left(\sqrt{1 + \frac{\sigma^2}{\varepsilon_o^2\kappa^2\omega^2}} + 1\right)} \quad . \tag{67}$$

For a monochromatic plane electromagnetic wave propagating in the z direction in a uniform medium with complex index of refraction m, the electric field intensity can be written as

$$E(z,t) = E_o e^{i\omega(t - mz/c)}$$

$$= E_o e^{i\omega t} e^{-\omega m_I/c\, z} e^{-i\omega m_R/c\, z}$$

$$= E_o e^{i\omega t} e^{-\alpha z} e^{-i\beta z} \quad , \tag{68}$$

where

$$\gamma = \alpha + i\beta = i\frac{\omega}{c}m = \text{propagation factor } (m^{-1}) \tag{69}$$

$$\alpha = \frac{\omega m_I}{c} = \text{attenuation factor (nepers } m^{-1}) \tag{70}$$

$$\beta = \frac{\omega}{c}m_R = \text{phase factor (rad } m^{-1}) . \tag{71}$$

α is the attenuation coefficient for the amplitude. Our interest is normally in the power attenuation coefficient, which is

$$k = 2\alpha = \frac{2\omega}{c}m_I \qquad m^{-1}$$

$$= \frac{20\omega\, m_I}{c\,\ell n\,10} \qquad dB\ m^{-1} . \tag{72}$$

A dust cloud consists of discrete dust particles dispersed in air. In the general case, the particles both absorb and scatter the incident radiation. In general, then, the cloud cannot be considered a uniform medium; and the attenuation coefficient must be calculated using the Mie theory rather than the simple uniform medium expression of Equation 72. Under certain restrictive conditions, however, the cloud can be considered a uniform medium, and the simpler attenuation (and phase delay) equations can be used. If the long wavelength limit obtains (radiation wavelength much larger than the dust particle sizes) and absorption dominates scattering, then the attenuation is proportional to the dust cloud mass density and does not depend upon the details of the particle sizes. In this simple case, a dust cloud index of refraction can be defined and the uniform medium relations used. The exact Mie relations can also be used for this simple case, of course; the same attenuation coefficient results from either calculation. When scattering is significant, or the long wavelength limit does not obtain, only the Mie relations can be used for the attenuation. For backscatter calculations, the Mie relations must be used in all cases.

Consider a two-phase mixture, consisting of a disperse phase (discrete elements) contained in a continuous medium, as shown in Figure 5.

36
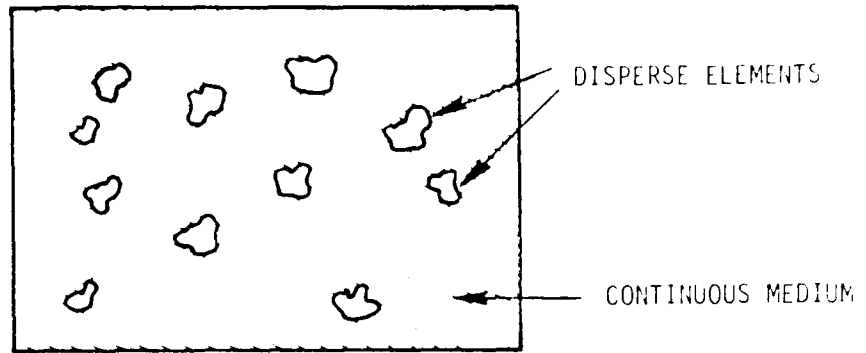
Figure 3.   A two-phase mixture.

Let

ϵ^* = relative complex permittivity of the two-phase mixture

ϵ_m^* = relative complex permittivity of the continuous medium

ϵ_d^* = relative complex permittivity of the disperse elements

ϕ = volume fraction of the disperse phase

$\quad = \dfrac{\text{volume of disperse elements}}{\text{total volume}}$.

Then the mixing rule for this two-phase system is given by Hanai, Reference 6, as

$$\frac{\epsilon^* - \epsilon_d^*}{\epsilon_m^* - \epsilon_d^*} \left(\frac{\epsilon_m}{\epsilon^*}\right)^{1/3} = 1 - \phi \quad . \tag{73}$$

Wobschall (Reference 5) shows that the permittivity of a multi-phase system can be calculated by the appropriate repeated applications of this two-phase mixing rule.   Let

$$C = \frac{(1 - \phi)^3 (\epsilon_m^* - \epsilon_d^*)^3}{\epsilon_m^*} \tag{74}$$

$$D = \frac{(\epsilon^* - \epsilon_d^*)^3}{(1 - \phi)^3 \epsilon_m^*} \quad . \tag{75}$$

37

Cubing both sides of Equation 75 and gathering terms, the two-phase
mixing rule can be written as a cubic equation:

$$\epsilon^{*3} - 3\epsilon_d^* \epsilon^{*2} + (3\epsilon_d^{*2} - C)\epsilon^* - \epsilon_d^{*3} = 0 \qquad (76)$$

or

$$\epsilon_m^{*3} - 3\epsilon_d^* \epsilon_m^{*2} + (3\epsilon_d^{*2} - D)\epsilon_m^* - \epsilon_d^{*3} = 0 \quad . \qquad (77)$$

The first form is appropriate if ϵ_d^* and ϵ_m^* are known and ϵ^* is the un-
known. The second form is for ϵ^* and ϵ_d^* known, with ϵ_m^* unknown. These
cubic equations can be solved by the standard techniques, and a computer
routine has been written to solve them (given in Appendix C).

Our first application of the mixing rule will be the calculation of
the permittivity of a particle knowing the constituent properties. The
particle will be considered to be a mixture of solid material, water, and
air. First consider a large particle such as a rock. For most rocks,
conduction is electrolytic, the conduction medium being an aqueous solu-
tion of common salts, distributed in a complicated manner through the
pore structure of a rock (Reference 7). As long as there is a continuous
film of water over all the surfaces of the rock structure, the rock con-
ductivity is a smooth function of the water volume and water conductivity.
The solid (essentially nonconducting) material of the rock can be con-
sidered to be dispersed in a conducting water medium. If the water con-
tent of the rock is below the critical saturation (the water film is no
longer continuous), then we would have discrete conducting water elements
dispersed in a nonconducting medium; the conductivity of the rock would
be greatly reduced. Besides solid and water, a rock has air in its pore
structure. The fraction of air in a rock is known as its porosity. We
will assume that a dust particle is constructed similarly to a rock.
Further, we assume the water film in the particle is unbroken. For the
particle, let

$$f_s = \text{volume fraction of solid material}$$

f_a = volume fraction of air (porosity)

f_w = volume fraction of water

ε_s^*, ε_a^*, ε_w^* = complex relative permittivities of solid, air, and water, respectively

Note that $f_s + f_a + f_w = 1$

We calculate the permittivity of the particle by two successive applications of the mixing rule, Equation 76. First we find the permittivity of the solid-water mixture by considering that the solid is dispersed in the continuous water. Thus

$$\varepsilon_d^* = \varepsilon_s^*$$

$$\varepsilon_m^* = \varepsilon_w^*$$

$$\phi = \frac{f_s}{f_s + f_w}$$

for the first application. Let ε_{sw}^* be the solution for the solid-water mixture. The particle permittivity is found by a second application considering that air is dispersed in the continuous solid-water mixture. We use Equation 76 again with

$$\varepsilon_d^* = \varepsilon_a^*$$

$$\varepsilon_m^* = \varepsilon_{sw}^*$$

$$\phi = f_a \ .$$

For frequencies below about 1 GHz the relative dielectric constant of water is essentially constant, and is given by

$$K_w = 87.8 - 0.37T, \tag{78}$$

where T is the temperature (°C). It happens that K_s varies little with soil type and is approximately equal to 3.5 (Reference 5). We will calculate the dielectric constant and conductivity of the particle assuming the following parameters:

39

$$K_w = 79.1$$

$$K_a = 1.0$$

$$\sigma_a = 0$$

$$K_s = 3.5$$

$$\sigma_s = 0 \quad .$$

Recall that

$$\varepsilon^* = K - i \frac{\sigma}{\varepsilon_o \omega} = K - i \frac{1.7976 \times 10^{10} \sigma}{f} \quad , \tag{79}$$

where f is the frequency (Hz). Applying the mixing rule twice as discussed above leads to the results shown in Table 2, where σ_p is the conductivity of the particle (mho m^{-1}).

Table 2. Dielectric constant and conductivity of a particle.

$\dfrac{f_w}{f_s + f_w}$ \ f_a	K_p						$\dfrac{\sigma_p}{\sigma_w}$					
	0	0.1	0.2	0.3	0.4	0.5	0	0.1	0.2	0.3	0.4	0.5
0.1	6.8	6.1	5.3	4.6	3.9	3.3	0.036	0.031	0.026	0.021	0.017	0.013
0.2	11.4	10.0	8.6	7.3	6.1	5.0	0.093	0.080	0.067	0.055	0.044	0.033
0.3	17.1	14.6	12.7	10.6	8.7	7.0	0.17	0.14	0.12	0.094	0.074	0.054
0.4	23.8	20.5	17.4	14.5	11.8	9.3	0.26	0.22	0.18	0.15	0.12	0.091
0.5	31.2	26.9	22.8	18.9	15.3	12.0	0.36	0.30	0.25	0.21	0.17	0.13

Analytic fits to these results are given by

$$K_p = 30.5 \; (1.475x^2 + 1.010x + 0.126)(0.4033f_a^2 - 1.388f_a + 1.00) \tag{80}$$

$$\sigma_p = 0.355\sigma_w(2x^2 + 1.045x - 0.023)(0.423f_a^2 - 1.5f_a + 1) \text{ mho m}^{-1} \quad . \tag{81}$$

The error in the conductivity fit is less than 1.5 percent. The maximum error in the dielectric constant fit is 9 percent; for all but two table entries, the error is less than 4 percent. The normal ranges for porosity

in rocks (f_a) is from 0 to about 60 percent, with a median value of about 15 percent. For connate water conductivity, 0.05 mho m^{-1} is a low conducitvity, 0.3 is a typical medium value, and 20 is a high value at radio broadcast frequencies.

The DICE THROW event was an HE (high explosive) test, conducted near the Giant Patriot site on the White Sands Missile Range, 6 October 1976 (Reference 8). The charge for this test was composed of approximately 628 tons (570 metric tons) of ammonium nitrate fuel oil (ANFO). A complement of 33 experimenters and support agencies participated in this nuclear simulation test event. SRI (References 8,9,10) fielded a UHF/ microwave transmission experiment to measure the effects of dust and debris on signals passing through the cloud generated by the blast. Both amplitude and phase shift were measured. The measurement frequencies are shown in Table 3. Several samples of loose crater material were collected after the detonation and analyzed to determine their dielectric properties and mass densities. Using the laboratory measurements we will compute the dielectric properties of the individual dust grains by means of the mixing rule. Using the dust grain values, we will then compute the propagation properties of the dust cloud by two methods: first, by the simpler mixing rule method, and second by the full Mie calculation. Finally, we will compare our calculated values of the dust cloud attenuation with the experimentally measured values.

We expect our calculated dust cloud attenuations to be equal or less than the measured attenuations. This is because the actual cloud has not only dust but the combustion products of the 628 tons of ANFO. If the extra attenuation due to these combustion products is unimportant at a given frequency, then the calculated and measured attenuations should be similar. If the combustion products attenuation is significant, then the dust attenuation will fall significantly below the measured attenuation. In the case of a nuclear device, the attenuation due to the device products will be negligible compared to the dust, since the nuclear products represent an infinitesimal fraction of the nuclear-lofted dust.

41

Table 3. Measurement frequencies.

Path	Frequency (MHz)
1	378.608, 413.028, 447.447
	1273.503
	2891.196
	10188.024
2	413.028
	10188.024
3	413.028
	10188.024
4	424.501
	8914.521
5	424.501
6	424.501

After the test, soil samples were taken from the resultant crater. There appeared to be three characteristic soils comprising the crater, descriptively labeled in Reference 10 as sand, Caliche A, and Caliche B. Laboratory measurements on each of these soil types are summarized in Table 4 (Reference 10).

The relative permittivity of the soil in the lab fixture is

$$\varepsilon_f^* = K_f - i \left[K_f \tan \delta_o + \frac{\sigma_o}{\varepsilon_o \omega} \right] = \varepsilon_f' - i \, \varepsilon_f'' \tag{82}$$

where the subscript f denotes values in the lab fixture. Let us assume a linear variation of K_f with frequency. Then for the 8 transmission frequencies, the lab permittivities are given in Table 5.

Next we apply the mixing rule to the lab permittivities to calculate the permittivities of the individual dust grains. In this case, the mixture permittivities are known and we want to solve for one of the

42

Table 4. Lab test results for the crater soils.

Sample	Density Measurements		Electrical Measurements of Soil in Lab Fixture			
	Density in Lab Fixture (g cm^{-3})	Soil Grain Density (g cm^{-3})	Dielectric Constant		tan δ_0	σ_0 (mho m^{-1})
			1 GHz	10 GHz		
Sand	1.521	2.56	2.9	2.5	0.025	0.0024
Caliche A	1.207	2.64	2.8	2.4	0.024	0.0031
Caliche B	1.472	2.64	3.0	2.7	0.021	0.0014

constituents, so Equation 77 is used. In the lab fixture we consider the soil mixture to be composed of dust grains and air. The grains are conducting and in contact with each other, so that the grains are the continuous medium and the air is the disperse phase. Thus in Equation 77,

$$\varepsilon_m^* = \varepsilon_g^* \text{ (grain permittivity)}$$

$$\varepsilon_d^* = 1.0 - i(0) \text{ (air permittivity)}$$

$$\varepsilon^* = \varepsilon_t^* \text{ (lab permittivities)}$$

$$\phi = \frac{\text{air volume}}{\text{total volume}} = 1 - \frac{\text{lab soil density}}{\text{grain density}} = \begin{cases} 0.4059 \text{ (sand)} \\ 0.5428 \text{ (Caliche A)} \\ 0.4424 \text{ (Caliche B)} \end{cases}$$

The results for the dust grain permittivities and indices of refraction are given in Table 6.

Table 5. Lab permittivities for the transmission frequencies.

Frequency (MHz)	Lab Permittivities					
	Sand		Caliche A		Caliche B	
	ϵ'_f	ϵ''_f	ϵ'_f	ϵ''_f	ϵ'_f	ϵ''_f
378.608	2.93	0.187	2.83	0.215	3.02	0.130
413.028	2.93	0.178	2.83	0.203	3.02	0.124
424.501	2.93	0.175	2.83	0.199	3.02	0.123
447.447	2.92	0.169	2.82	0.192	3.02	0.120
1 273.503	2.89	0.106	2.79	0.111	2.99	0.0826
2 891.196	2.82	0.0854	2.72	0.0846	2.94	0.0704
8 914.512	2.55	0.0686	2.45	0.0651	2.74	0.0604
10 188.024	2.49	0.0665	2.39	0.0628	2.69	0.0590

Table 6. Dust grain permittivities and indices of refraction.

Frequency (MHz)	Sand				Caliche A				Caliche B			
	ϵ'_g	ϵ''_g	m_R	m_I	ϵ'_g	ϵ''_g	m_R	m_I	ϵ'_g	ϵ''_g	m_R	m_I
378.608	4.84	0.395	2.20	0.0897	6.20	0.665	2.49	0.133	5.40	0.302	2.32	0.0649
413.028	4.84	0.376	2.20	0.0854	6.20	0.628	2.49	0.126	5.40	0.288	2.32	0.0614
424.501	4.84	0.370	2.20	0.0839	6.20	0.616	2.49	0.124	5.40	0.286	2.32	0.0614
447.447	4.82	0.357	2.20	0.0812	6.17	0.594	2.49	0.119	5.40	0.279	2.32	0.060
1 273.503	4.76	0.224	2.18	0.0513	6.07	0.343	2.46	0.0695	5.33	0.192	2.31	0.0415
2 891.196	4.61	0.180	2.15	0.0419	5.86	0.261	2.42	0.0538	5.21	0.163	2.28	0.0357
8 914.512	4.04	0.143	2.01	0.0356	5.03	0.198	2.24	0.0442	4.75	0.139	2.18	0.0314
10 188.024	3.92	0.139	1.98	0.0350	4.85	0.191	2.20	0.0433	4.63	0.136	2.15	0.0315

Using the dust grain indices of Table 6, we next calculate the propagation properties of the DICE THROW dust cloud. First we assume that the long wavelength limit obtains and that scattering is insignificant compared to absorption. We can then use the mixing rule to calculate the index of refraction of the cloud and use Equations 71 and 72 to find the phase shift and attenuation coefficient. We use the mixing rule of Equation 76 with the dust grains dispersed in air. Take the dust density in the cloud to be 10^{-2} g cm^{-3}; this is the estimated value of the dust density when the cloud had a diameter of about 100 m. Table 7 gives the permittivities and indices of refraction of the dust cloud. Equations 71 and 72 are now used to calculate the propagation properties of the cloud. We convert the linear coefficients into mass penetrated coefficients by dividing by the cloud dust density. These mass penetrated values can then be used for any cloud density. Table 8 shows the results.

As an example of the use of the propagation parameters, we consider a 100 m ray path through a cloud of average dust density of 10^{-2} g cm^{-3}. This corresponds to a mass penetrated value of 10^{6} g m^{-2}. If the dust were composed of sand, then the dust-induced phase shift and attenuation would be 2.78 rad and 1.05 dB at 378.608 MHz and 65.1 rad and 15.5 dB at 10188.024 MHz.

Next we use the full Mie calculation. We use the dust grain indices of refraction of Table 6 and the WEPH power-law size distribution described in the previous section. The exact power-law exponent for the DICE THROW dust cloud is not known, but is thought to lie between the values 4 and 5. In order to prevent damage to the experimental equipment from large soil missiles thrown out by the blast, an annular ring of in situ soil around the explosive was removed and replaced with sand. The dust cloud particles are biased toward small particles. The Mie extinction and absorption coefficients are shown in Table 9 for power-law exponents of 3.5 ("hard rock"), 4.0 ("unconsolidated soils"), and 4.5 ("fine soils"). The Mie scattering coefficient is the difference between the extinction and absorption coefficients. At the lower

Table 7. Dust cloud ($\rho = 10^{-2}$ g cm^{-3}) permittivities and indices of refraction.

Table 8. Dust cloud propagation properties from mixing rule.

Table 9. Mie extinction and absorption coefficients for DICE THROW dust cloud.

frequencies and smaller particle distributions (larger p), the extinction is due entirely to the absorption and is the same (within our computational accuracy) as that of Table 8 calculated by the simple mixing rule. At the higher frequencies and larger particle distributions (smaller p), the dust particles are no longer small compared to the wavelength. Scattering becomes more important and dominates the extinction. Serious errors would result if the simple mixing rule were used to calculate the extinction for these cases.

In the DICE THROW dust cloud transmission experiments, both phase shift and extinction were measured. Figure 4 from Reference 10 shows the phase shifts on transmission path 1 as a function of time for the three lowest frequencies. We will assume that the cloud is composed primarily of sand particles with a power-law size distribution exponent of 4.5. Using the phase shift parameters from Table 8 and the phase shifts of Figure 4, we can calculate the mean mass penetrated as a function of time. We ignore the scintillations about the mean phase shift line.

Figure 5 shows the mean mass penetrated. We use the mass penetrated time history and the Mie extinction coefficients for sand and p = 4.5 of Table 9 to calculate the mean extinction as a function of time and frequency. Figure 6 shows the measured attenuations (Reference 10) and our calculated values. The data show strong scintillations about the mean absorption. Our calculated mean values show reasonable agreement at the lowest and highest frequencies, but do not produce enough attenuation at the intermediate frequencies. As we speculated earlier, the missing attenuation at the intermediate frequencies may be due to the combustion products of the 628 tons of ANFO in the cloud which we have neglected. Another possibility is that the size distribution of the dust particles may not be well represented by a p = 4.5 power law distribution. Because part of the native soil was removed and replaced with sand, the resulting dust particle size distribution may be abnormal.
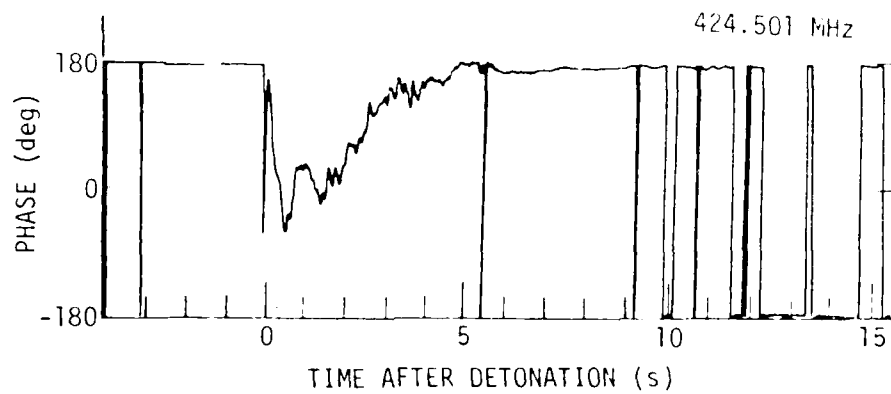
Figure 4. UHF phases for transmission path 1.
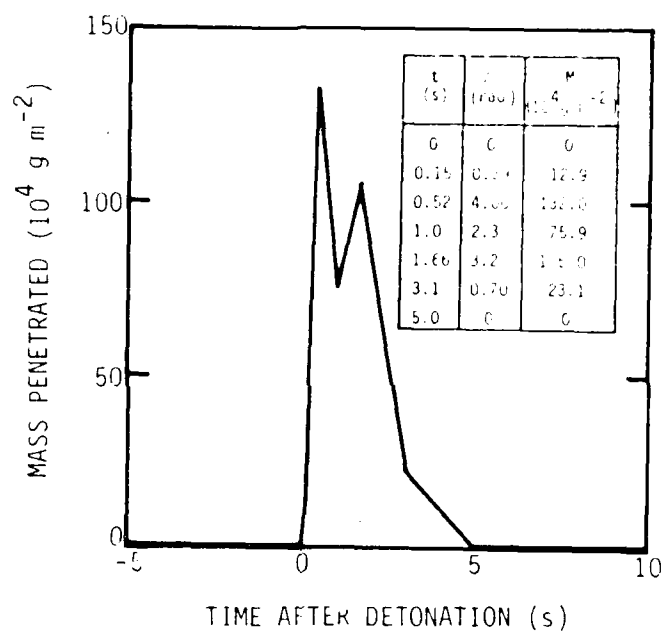
Figure 5.   Mass penetrated on transmission path 1.
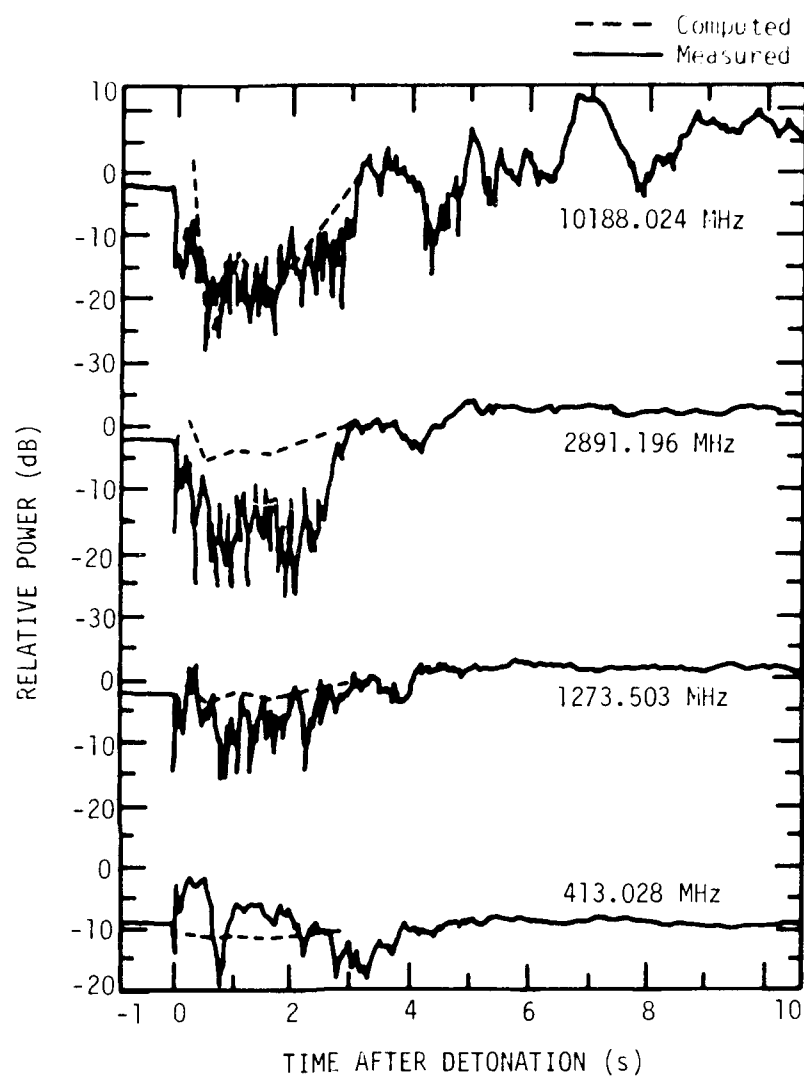
Figure 6.   Computed and measured attenuations
for transmission path 1.

SECTION 5

DUST MODELS FOR THE STEM
AND PRECURSOR PEDESTAL REGIONS

Theoretical investigations of dust in a nuclear environment have been carried out for many years at many different companies, including SAI (Science Applications Inc.), IITRI (Illinois Institute of Technology Research Institute), ATI (Applied Theory Inc) and S^3 (Systems, Science, and Software) (see References 11 to 18). The mechanisms of dust generation and transport have been studied. Dust generation includes crater ejecta, dust "popcorned" from the surface due to the thermal pulse of the device (with a minor contribution due to the neutron output), and the subsequent "scouring" of additional dust from the surface due to the outgoing shockwave and the inrushing afterwinds. Transport involves following the motion of the dust after generation, both within and outside the fireball.

The general technique in the transport studies is the following:

1. Assume an initial dust mass distribution in space and a particle size distribution. The initial mass distribution can come from the dust generation results or from empirical models.

2. Obtain a model for the air density and velocity flow fields as a function of time. Both large hydrodynamic codes (such as HULL and SHELL) and idealized models (such as Hill's spherical vortex) have been used to specify the fields.

3. Follow the motion of a large number of individual particles in the flow fields. The number and size of the particles are chosen so as to give good statistics for size distribution and mass density. The particles are assumed not to affect the flow fields. The particle motion is followed under the effects of gravity and drag (from the flow).

52

Using results from nuclear test experiments, HE experiments, and the theoretical studies, GE-TEMPO developed a systems model for the dust within the fireball (Reference 18). This model was used in the RANC and WEPH nuclear weapon effects codes, and was subsequently adopted for the ROSCOE systems code. Besides the fireball region, the stem and pedestal regions also contain dust. Figure 7 shows an artist's sketch of a surface or near-surface nuclear detonation. There now exist sufficient data, both theoretical and experimental, for the development of a systems model for the dust within the stem and pedestal regions. In this section we develop such a model.
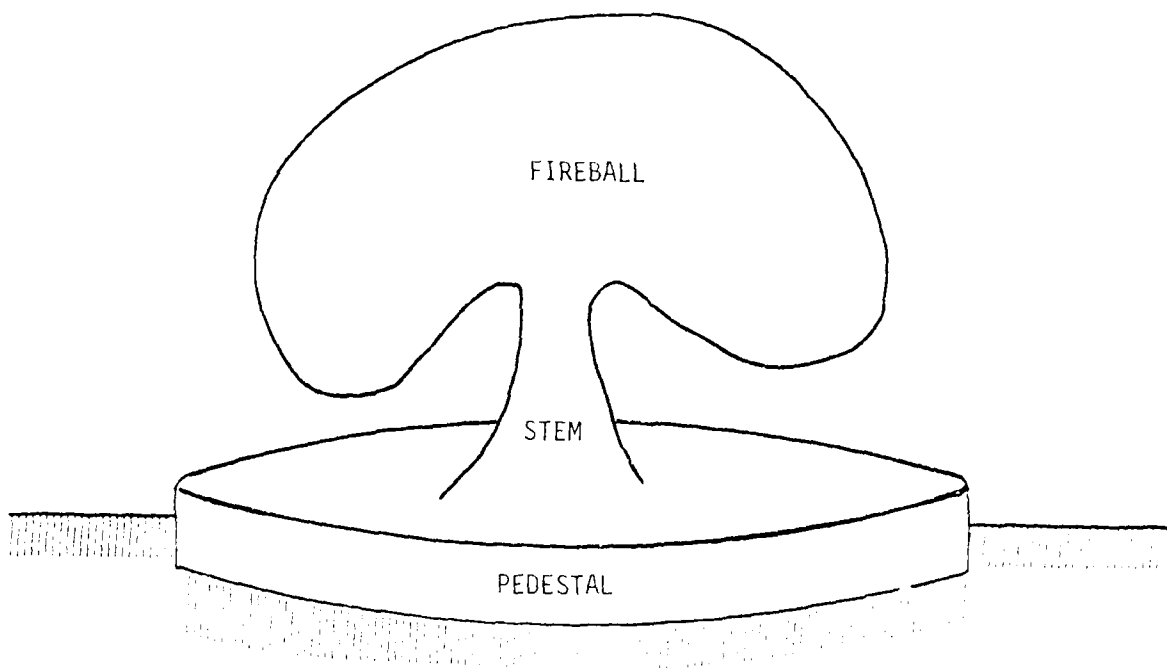

Figure 7. Sketch of the nuclear dust regions.

We first consider the dust pedestal region. A typical pedestal region will extend out to about three initial fireball radii and be 50 to 100 meters thick, containing roughly 0.03 MT of dust per MT of yield (Reference 11). The formation of a large dust pedestal region is a unique characteristic of a nuclear detonation. About 40 percent of the total yield of a nuclear detonation is emitted from the fireball in the form of thermal radiation. The soil surface around the fireball region is irradiated by this thermal flux. The weapon neutron and X-ray output may also irradiate the soil surface; but the range of these outputs is so short that the affected soil is within the fireball or stem regions, and so they do not contribute to pedestal function. The thermal irradiation causes the top 0.3 to 1 mm layer of soil to be thrown off, forming a low-lying dust layer. For wet soils, steam production is probably the throw-off mechanism. For dry soils, a "pop-corning" effect is observed, probably due to the release of hydrated water (Reference 12).

The air in this low-lying dust region is heated by a variety of mechanisms. There is conduction from the hot soil surface, convection within the layer, steam production in the case of wet soils, and conduction heat from the hot thrown-up soil particles. Once the dust layer is formed, the dust particles absorb the incident thermal radiation and efficiently transfer the absorbed heat to the air by conduction. The net result is the formation of a thin, hot, dusty air layer above the surface. Sound propagates faster in heated air. As the blast-produced shock wave propagates outward from the burst, that portion of the shock propagating in the heated region travels faster than the main shock; it becomes the shock precursor. Figure 8 from Reference 12 shows a sketch of the shock behavior. The outrunning shock wave scours some additional dust from the soil surface. The formation of a shock precursor causes large vertical air velocities behind the shock front which carry the dust upward 50 to 100 meters.

The dust production from a conventional explosion differs significantly from that of a nuclear explosion. Conventionally, there is no hot air layer existing before the shock arrival. The outrunning shock

54

Incident Shock

Precursor

Sweep-Up
Dust Cloud

Range

Altitude

Blast-Wave Precursor

Fireball

Mixture of hot blow-off
material and ambient air

Range

Altitude

Pre-Shock Thermal Blow-Off
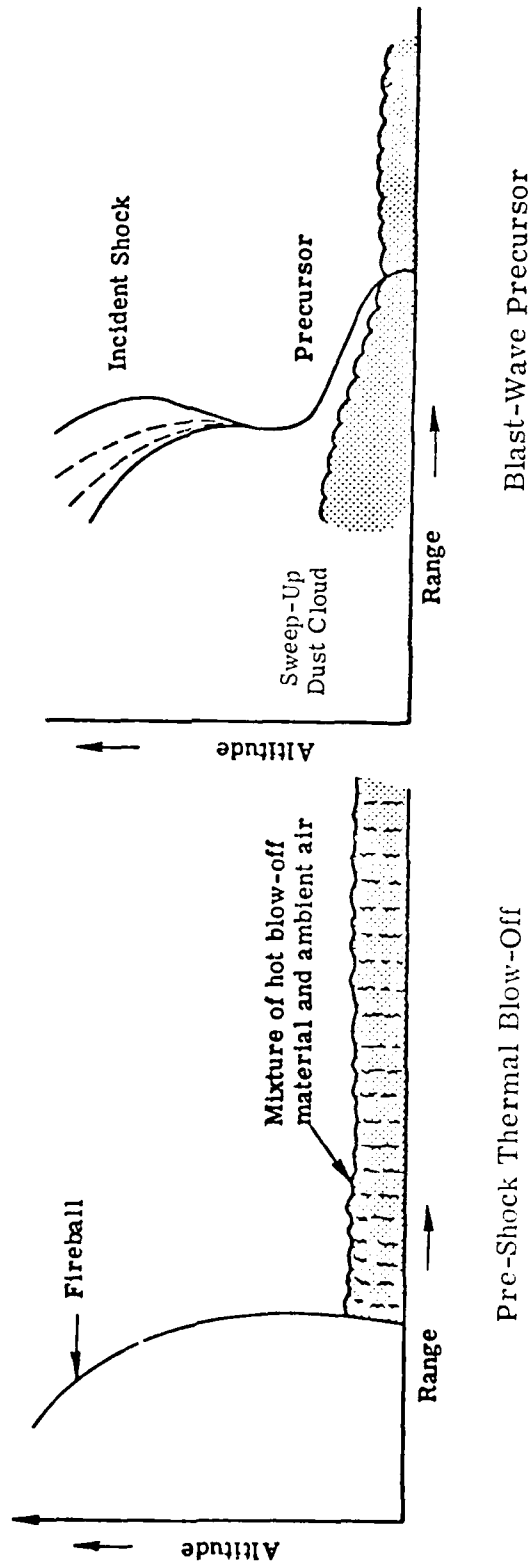
Figure 8.   Nuclear blast precursor development.

can scour dust from the surface, but there are no precursor-induced vertical velocity components to carry the dust to relatively high altitudes. Thus the total dust production is proportionally less and the dust is confined to the near surface layer. The nuclear-produced dust is truly a "precursor" pedestal.

For the development of our systems model for the dust pedestal, we rely primarily upon the work reported in References 11, 12, and 13. In these reports the authors have studied the pedestal formation and time history from both a theoretical and experimental approach. The experimental data consists primarily of photographic records of nuclear test events at the Nevada Test Site; there are also a few dust density measurements.

We begin with the geometrical modeling of the dust pedestal. From test observations, the thermally produced dust layer is rapidly lofted to its maximum altitude after passage of the shock wave. The radius grows out to a fairly well defined maximum radius (where the shock becomes too weak to loft the dust). Figure 9 from Reference 12 shows the time history of some typical dust profiles predicted by the PREDUM code. SAI approximates the final pedestal dust cloud by the simple geometry shown in Figure 10. Utilizing the photographic data, an empirical model for R_{MAX} and R'_{MAX} was developed in Reference 12. This model is shown in Figure 11; also shown is an estimate of R_{MIN} developed from PREDUM calculations. For our pedestal model we choose the simple geometry of an annular cylinder; the inner radius is taken as the stem radius. Our geometry is shown in Figure 12.

As the burst altitude is increased above the ground surface, the thermal flux at the ground and the strength of the outrunning shock wave become weaker. Eventually an altitude is reached at which no precursor is formed. Reference 12 estimates that this point is reached at an altitude of about

$$H_{MAX}(ft) = 675 \ W^{1/3} \ (KT) \ .$$

(8.5a)
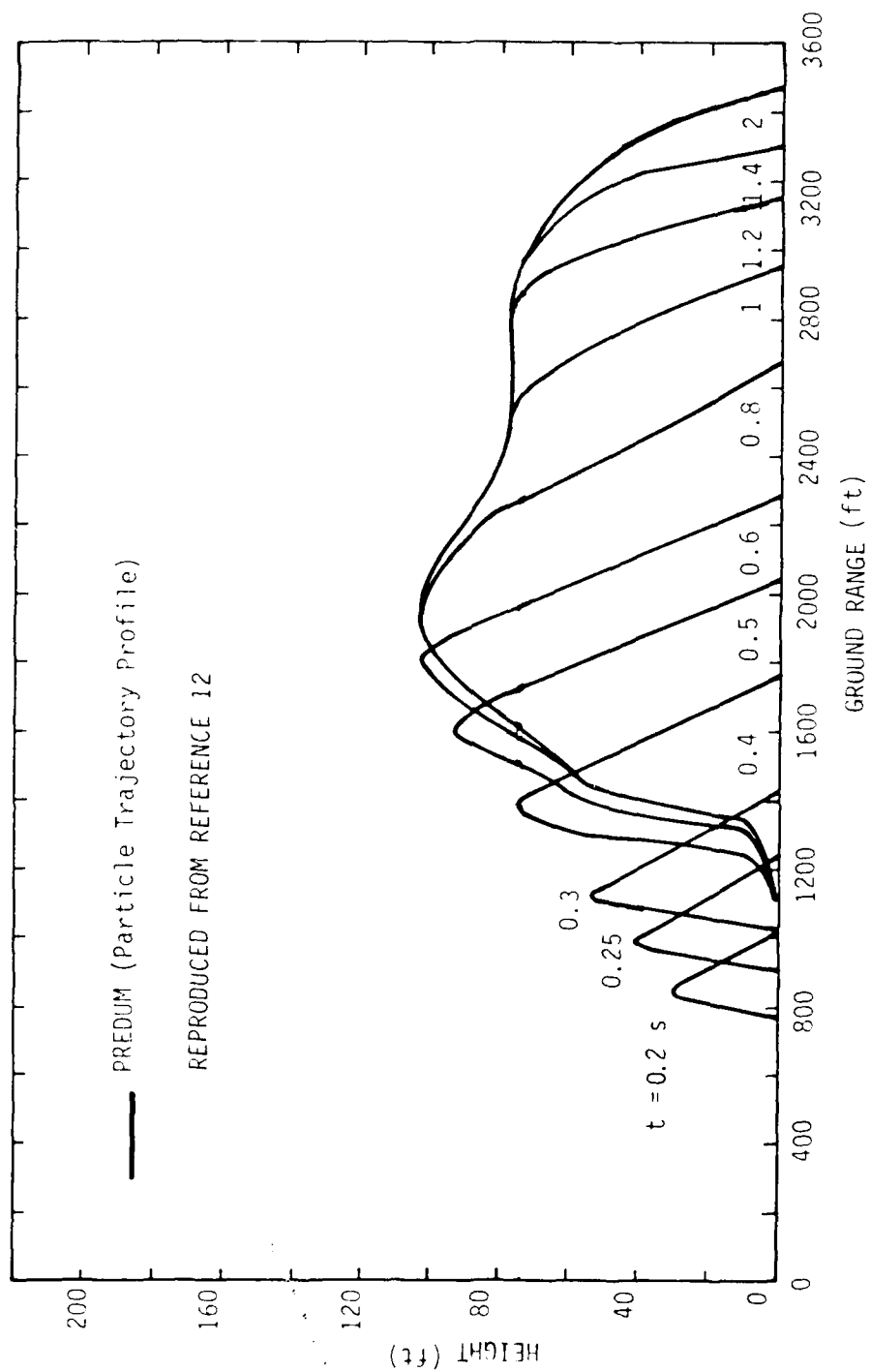
Figure 9.   Shot PRISCILLA—sweep-up dust layer profile predictions at various times.
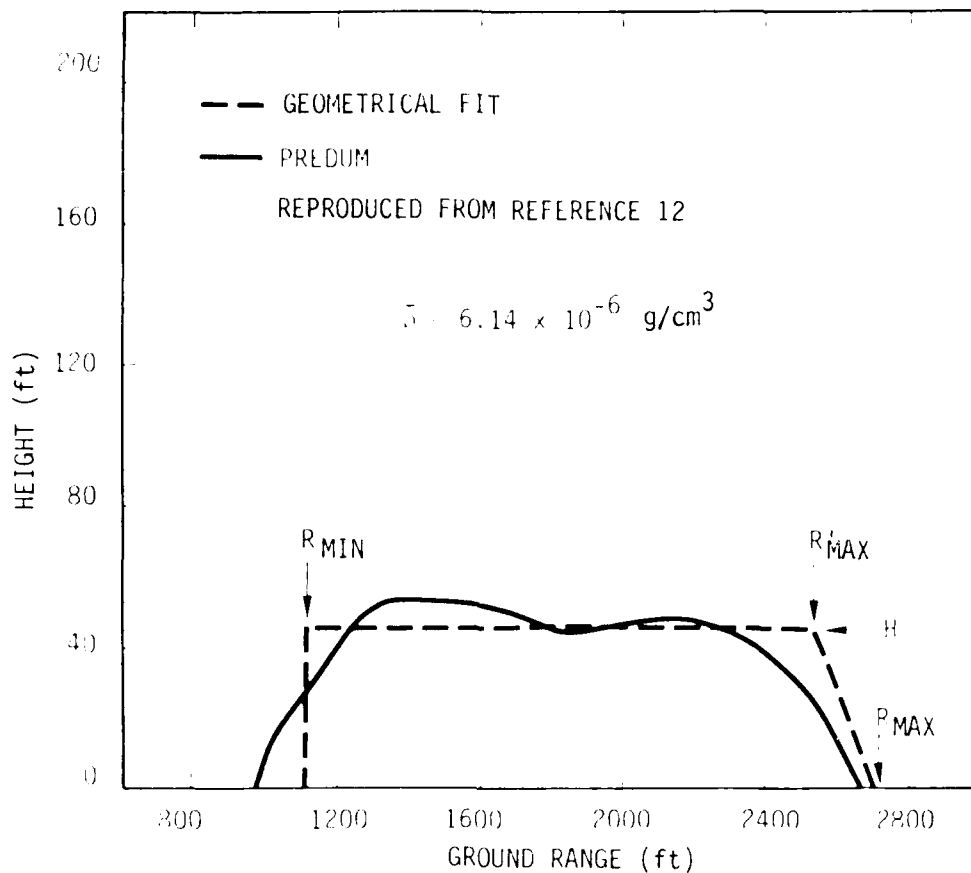
Figure 10. PREDUM predictions for shot DOG and simplified geometrical fit.

The units customarily used in the stem and pedestal references are feet for distance and kilotons for yield. The working units of most weapons effects codes such as WEPH are kilometers for distance and megatons for yield. We will generally write the same equation twice, once in each set of units. The distance and yield units will be explicitly indicated within the equation; the units of the other variables which do not change will not be explicitly indicated in the equation, but will be specified elsewhere. Thus the maximum altitude above which no precursor is formed is also written as

$$H_{MAX}(km) = 2.06 \, W^{1/5}(MT) \quad . \tag{85b}$$
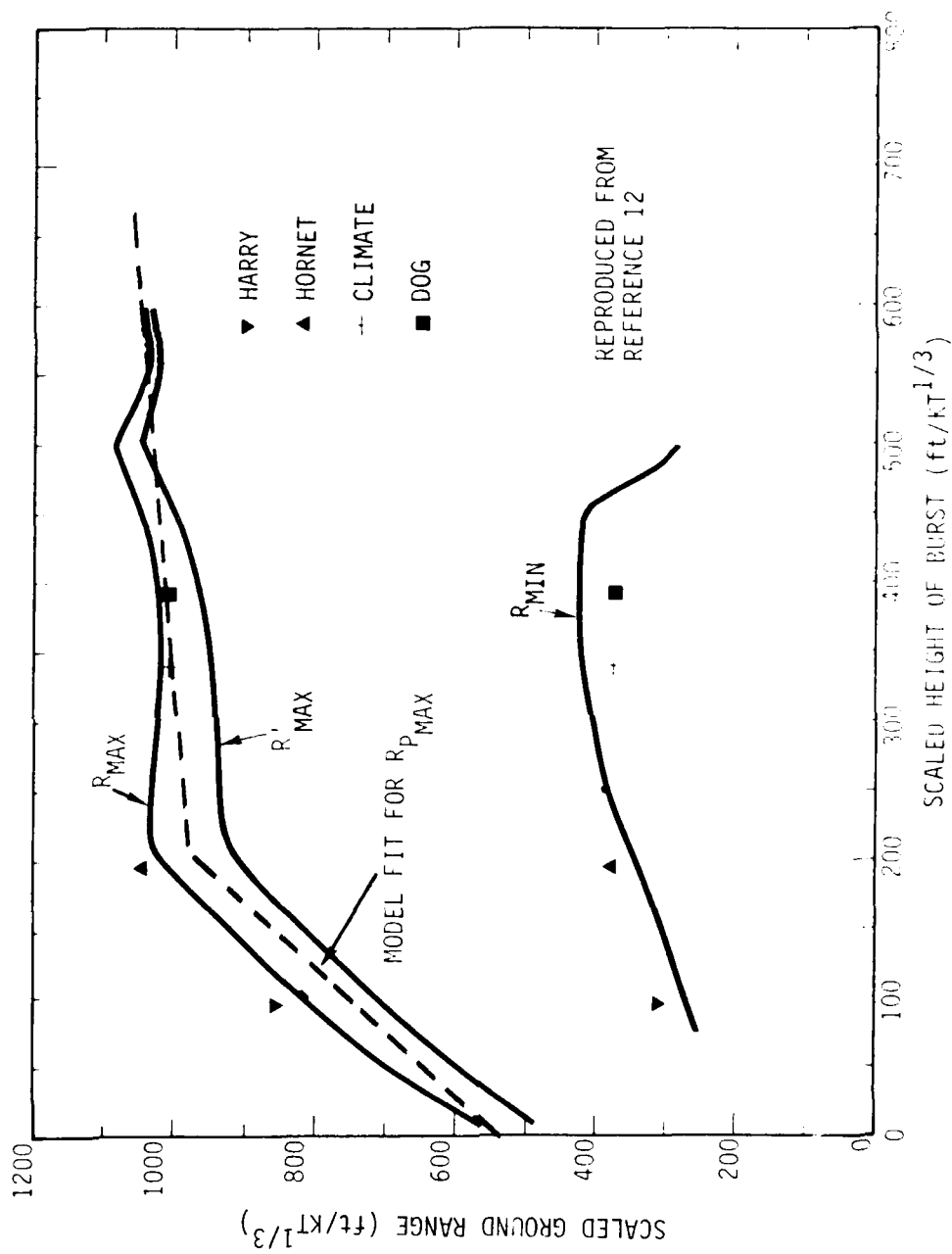
Figure 11. Stabilized sweep-up dust cloud radii, R_{MIN}, R'_{MAX}, and R_{MAX}.
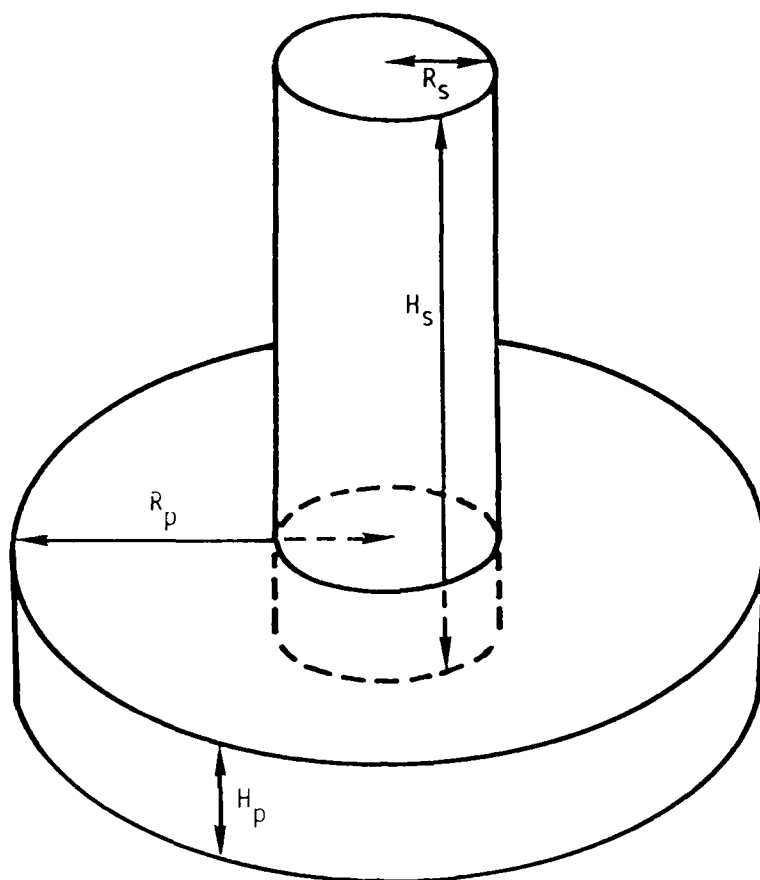
Figure 12.   Pedestal and stem geometry.

In our model we will assume that no dust pedestal is formed for bursts whose detonation altitude is above H_{MAX}.

For the maximum radius reached by the dust pedestal, we take a simple two-segment linear fit intermediate between the R_{MAX} and R'_{MAX} curves of Figure 11.   The fit is

$$R_{P_{MAX}}(ft) = \begin{cases} 2.2H_B(ft) + 525W^{1/3}(KT) & 0 \leq H_B(ft) \leq 205W^{1/3}(KT) \\ 0.16H_B(ft) + 942W^{1/3}(KT) & 205W^{1/3}(ft) \leq H_B(ft) \leq 675W^{1/3}(KT) \end{cases} \tag{84a}$$

60

$$R_{P_{MAX}}(km) = \begin{cases} 6.71 \times 10^{-4} \, H_B(km) + 1.60 \, W^{1/3}(MT) & 0 \le H_B(km) \le 0.625 W^{1/3}(MT) \\ 4.88 \times 10^{-5} \, H_B(km) + 2.87 \, W^{1/3}(MT) & 0.625 W^{1/3}(MT) \le H_B(km) \le 2.06 W^{1/3}(MT) \end{cases}$$

$$(84b)$$

Figure 13 from Reference 12 shows the estimates for the height of the final pedestal dust cloud; shown are the test data points, the "best estimate" (empirical model), and the PREDUM code predictions. We adopt the following fit (also shown on Figure 13):

$$H_{P_{MAX}}(ft) = 40 W^{1/3}(KT) \; \exp\left[-2.05 \times 10^{-3} \cdot \frac{H_B(ft)}{W^{1/3}(KT)}\right] \tag{85a}$$

$$H_{P_{MAX}}(km) = 0.122 \, W^{1/3}(MT) \; \exp\left[-0.673 \, \frac{H_B(km)}{W^{1/3}(MT)}\right] . \tag{85b}$$

We will model the time history of the pedestal radius as it grows from the stem radius to its maximum radius. We ignore the short build-up time that it takes the dust to reach its maximum altitude, and take the pedestal height as a constant equal to $H_{P_{MAX}}$. Consider a burst at an altitude low enough for a precursor to be formed. The shock wave travels downward from the burst point, intersects the ground, and then travels outward along the ground surface. The precursor forms and the dust pedestal is generated. We take as the pedestal outer radius time history,

$$R_P(t) = \begin{cases} 0 & t \le t_{SH} \\ R_{SH}(t) & t_{SH} \le t \le t_{pr} \\ R_{SH}(t_{pr}) + \left[R_{P_{MAX}} - R_{SH}(t_{pr})\right]\left[1 - 0.95 e^{-\frac{t - t_{pr}}{t_e}}\right] & t \ge t_{pr} \end{cases}$$

$$(86)$$

where

t_{SH} = time of arrival of the shock at the ground (s)

61
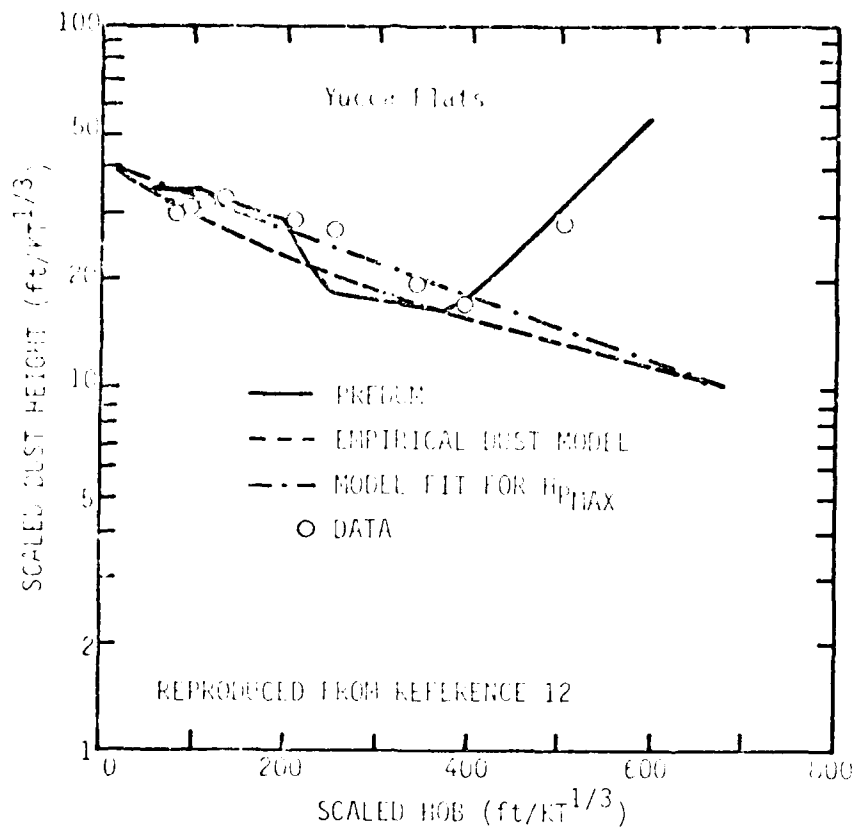
Figure 13. Dust height predictions (PREDUM) compared to empirical dust model and data.

$R_{SH}(t)$ = ground range of the shock wave (ft and km)

t_{pr} = time at which the precursor forms (s)

t_c = time constant which determines the rate at which the final radius is reached (s).

In our model there is no dust pedestal until

$$R_p(t) > R_S(t) \quad ,$$

where $R_S(t)$ is the radius of the stem and the inner radius of the pedestal ($R_S(t)$ will be given later). The equation for $R_p(t)$ for $t \geq t_{pr}$ is of the form given in Reference 13.

The slant range from the burst point to the shock front is

62

$$L = \sqrt{R_{SH}^2(t) + H_B^2} \quad . \tag{87}$$

Define a scaled slant range as

$$S = \frac{L(ft)}{W^{1/3}(KT)} = \frac{528.1 \, L(km)}{W^{1/3}(MT)} \quad . \tag{88}$$

Then the time in seconds at which the shock front reaches ground radius R_{SH} is given in Reference 15 as

$$t(R_{SH}) = \begin{cases} 3.595 \times 10^{-5} \, S^{5/2} \, T_W & S < 100 \\[4mm] \dfrac{0.5429 - 2.1185 \times 10^{-3}S + 3.618 \times 10^{-4}S^2 + 2.585 \times 10^{-6}S^3}{1 + 2.048 \times 10^{-3}S + 2.6872 \times 10^{-6}S^2} T_W & S > 100 \end{cases} \tag{89}$$

where

$$T_W = 10^{-5}W^{1/3}(KT) = 10^{-2}W^{1/3}(MT) \quad . \tag{90}$$

This expression is a fit to the shock radius history as calculated by a shock hydrocode. The time of arrival of the shock at the ground is obviously given by

$$t_{SH} = t(0), \text{ i.e., } S = \frac{H_B(ft)}{W^{1/3}(KT)} = \frac{528.1 \, H_B(km)}{W^{1/3}(MT)} \quad . \tag{91}$$

We take

$$R_{SH}(t) = 130W^{1/3}(KT) \, ft \tag{92a}$$

$$R_{SH}(t) = 0.2W^{1/3}(MT) \, km \quad . \tag{92b}$$

Hence

63

$$t_{pr} = t(R_{SH}(t_{pr})) \quad , \quad \text{ie}, \quad S = \sqrt{(140)^2 + \left(\frac{H_B(\text{ft})}{W^{1/3}(\text{KT})}\right)^2}$$

$$= \sqrt{(140)^2 + \left(\frac{328.1 \ H_B(\text{km})}{W^{1/3}(\text{MT})}\right)^2} \quad . \tag{93}$$

We can invert Equation 89 to find the shock front radius as a function of time. Define a scaled time

$$\iota = \frac{t}{T_W} \quad . \tag{94}$$

Then inverting Equation 89,

$$S(t) = \begin{cases} 59.954\iota^{2/5} & \iota \leq 5.595 \\ \\ \dfrac{61.94 + 15.89\iota + 0.1782\iota^2 + 2.035 \times 10^{-4}\iota^3}{1 + 5.871 \times 10^{-2}\iota + 1.806 \times 10^{-4}\iota^2} & \iota \geq 5.595 \end{cases} \tag{95}$$

and from Equations 87 and 88,

$$R_{SH}(t) = \sqrt{\left(S(t)W^{1/3}(\text{KT})\right)^2 - H_B^2(\text{ft})} \qquad \text{ft} \tag{96a}$$

$$R_{SH}(t) = \sqrt{\left(\frac{S(t)W^{1/3}(\text{MT})}{328.1}\right)^2 - H_B^2(\text{km})} \qquad \text{km} \quad . \tag{96b}$$

Reference 13 gives the time constant t_e as

$$t_e = \begin{cases} \left[0.206 - 0.146\left(1 - \dfrac{H_B(\text{ft})}{255W^{1/3}(\text{KT})}\right)\right]W^{1/3}(\text{KT}) & H_B(\text{ft}) \leq 255W^{1/3}(\text{KT}) \\ \\ 0.206W^{1/3}(\text{KT}) & H_B(\text{ft}) > 255W^{1/3}(\text{KT}) \end{cases} \tag{97a}$$

$$t_e = \begin{cases} \left[2.06 - 1.46\left(1 - \dfrac{1.40H_B(\text{km})}{W^{1/3}(\text{MT})}\right)\right]W^{1/3}(\text{MT}) & H_B(\text{km}) \leq 0.716W^{1/3}(\text{MT}) \\[4mm] 2.06W^{1/3}(\text{MT}) & H_B(\text{km}) > 0.716W^{1/3}(\text{MT}) \end{cases} \tag{97b}$$

Figure 14 from Reference 12 shows the average dust density in the final dust cloud as a function of yield and altitude, as calculated by the PREDUM code. An excellent fit to the data is

$$\rho_f = \begin{cases} \dfrac{3.\_ \times 10^{-6}}{W^{1/3}(\text{KT})} \exp\left[9.0\_ \times 10^{-3}\,\dfrac{H_B(\text{ft})}{W^{1/3}(\text{ft})}\right] & 0 \leq H_B(\text{ft}) \leq 200W^{1/3}(\text{ft}) \\[4mm] \dfrac{1.1\_ \times 10^{-6}}{W^{1/3}(\text{KT})} \exp\left[9.1\_ \times 10^{-3}\,\dfrac{H_B(\text{ft})}{W^{1/3}(\text{ft})}\right] & 200W^{1/3}(\text{ft}) \leq H_B(\text{ft}) \\ & \leq 200W^{1/3}(\text{ft}) \quad \text{g cc}^{-3} \\[4mm] \dfrac{6.0\_ \times 10^{-6}}{W^{1/3}(\text{ft})} \exp\left[1.\_ \times 10^{-3}\,\dfrac{H_B(\text{ft})}{W^{1/3}(\text{ft})}\right] & 200W^{1/3}(\text{ft}) \leq H_B(\text{ft}) \\ & \leq 380W^{1/3}(\text{ft}) \\[4mm] \dfrac{3.6\_ \times 10^{-6}}{W^{1/3}(\text{ft})} \exp\left[\_ \times 10^{-3}\,\dfrac{H_B(\text{ft})}{W^{1/3}(\text{ft})}\right] & 380W^{1/3}(\text{ft}) \leq H_B(\text{ft}) \\ & \leq 625W^{1/3}(\text{ft}) \end{cases} \tag{98a}$$

$$\rho_f = \begin{cases} \dfrac{\_ \times 10^{-7}}{W^{1/3}(\text{MT})} \exp\left[\dfrac{H_B(\text{km})}{W^{1/3}(\text{MT})}\right] & 0 \leq H_B(\text{km}) < 0.625W^{1/3}(\text{MT}) \\[4mm] \dfrac{2.81 \times 10^{-7}}{W^{1/3}(\text{MT})} \exp\left[\_ \,\dfrac{H_B(\text{km})}{W^{1/3}(\text{MT})}\right] & 0.625W^{1/3}(\text{MT}) \leq H_B(\text{km}) \\ & \leq 0.792W^{1/3}(\text{MT}) \quad \text{g cc}^{-3} \\[4mm] \dfrac{1.5\_ \times 10^{-6}}{W^{1/3}(\text{MT})} \exp\left[0.5\_\,\dfrac{H_B(\text{km})}{W^{1/3}(\text{MT})}\right] & 0.792W^{1/3}(\text{MT}) \leq H_B(\text{km}) \\ & \leq 1.16W^{1/3}(\text{MT}) \\[4mm] \dfrac{9.11 \times 10^{-6}}{W^{1/3}(\text{MT})} \exp\left[\_.00\_\,\dfrac{H_B(\text{km})}{W^{1/3}(\text{MT})}\right] & 1.16W^{1/3}(\text{MT}) \leq H_B(\text{km}) \\ & \leq 2.06W^{1/3}(\text{MT}) \end{cases} \tag{98b}$$
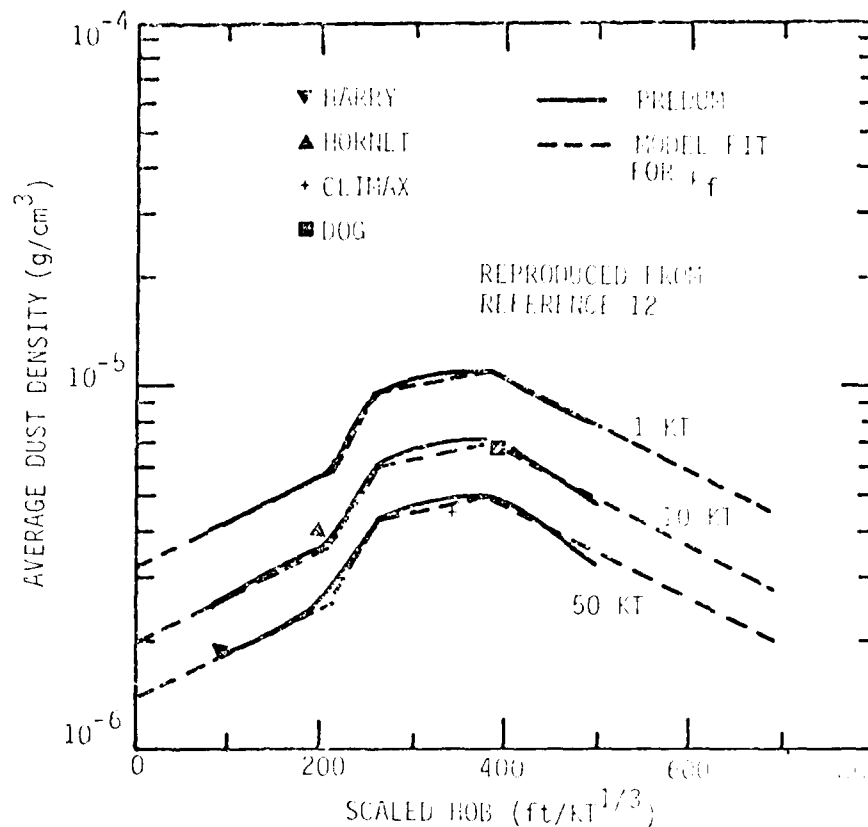
Figure 14. Average dust density in the final
dust pedestal.

What is the size distribution of the particles in the dust pedestal?
We are assuming that the particles came primarily from the top 0.5 to 1
mm of the soil surface, so the particles are small. We will assume that
the pedestal particles have the same size distribution as the fireball
dust particles, but that the maximum size particle in the pedestal is
1 mm (0.1 cm). For evaluation purposes the fireball dust size distribu-
tion is divided into eight size groups spanning particle diameters from
0.001 to 10 centimeters. We take the same small-size limit of 0.001
centimeters. For evaluations, we divide the pedestal dust sizes into
the four size groups given in Table 10. Since we are assuming the same
size distribution for the pedestal dust as for the fireball dust, we can
use the fireball dust attenuation and backscatter formulas for the
pedestal dust propagation.

Table 10. Pedestal dust sizes.

Group	Minimum Diameter of Particle in Group (cm)	Maximum Diameter of Particle in Group (cm)
1	0.001	0.004
2	0.004	0.01
3	0.01	0.04
4	0.04	0.1

As in the fireball case, we assume that each size group is uniformly distributed within its own (annular) cylindrical volume. All cylinders will be assumed to have the same radial dimensions at all times, inner radius $R_s(t)$ and outer radius $R_p(t)$. All cylinders will initially have the same altitude, $H_{p_{max}}$; after a suitable delay interval the height of each cylinder will be allowed to fall with its characteristic velocity. We do not have any data for the appropriate delay time before the dust particles begin to settle. We arbitrarily take the delay time to be 5 times the e-folding time of $R_p(t)$ in Equation 86,

$$t_{fp} = t_{pr} + 5t_e \quad .\tag{99}$$

The altitude history of each group cylinder is

$$(H_p)_i = \begin{cases} H_{p_{max}} & t \leq t_{fp} \\ H_{p_{max}} - v_{pi}(t - t_f) & t > t_{fp} \end{cases}\tag{100}$$

where v_{pi} is the characteristic fall velocity of size group i.

The terminal velocity equation of a spherical particle falling under gravity in still air is

$$\frac{3\rho_a C_D}{4\rho_p d} v^2 - g = 0 \quad ,\tag{101}$$

67

where

> V = terminal fall velocity
>
> ρ_a = ambient air density
>
> ρ_p = particle density
>
> d = diameter of spherical particle
>
> g = acceleration of gravity.

For a spherical dust particle we can use (Reference 11)

$$C_D = \frac{24}{R_e} + 0.44 \quad , \tag{102}$$

where R_e is the Reynolds number, given by

$$R_e = \frac{\rho_a V d}{\mu_a} \tag{103}$$

and μ_a is the air viscosity. Thus the velocity equation becomes

$$\frac{1}{3} \frac{\rho_a}{\rho_p d} V^2 + \frac{18\mu_a}{\rho_p d^2} V - g = 0 \quad , \tag{104}$$

which has the solution

$$V = \sqrt{\left(\frac{27 \, \mu_a}{\rho_a d}\right)^2 + \frac{3 g \rho_p d}{\rho_a}} - \frac{27\mu_a}{\rho_a d} \quad . \tag{105}$$

This terminal velocity equation is more familiar in the limits of large and small dust particles. For small dust particles ($d \lesssim 0.01$ cm)

$$C_D \approx \frac{24}{R_e} \quad \text{and}$$

$$V = \frac{g \rho_p d^2}{18\mu_a} \quad , \tag{106a}$$

which is Stokes law. For large dust particles ($d \gtrsim 0.1$ cm),

$$V = \sqrt{\frac{4\rho_p g d}{3\rho_a C_D}} \quad , \tag{106b}$$

which is the dynamic drag equation. We assume the following numerical
values:

$$\rho_a = 1.225 \times 10^{-3} \text{ g cm}^{-3} \text{ (sea-level air)}$$
$$\rho_p = 2.6 \text{ g cm}^{-3}$$
$$g = 980.6 \text{ cm s}^{-2}$$
$$\mu_a = 1.81 \times 10^{-4} \text{ poise} \quad .$$

With these values the terminal velocity equation becomes

$$V = \sqrt{\left(\frac{3.9894}{d}\right)^2 + 6.2438 \times 10^6 d} \;-\; \frac{3.9894}{d} \qquad \text{cm s}^{-1} \qquad (107)$$

where d is in cm. We assume that each size group falls with the terminal
velocity characteristic of the smallest particle in the group. The dust
particles are not spherical nor are they falling in calm air. Hence we
expect the effective fall velocity to be less than our simple calculation.
Taking the smallest particle in the group assures a slower rate. Table
11 gives the fall velocities for each size group.

Table 11. Fall velocities for pedestal dust size groups.

Group	Diameter of Smallest Particle in Group (cm)	Fall Velocity		
		cm s^{-1}	km s^{-1}	ft s^{-1}
1	0.001	0.782	7.82^{-6}	2.57^{-2}
2	0.004	12.4	1.24^{-4}	0.408
3	0.01	71.8	7.18^{-4}	2.36
4	0.04	410	4.10^{-3}	13.4

We next develop a systems model for the dust in the nuclear stem re-
gion. The stem region is more complicated to model than the pedestal re-
gion. For very-low-altitude bursts, the fireball itself intersects the
ground and dust is directly injected into the fireball. The fireball and
stem are connected and rise together; additional dust is injected into the

69

fireball via the stem. As the burst altitude is increased, the fire-
ball does not reach the ground surface. A dust stem is formed and
rises to intersect the rising fireball; dust is injected into the fire-
ball only via the stem. At still higher burst altitudes, the stem does
not reach the rising fireball; the fireball region is dust free. Even-
tually a high enough burst altitude is reached so that no stem is formed.

We take the geometry of the stem region to be cylindrical; see Figure
12. We begin by modeling the stem radius time history. Figure 15 from
Reference 14 shows the scaled stem radius as a function of scaled time
for a number of very-low-altitude bursts. These data were taken from
photographic data of the test events. We adopt the following fit to
the best-estimate curve shown on Figure 15:

$$
R_S(t) = \begin{cases}
505.4W^{0.2452}_{(KT)}t^{0.2705} & t \leq 0.42W^{1/3}_{(KT)} \\[2ex]
240W^{1/3}_{(KT)} & 0.42W^{1/3}_{(KT)} \leq t \leq 2.25W^{1/3}_{(KT)} \\[2ex]
104.5W^{0.5479}_{(KT)}t^{-0.6457} & 2.25W^{1/3}_{(KT)} \leq t \leq 5.5W^{1/3}_{(KT)} \quad \text{ft} \\[2ex]
48.0W^{0.1310}_{(KT)}t^{0.6070} & 5.5W^{1/3}_{(KT)} \leq t \leq 77W^{1/3}_{(KT)} \\[2ex]
670W^{1/3}_{(KT)} & t \geq 77W^{1/3}_{(KT)}
\end{cases}
\tag{108a}
$$

$$
R_S(t) = \begin{cases}
0.4962W^{0.2452}_{(MT)}t^{0.2705} & t \leq 4.2W^{1/3}_{(MT)} \\[2ex]
0.7315W^{1/3}_{(MT)} & 4.2W^{1/3}_{(MT)} \leq t \leq 22.5W^{1/3}_{(MT)} \\[2ex]
5.428W^{0.5479}_{(MT)}t^{-0.6457} & 22.5W^{1/3}_{(MT)} \leq t \leq 55W^{1/3}_{(MT)} \quad \text{km} \\[2ex]
0.05616W^{0.1310}_{(MT)}t^{0.6070} & 55W^{1/3}_{(MT)} \leq t \leq 770W^{1/3}_{(MT)} \\[2ex]
2.042W^{1/3}_{(MT)} & t \geq 770W^{1/3}_{(MT)}
\end{cases}
\tag{108b}
$$

There is no discernible variation of $R_S(t)$ with height of burst for the
limited altitude range of Figure 15. We assume therefore that there is
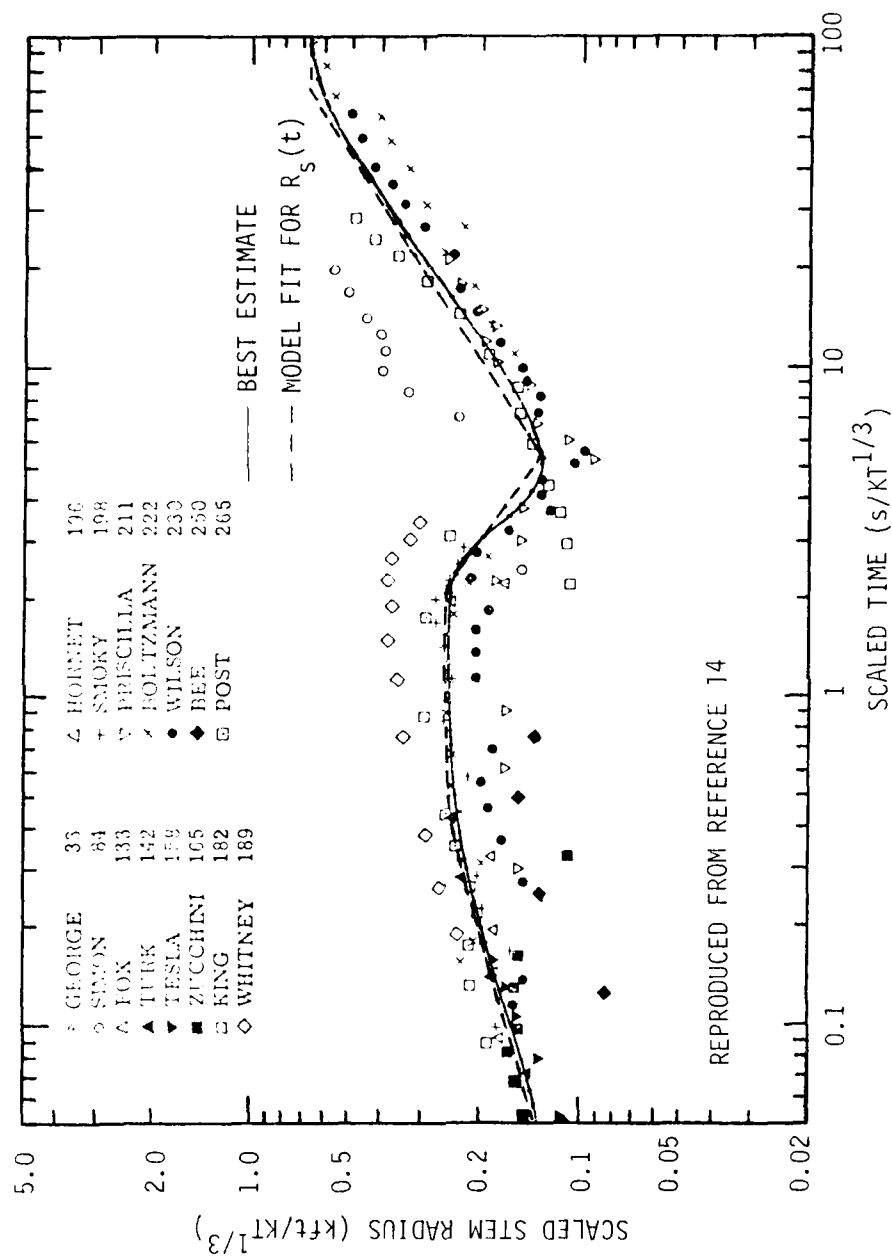
Figure 15. Scaled stem radius as a function of scaled time after burst for shots with scaled heights of burst in the range 33 to 265 feet.

71

no functional dependence upon height of burst for the whole narrow
altitude range for which a stem is formed. We restrict $R_S(t)$ to be the
minimum of that given in Equation 108 and the shock front radius of
Equation 96. Note that for a burst altitude less than $65.9W^{1/3}$ feet
$(0.2W_{(MT)}^{1/3}$ kilometers), the stem radius eventually expands enough to en-
gulf the entire dust pedestal.

Define a scaled height of burst of

$$h_{SB} = \frac{H_B}{R_{EQ}} , \qquad (109)$$

where

R_{EQ} = fireball pressure equilibrium radius (the radius of the
fireball when the fireball internal pressure falls to the
ambient atmospheric pressure).

Then from observations of nuclear test events, the following general state-
ments can be made about the rise behavior of the stem (Reference 18). For
scaled heights between about 2.5 to 3, there is no mixing of the fireball
proper and the surface dust layer. The stem does not begin rising until
20 to 30 seconds after detonation, giving the larger particles initially
lofted ample time to fall back. The rising dust column (the stem) does
not reach the rising fireball until a few minutes after burst. For scaled
burst heights greater than about 3, the column of rising dust does not
reach the rising fireball cloud before the cloud stabilizes (at about
7 minutes).

Based on a very limited set of test data, we adopt the following some-
what arbitrary model for the time history of the stem altitude. Let

$H_S(t)$ = altitude of the top of the stem (ft and km)

$H_{BOT}(t)$ = altitude of the bottom of the fireball (ft and km)

t_{FBS} = time at which the fireball stabilizes (s)

t_{IS} = time at which the rising stem intersects the fireball
bottom (s)

t_D = delay time before the stem starts to rise (s).

The stem altitude will always be limited by the fireball bottom altitude;

$$H_S(t) \leq H_{BOT}(t) \text{ at all times} \quad .$$

We assume there is no stem formation until the downward-traveling shock wave from the burst intersects the ground surface. We then let the altitude rise with the same velocity as the outrunning shock until the stem altitudes reaches either the dust-pedestal maximum altitude or the fireball bottom, depending upon the burst altitude. For bursts with $h_{SB} \leq 2$, take

$$H_S(t) = \begin{cases} 0 & t \leq t_{SH} \\ R_{SH}(t) & R_{SH}(t) \leq H_{BOT}(t) \\ H_{BOT}(t) & R_{SH}(t) > H_{BOT}(t) \end{cases} \quad (110)$$

where t_{SH} is given by Equation 91, R_{SH} by Equation 96, and H_{BOT} is given by the fireball phenomenology model. Thus for very low bursts, we let the stem rise until it intersects the fireball; it remains at the fireball bottom from then on.

For bursts with $h_{SB} > 2$, we take

$$H_S(t) = \begin{cases} 0 & t \leq t_{SH} \\ R_{SH}(t) & R_{SH}(t) \leq H_{P_{MAX}} \\ H_{P_{MAX}} & t \leq t_D \end{cases} \quad (111)$$

where $H_{P_{MAX}}$ is the maximum altitude reached by the dust pedestal and is given by Equation 85. For bursts above a scaled height of 2, we let the stem rise to the pedestal altitude and then hold it at that altitude for the delay time t_D. Take the delay time to be

$$t_D = \begin{cases} 0 & h_{SB} \leq 2 \\ 50 \ (h_{SB} - 2) & 2 \leq h_{SB} \leq 3 \\ 50 & h_{SB} > 3 \end{cases} \quad . \quad (112)$$

73

We simply let the delay time increase from 0 to 30 seconds as the scaled height of burst increases from 2 to 3.

After the delay time is over, the stem rises again. We assume that the stems for bursts with scaled heights between 2 and 3 rise and intersect the fireball bottom. We take the time of intersection as

$$t_{IS} = t_{FBS}[h_{SB} - 2] \qquad 2 \le h_{SB} \le 3 \quad . \tag{113}$$

For bursts with scaled altitudes between 3 and 6, we assume the stem does not reach the fireball, but stabilizes at a lower altitude given by

$$H_{S_{MAX}} = \frac{(6 - h_{SB})}{3} H_{BOT}(t_{FBS}) \qquad 3 \le h_{SB} \le 6 \quad . \tag{114}$$

For bursts with $h_{SB} > 6$ we assume no stem forms. As a comparison, the maximum scaled burst height for which a dust pedestal is formed is $h_{SB} \approx 2.6$. The WEPH fireball dust model assumes that dust is lofted into the fireball for bursts with $h_{SB} < 3$. Our stem model is consistent with the current fireball model. Table 12 gives the present model dust regions as a function of scaled burst height.

For $h_{SB} > 2$, define the average rise velocity V_S of the stem as it rises from the pedestal altitude to either the intersection with the fireball bottom ($2 \le h_{SB} \le 3$) or to its maximum altitude ($3 \le h_{SB} \le 6$):

$$V_S = \begin{cases} \dfrac{H_{BOT}(t_{IS}) - H_{P_{MAX}}}{t_{IS} - t_D} & 2 \le h_{SB} \le 3 \\[4mm] \dfrac{H_{S_{MAX}} - H_{P_{MAX}}}{t_{FBS} - t_D} & 3 \le h_{SB} \le 6 \end{cases} \tag{115}$$

We choose the simplest time rise history, namely a constant velocity rise

Table 12. Dust regions.

Scaled Burst Height (h_{SB})	Dust Regions
0 - 2.6	Stem, fireball, pedestal
2.6 - 3	Stem, fireball
3 - 6	Stem
> 6	No dust regions

$$2 \leq h_{SB} \leq 3$$

$$H_S(t) = \begin{cases} H_{P_{MAX}} + V_S(t - t_D) & t_D \leq t \leq t_{IS} \\ H_{BOT}(t) & t \geq t_{IS} \end{cases} \qquad (116)$$

$$3 \leq h_{SB} \leq 6$$

$$H_S(t) = \begin{cases} H_{P_{MAX}} + V_S(t - t_D) & t_D \leq t \leq t_{FBS} \\ H_{S_{MAX}} & t \geq t_{FBS} \end{cases} \qquad (117)$$

We have expressed the rise model as a function of scaled height of burst. For comparisons with the unscaled units, we can use the conversions

$$H_B(ft) = 263.7 W_{(KT)}^{1/3} h_{SB} \qquad (118a)$$

$$H_B(km) = 0.8038 W_{(MT)}^{1/3} h_{SB} \quad . \qquad (118b)$$

Next we model the dust densities in the stem region. We consider only that dust which is lofted by the air velocity flow fields. We ignore the crater ejecta and fallback. For scaled burst heights above about 0.05, the crater becomes a compaction crater with very little ejecta, so the lofted dust is entirely composed of material "popcorned" or scoured off the ground surface. For bursts low enough to form an

ejecta crater, the fireball intersects the ground; any systems dust ef-
fects would be completely obscured by the fireball itself. Only after
the fireball has risen sufficiently and before the ejecta falls back
would the stem ejecta be significant. The fireball dust model accounts
for the crater ejecta which is entrained into the rising fireball.
We lose little systems significance by ignoring the stem ejecta.

In Reference 14 the early-time lofted stem dust densities have been
estimated by combining VORDUM code predictions with the available photo-
graphic data of the stem time history. There are fairly large uncertainties
in the calculation of the stem densities. As would be expected, there are
no direct experimental measurements of the dust density in a nuclear stem
with which to compare the calculated estimates.

Figures 16 through 28 from Reference 14 show the estimated densities
for a range of burst yields and altitudes. The solid lines in the fig-
ures are the best estimates of the densities. There is no definite func-
tional dependence of dust densities upon height of burst evident from
the calculations; therefore we assume no height of burst dependence. We
adopt the best estimate curves as our primary data, and devise the
following fit. The curve fit is also shown in the figures for comparison.

Let

$$\rho_1 = \begin{cases} 5.2 \times 10^{-8} W_{(KT)}^{1/3} = 5.2 \times 10^{-7} W_{(MT)}^{1/3} & W \leq 5 \text{ MT} = 5000 \text{ KT} \\ 8.9 \times 10^{-7} \text{ g cm}^{-3} & W \geq 5 \text{ MT} = 5000 \text{ KT} \end{cases}$$

(119)

$$R_1(\text{ft}) = 240 W_{(KT)}^{1/3}$$ (120a)

$$R_1(\text{km}) = 0.732 W_{(MT)}^{1/3}$$ (120b)

ρ_1 is a characteristic density when the stem radius is R_1. The curve fit
to the stem density is

76
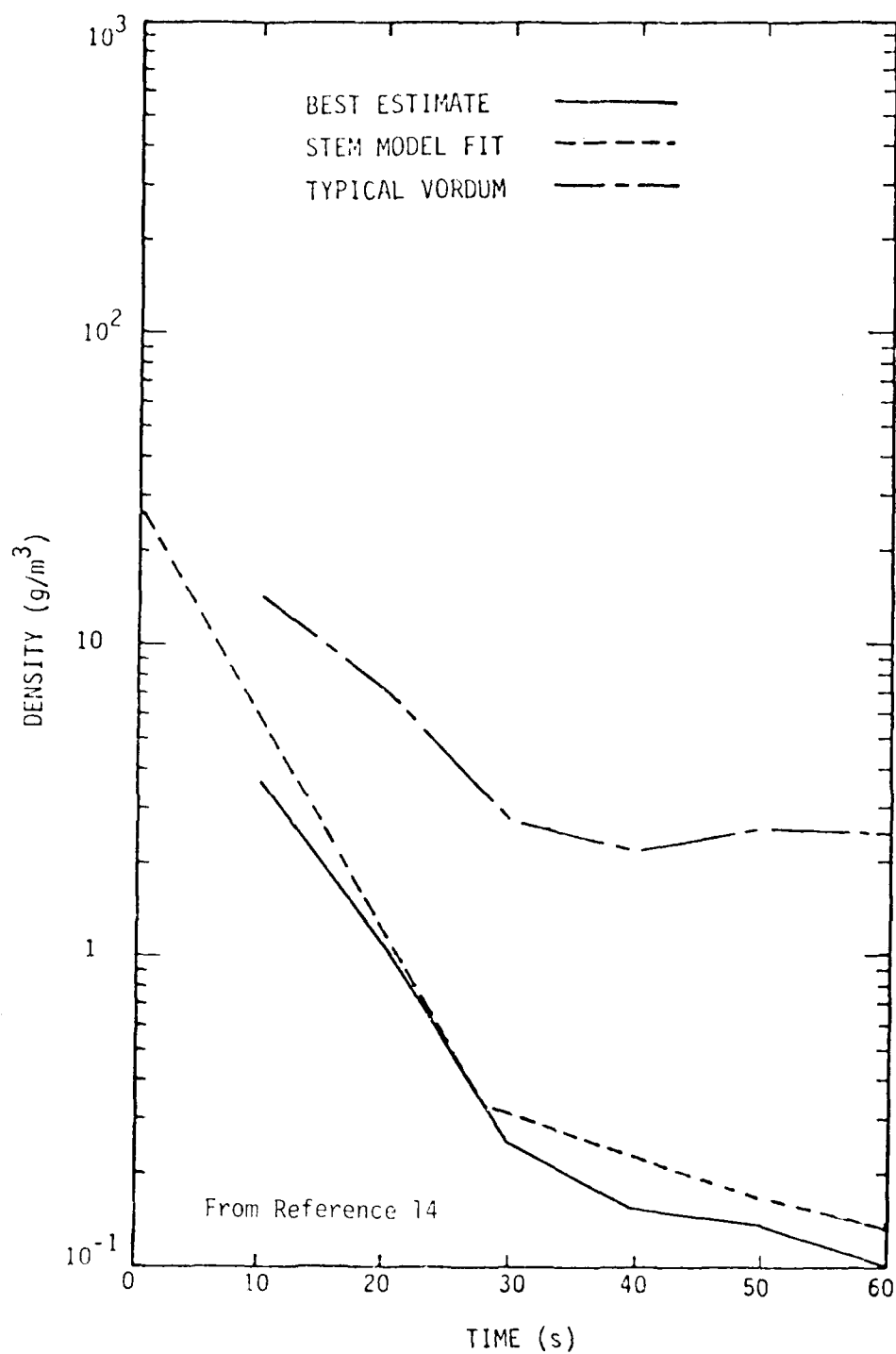
Figure 16. Early time stem densities for 0.05-MT burst at 120 $W^{1/3}$(KT)-feet altitude.

77
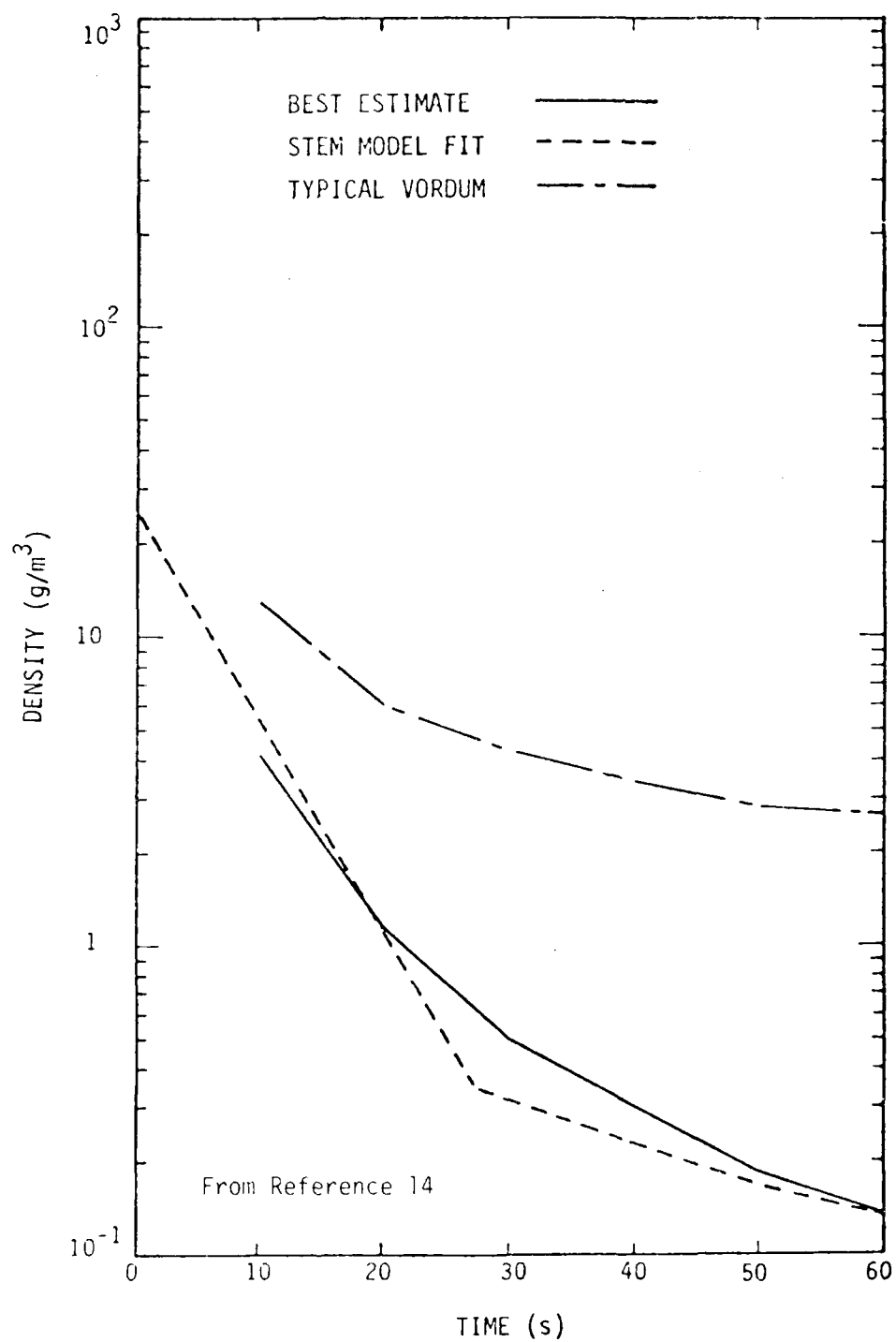
Figure 17. Early time stem densities for 0.05-MT burst at $150 \ w^{1/3}$ (KT)-feet altitude.

From Reference 14
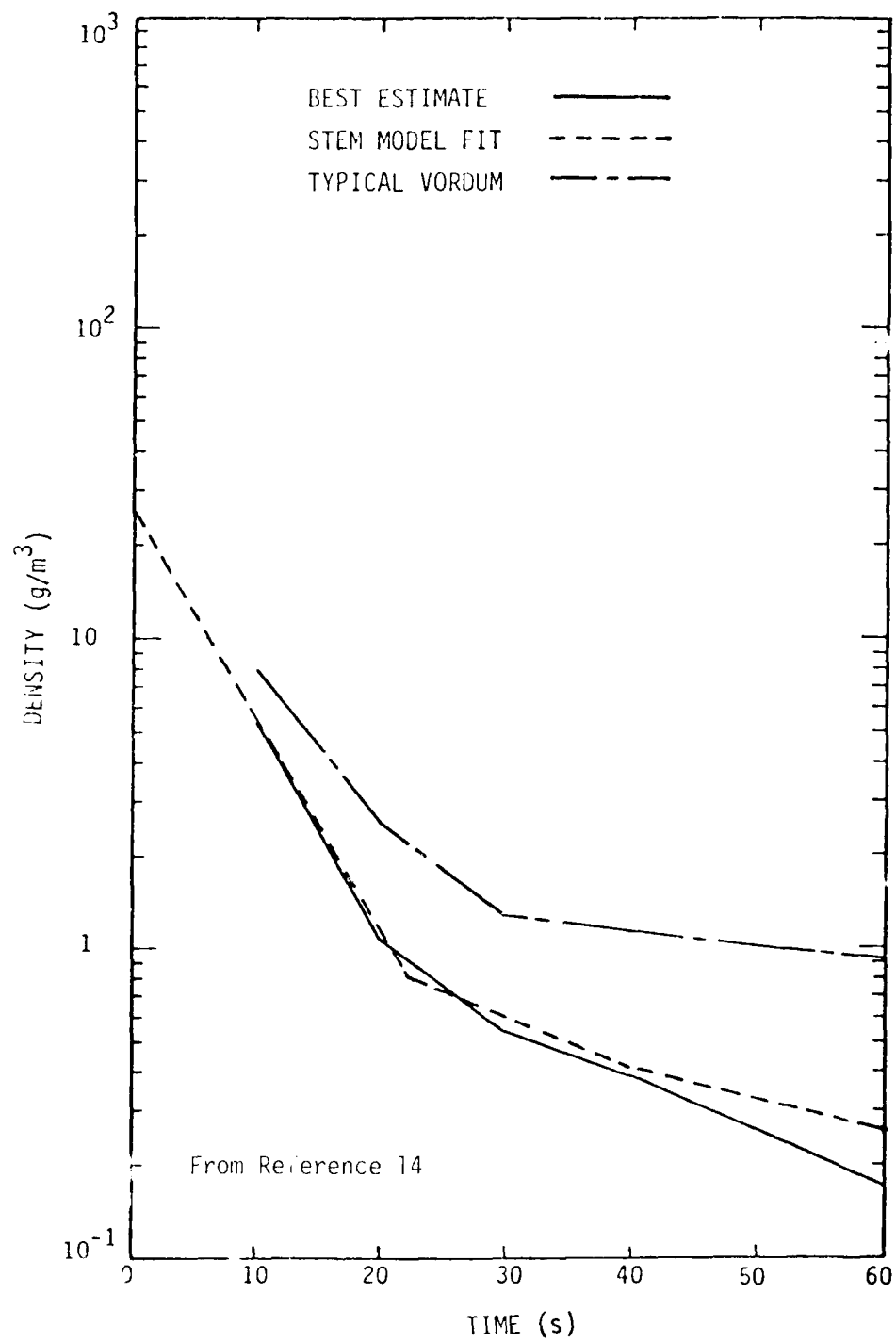
Figure 18.   Early time stem densities for 0.10-MT burst at 120 $W^{1/3}$(KT)-feet altitude.
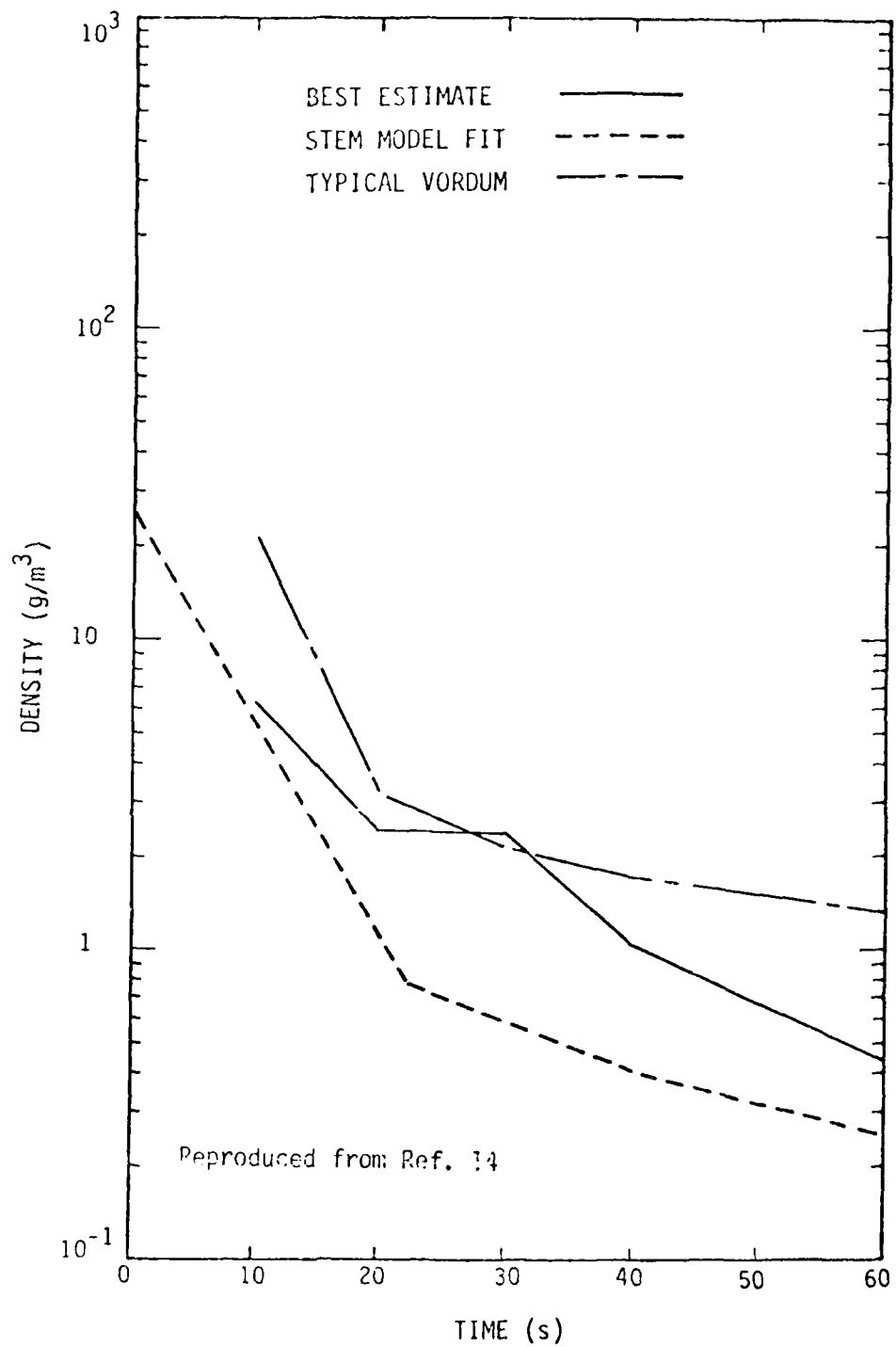
Figure 19. Early time stem densities for 0.10-MT burst at 200 $W^{1/3}$(KT)-feet altitude.
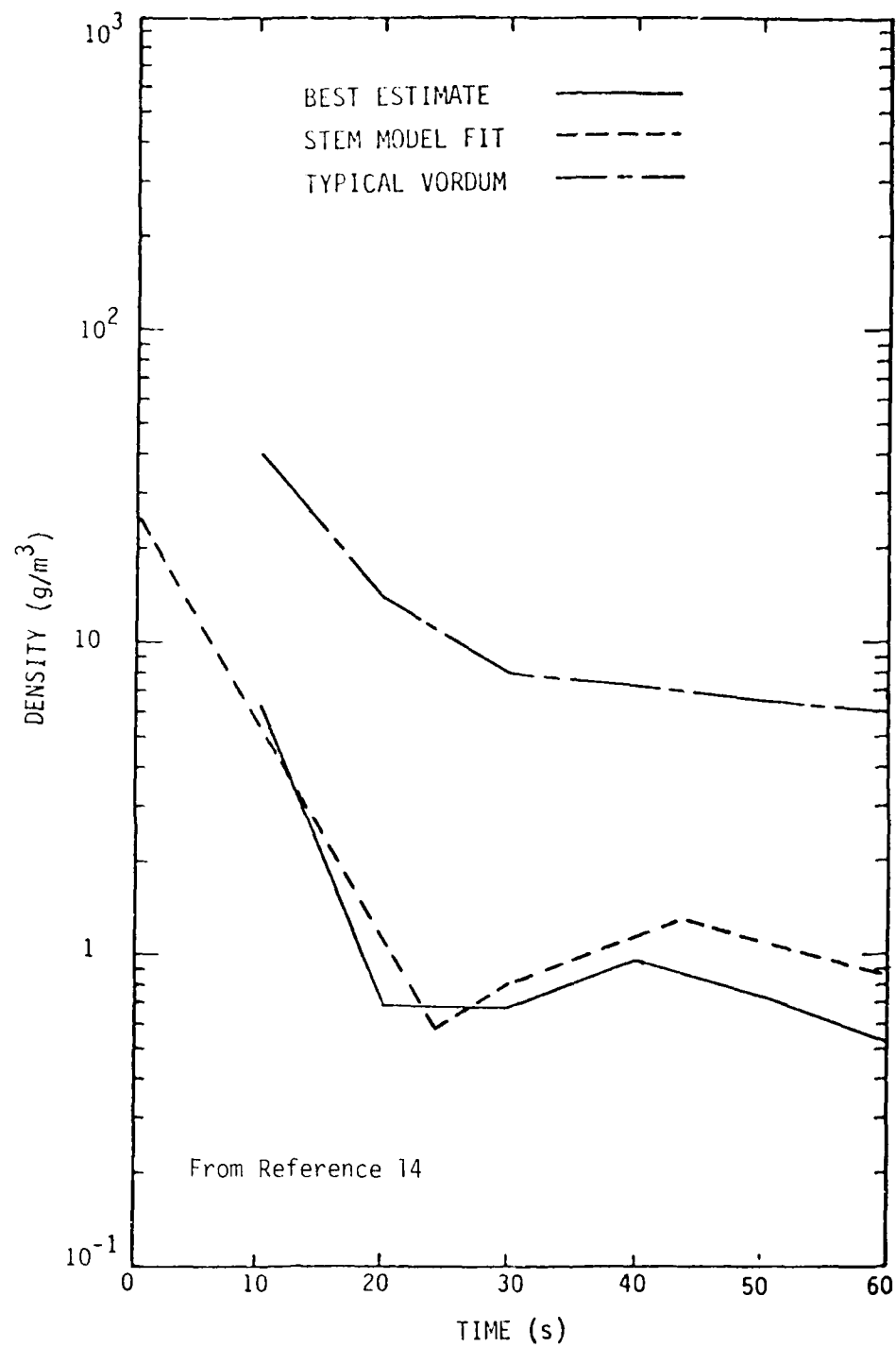
Figure 20. Early time stem densities for 0.50-MT burst at
50 $W^{1/3}$(KT)-feet altitude.

81
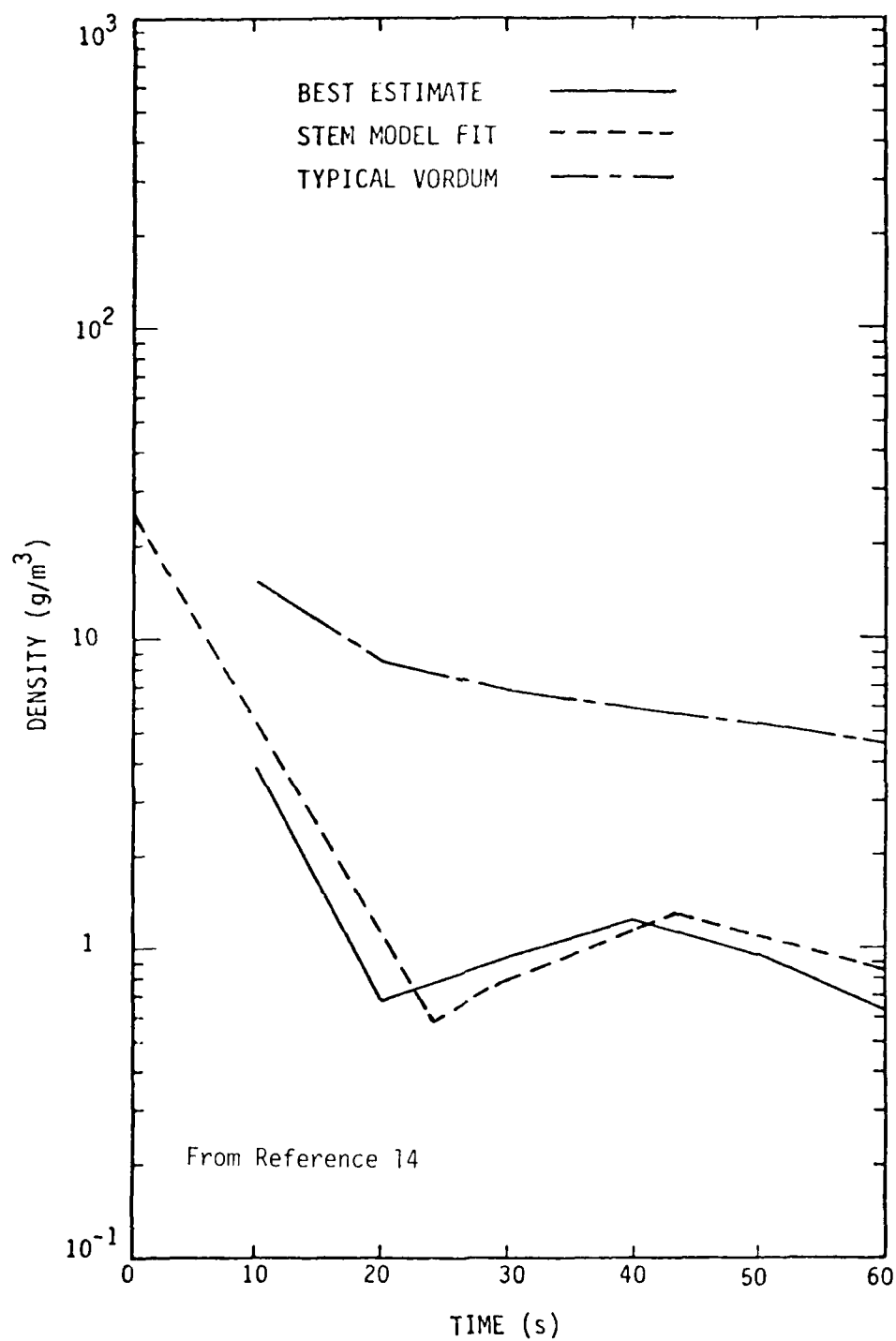
Figure 21.   Early time stem densities for 0.50-MT burst at 150 $W^{1/3}$(KT)-
feet altitude.
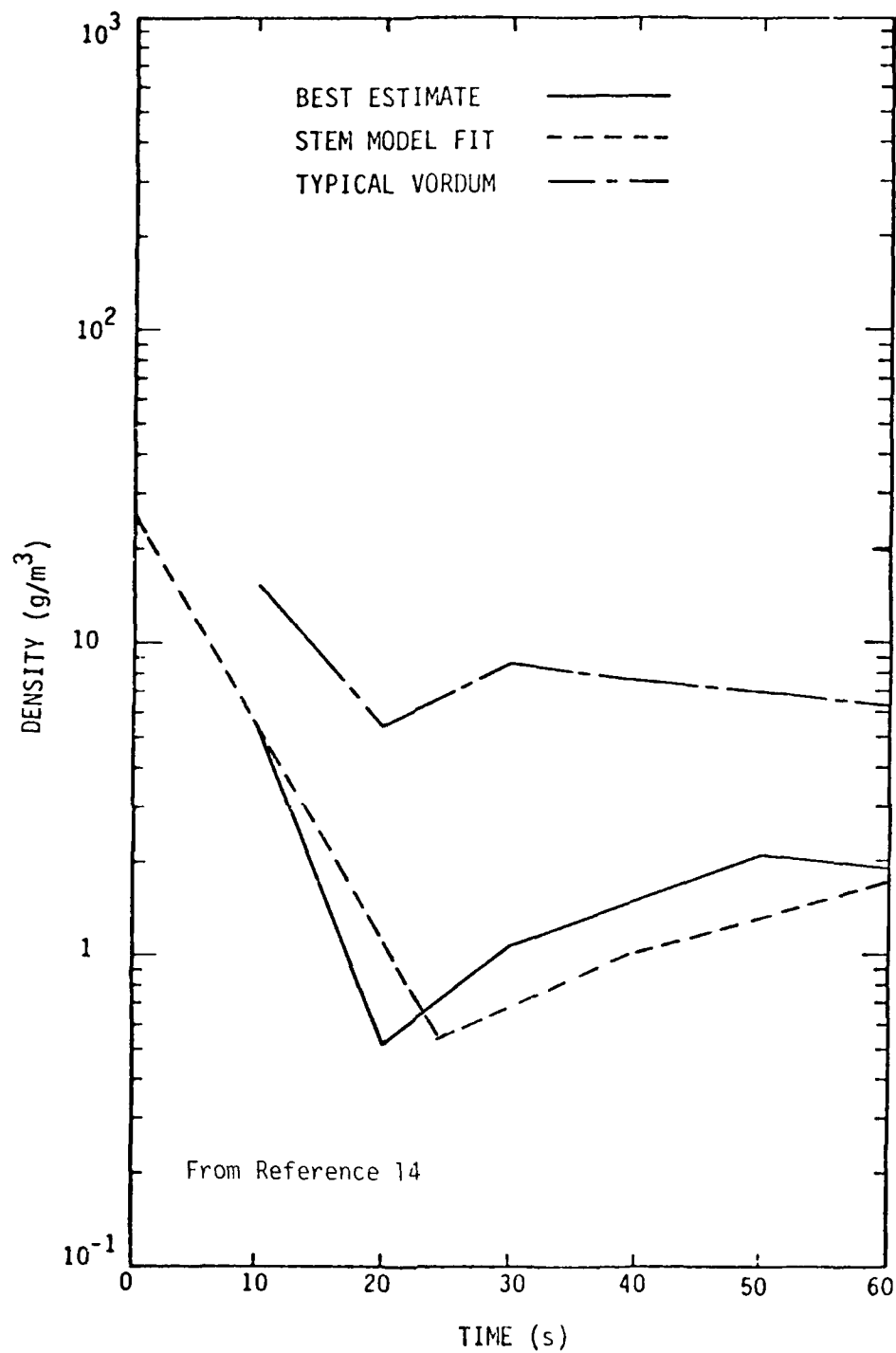
Figure 22.   Early time stem densities for 1.0-MT burst at 150 $W^{1/3}$(KT)-feet altitude.
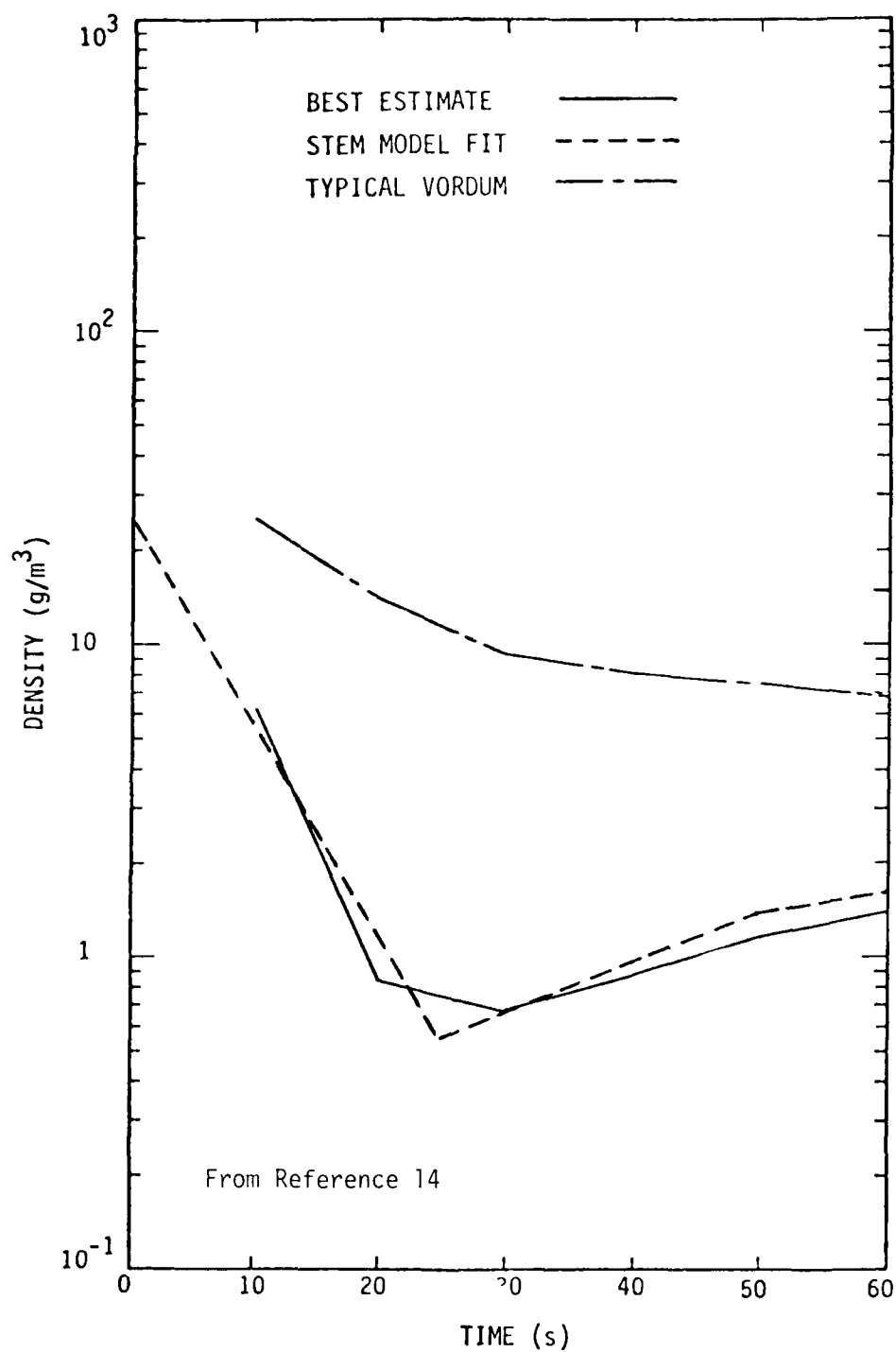
Figure 23. Early time stem densities for 2.0-MT burst at 50 $W^{1/3}$(KT)-feet altitude.
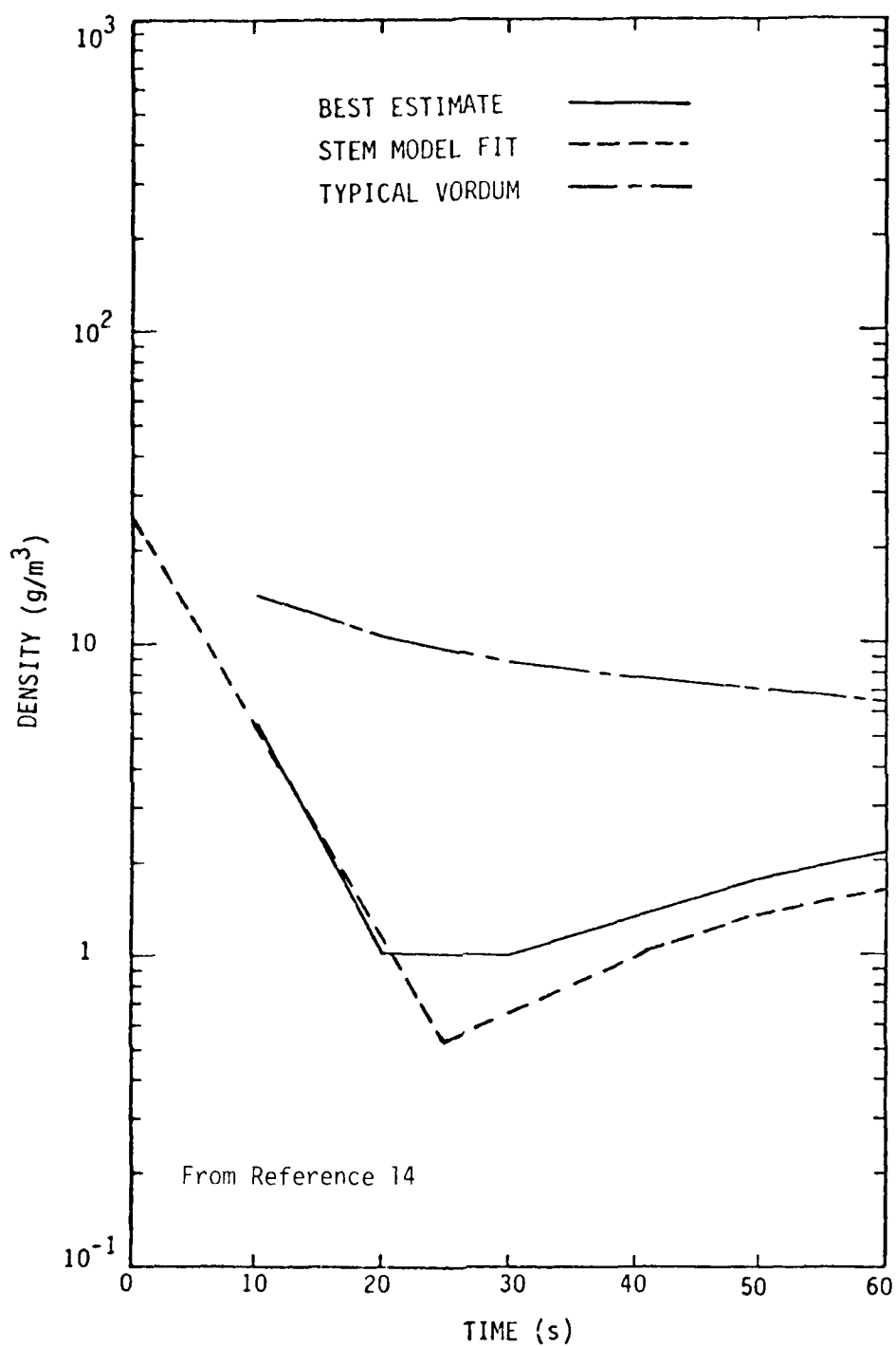
Figure 24. Early time stem densities for 2.0-MT burst at $150 \ W^{1/3}$(KT)-feet altitude.
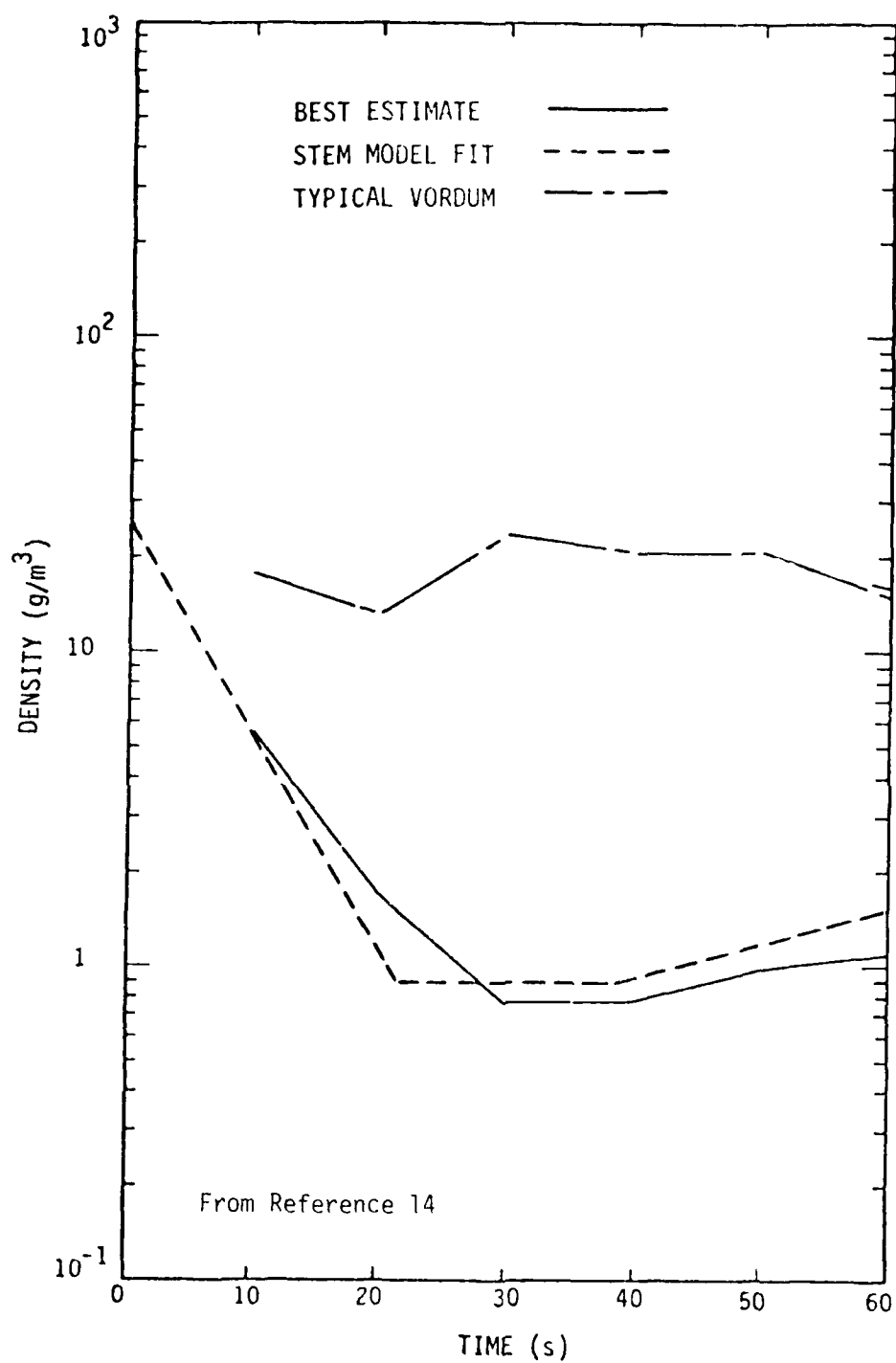
Figure 25. Early time stem densities for 5.0-MT burst at 50 $W^{1/3}$(KT)-feet altitude.
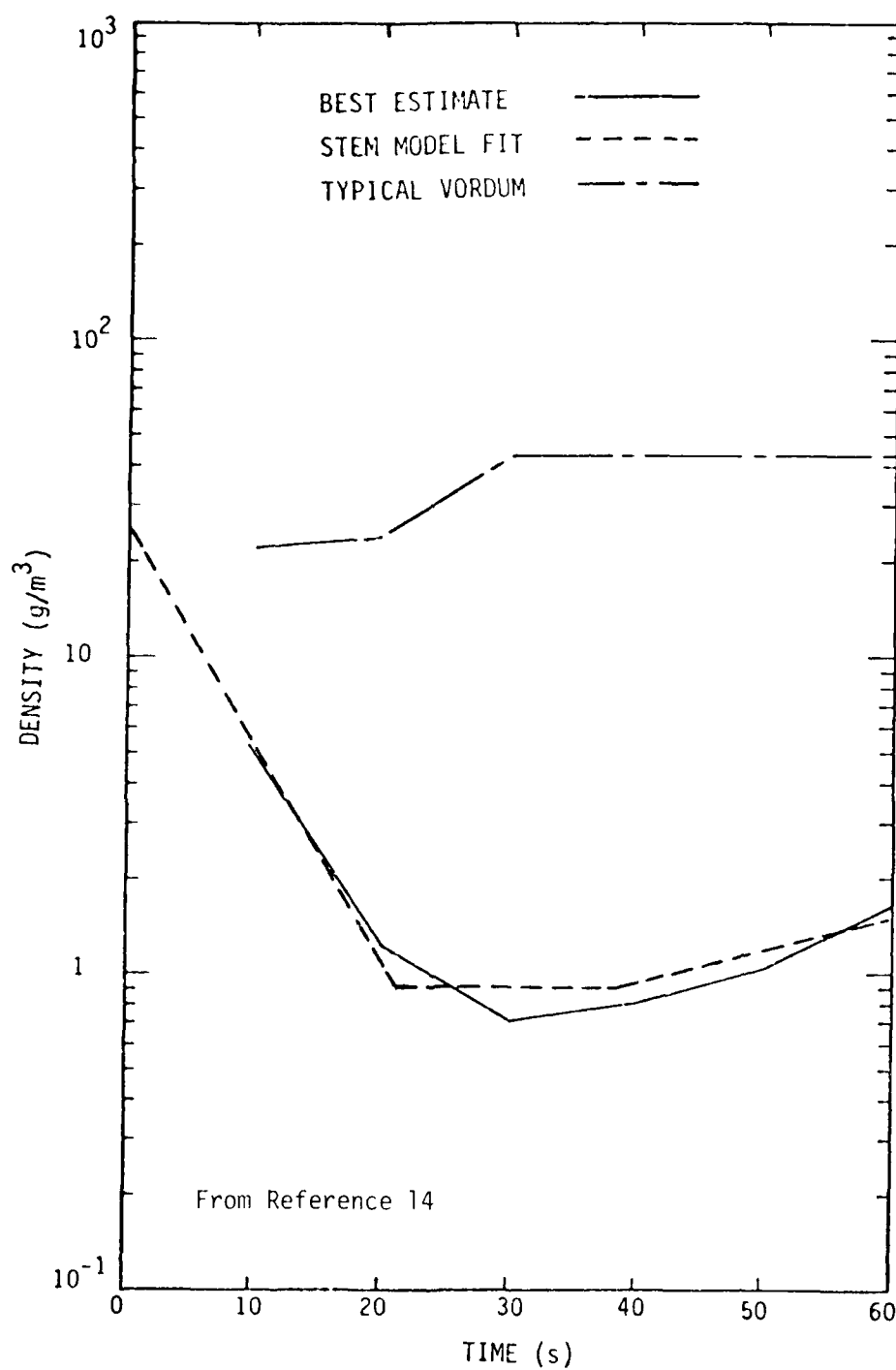
Figure 26. Early time stem densities for 5.0-MT burst at 150 $W^{1/3}$(KT)-feet altitude.
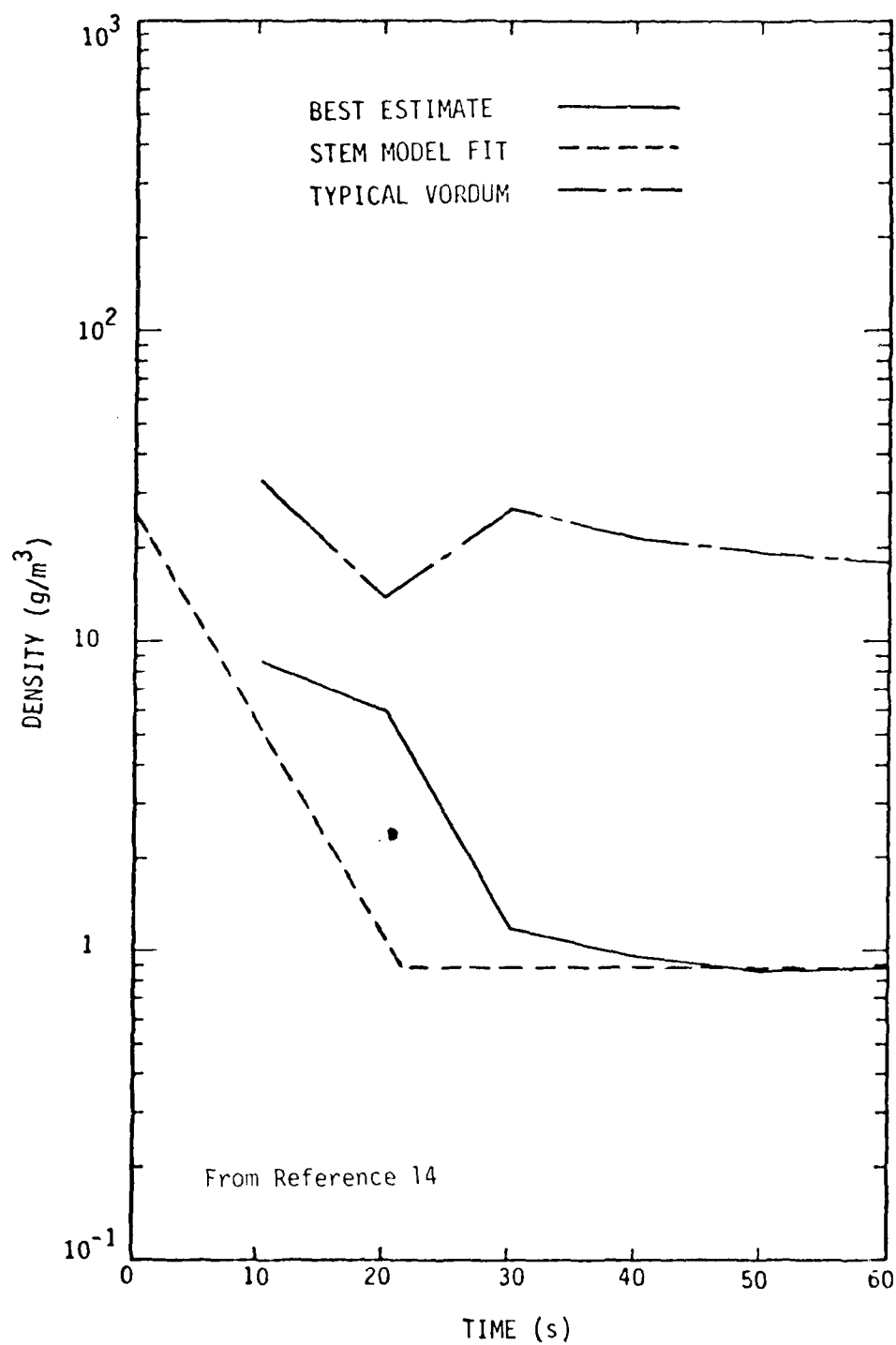
Figure 27. Early time stem densities for 20.0-MT burst at 50 $W^{1/3}$(KT)-feet altitude.
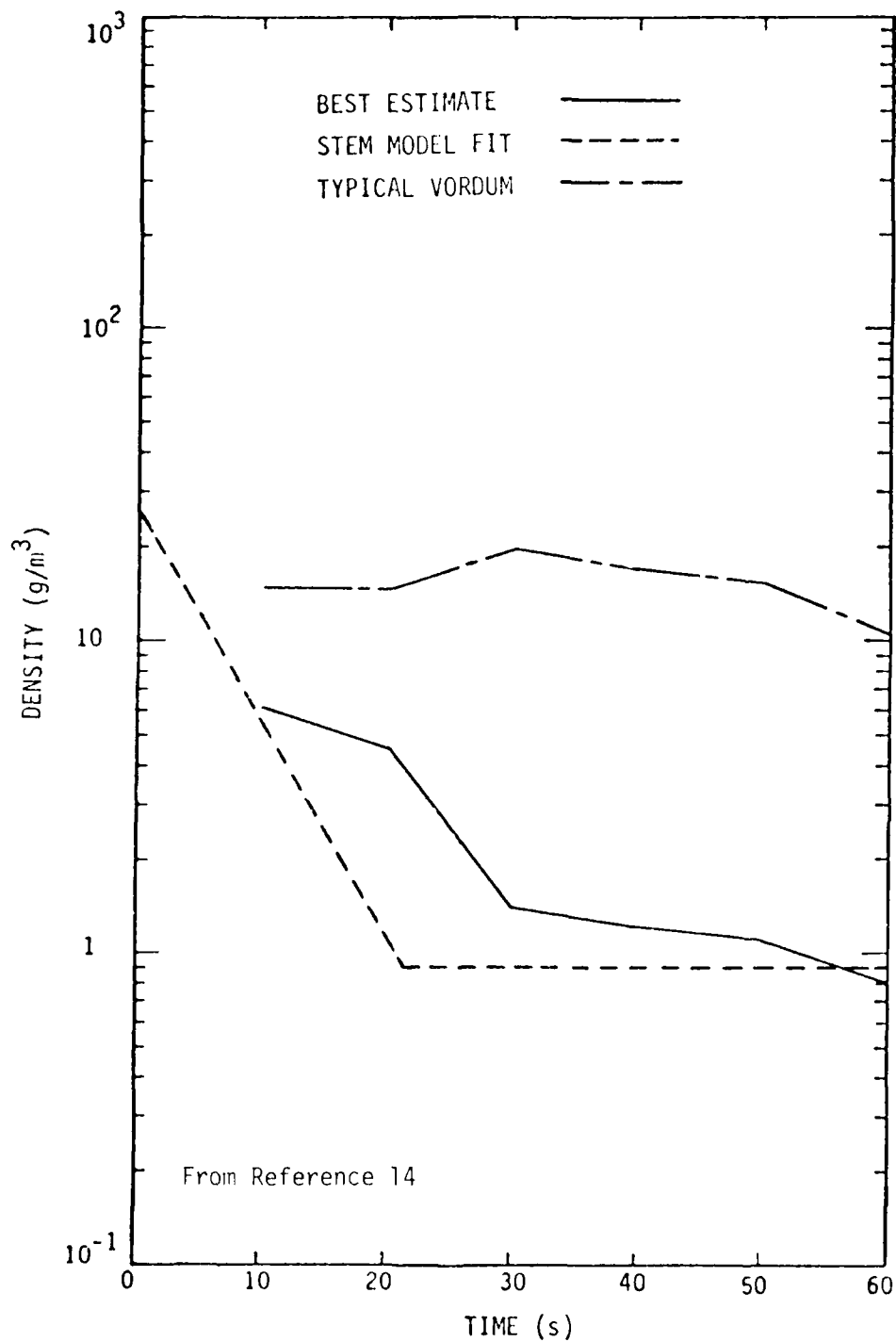
Figure 28.   Early time stem densities for 20.0-MT burst at 150 W$^{1/3}$(kT)-feet altitude.

$$
\rho_S(t) = MAX\left[2.5 \times 10^{-5} e^{-\frac{t}{6.54}} , \quad \rho_1\left(\frac{R_1}{R_S(t)}\right)^2\right] \text{ g cm}^{-3} \quad . \quad (121)
$$

The first term accounts for the early time rapid falloff while the second term accounts for the late time behavior. The late time functional dependence is equivalent to assuming that the total dust mass per unit length of the stem remains constant as the stem radius expands; ie, this is a dust mass conservation assumption.

Code calculations indicate that the air flow fields in the stem region are strong enough to loft soil particles of about 1 centimeter or so in diameter, if these particles are initially lofted into the flow fields from the soil surface (Reference 15). We extend the particle size groups chosen for the pedestal model up to 1 centimeter in diameter for the stem size groups; Table 13 shows the stem size groups.

Table 13. Stem dust size groups.

Group	Minimum Diameter of Particle in Group (cm)	Maximum Diameter of Particle in Group (cm)
1	0.001	0.004
2	0.004	0.01
3	0.01	0.04
4	0.04	0.1
5	0.1	0.4
6	0.4	1.0

In Reference 15 the trajectories of dust particles up to 1 centimeter diameter are studied by means of the STEM code. The calculated trajectories depend in a complex manner upon yield, height of burst, and initial assumed particle injection velocity. The calculations considered

times out to 60 seconds and burst heights between $20W^{1/3}$ (KT) and $200W^{1/3}$ (KT) feet. These theoretical data are not complete enough to allow an analytic model of stem particle motion to be developed; moreover we do not know the proper injection velocity to use. Hence, we will develop a very simplified stem particle motion model for use until more complete theoretical data are available.

We begin by calculating the maximum altitude, $(H_{SM})_i$, that each size group can be carried. We take the characteristic air velocity to be that of the average stem velocity, V_s, of Equation 115. We then substitute V_s into the terminal velocity Equation 104 and solve for ρ_a. This is the density a flow field of velocity V_s must have in order to just offset the gravity force of a particle of diameter d

$$(\rho_a)_i = \frac{30 \rho_p d_i g}{V_s^2} - \frac{54 \mu_a}{d_i V_s} \qquad g \cdot cm^{-3} \qquad (122)$$

We assume that the stem flow field carried a particle of diameter d_i upward to an altitude $(H_{SM})_i$ where the ambient density is $(\rho_a)_i$. The flow field can loft only those particles for which

$$(\rho_a)_i < \rho_o$$

where ρ_o is the ground level air density. For the characteristic particle diameter d_i of Equation 122, take the maximum diameter of the particles in group i.

The altitude of each size group cylinder is identical to the stem altitude, $H_s(t)$, until the altitude $(H_{SM})_i$ is reached. The group cylinder altitude stops, then falls as the stem flow fields weaken. We again use the minimum diameter of the group size to calculate the fall velocity (again to crudely compensate for the fact that the air is certainly not quiet). We use the terminal velocity equation to calculate two fall velocities V_{hi} and V_{oi}, where V_{hi} is the velocity at altitude $(H_{SM})_i$ and V_{oi} is the velocity at ground level. For small particles these

91

velocities will be about the same and we can use the average as a constant fall rate. For larger particles the fall rate will be larger at the high altitude and will diminish as the particle encounters denser air at the lower altitudes. Assume that the velocity is a simple linear function of altitude. Then

$$v(H) = v_o + \frac{H}{H_{SM}} (V_h - V_o) \tag{123}$$

and

$$v(H) = - \frac{dH}{dt} \quad . \tag{124}$$

Solving the first-order differential equation for H, we have

$$H(t) = H_{SM} - \frac{V_h H_{SM}}{V_h - V_o} \left[1 - e^{-\frac{V_h - V_o}{H_{SM}} (t - t_{fs})} \right] \qquad t > t_{fs} \tag{125}$$

where t_{fs} is the time the fall begins. For small particles

$$V_h \approx V_o \qquad \text{and we take}$$

$$H(t) = H_{SM} - V_o (t - t_{fs}) \qquad\qquad t > t_{fs} \quad . \tag{126}$$

Hence the time history of the altitude of each group cylinder is

$$H_i(t) = \begin{cases} H_s(t) & t \leq (t_{fs})_i \\ H(t) \ (\text{eqs } 125 \text{ and } 126) & t > (t_{fs})_i \end{cases} \tag{127}$$

and $(t_{fs})_i$ is the time at which $H_s(t_{fs}) = (H_{SM})_i$.

REFERENCES

1. Stanton, M.J., et al, *Nuclear-Induced Optical Phenomenology Program (1976-1977)*, General Electric-TEMPO, August 1977, unpublished.

2. Lentz, W.J., "Generating Bessel Functions in Mie Scattering Calculations Using Continued Fractions," *App. Opt.*, vol 15, no 3, pp 668-671, March 1976.

3. Layson, W.M., et al, *Nuclear Surface Burst Debris and System Vulnerability*, vol I, General Research Corporation, August 1969, unpublished.

4. Gicking, D., et al, *Technology Support for Environmental Defense*, Science Applications, Inc., September 1975, unpublished.

5. Wobschall, D., "A Theory of the Complex Dielectric Permittivity of Soil Containing Water: The Semidisperse Model," *IEEE Transactions on Geoscience Electronics*, *Volume GE-15*, Number 1, January 1977.

6. Hanai, T., "Dielectric Theory on the Interfacial Polarization for Two-Phase Mixtures," *Bull. Inst. Chem. Res., Kyoto Univ.*, *Vol 39*, pp 341-368, 1961. Also see *Electrical Properties of Emulsions*, Emulsion Science, P. Sherman, ed., New York, Academic Press, 1968.

7. Keller, G.V. and F. Frischknecht, *Electrical Methods in Geophysical Prospecting*, Pergamon Press, 1966.

8. *Proceedings of the DICE THROW Symposium, 21-23 June 1977, Volume 2*, DNA 4377P-2, DASIAC, General Electric Company— TEMPO, July 1977.

9. Burns, A.A., *DICE THROW UHF/SHF Transmission Experiment— Preliminary Results*, SRI International, January 1977, unpublished.

10. Burns, A.A., and R.E. Winkelman, *DICE THROW UHF/SHF Transmission Experiment - Dielectric Properties of Dust*, SRI International March 1977, unpublished.

11. Kirsch, J.W., et al, *Near-Surface Dust Cloud Phenomenology*, DNA 3962F (SSS-R-76-2827), Systems, Science, and Software, April 1976.

12. Powers, J.T., R.T. Liner, and J.E. Mansfield, *Precursor Sweep-up Dust Cloud Model and Thermal Model Development*, DNA 3876F (SAI-75-594-WA), Science Applications Inc, McLean, VA, December 1975.

13. Liner, R.T., et al, *Nuclear Precursor Phenomenology and Sweep-up Dust Cloud Model Development*, DNA 3781F (SAI-74-627-WA), Science Applications, Inc., McLean, VA, November 1975.

14. Seebaugh, W.R., *Estimates of Early-Time Stem Dust Densities for Scaled Heights of Burst from 20 to 200 Feet*, Science Applications, Inc., McLean, VA, October 1975 (Unpublished).

15. Hains, F.D., *Early-Time Nuclear Cloud Stem Fratricide Environments*, Science Applications, Inc., McLean, VA, August 1975, unpublished.

16. Kirsch, J.W., *Near-Surface Nuclear Dust Cloud Studies*, DNA 4332F (SSS-R-76-2828), Systems, Science, and Software, January 1977.

17. Hartenbaum, B., *Lofting of Particulates by a High Speed Wind*, DNA 2737, Applied Theory, Inc., September 1971.

18. Hare, Robert, General Electric-TEMPO, Personal Communication, January 1975.

APPENDIX A
MIE COMPUTER ROUTINES

In this appendix we give computer listings for two versions of the improved Mie routine. The first version, MISCAT, calculates the Mie efficiencies for extinction, scatter, and backscatter. The second version, MIE, calculates the Mie efficiencies for extinction and scatter and the unnormalized scattering pattern. From either version, the Mie efficiency for absorption can be found from

$$Q_{ABS} = Q_{EXT} - Q_{SCA} \tag{A-1}$$

The unnormalized scattering pattern calculated in MIE is

$$S_U(\theta) = \frac{S(\theta)}{\left(\frac{\lambda}{2\pi}\right)^2} \tag{A-2}$$

where $S(\theta)$ is the scattering pattern given by Equation 5 in Section 2. For the MIE version, the backscatter efficiency, if desired, can be calculated from

$$Q_{BKS} = \frac{4S_U(\pi)}{\alpha^2} \tag{A-3}$$

where α is the dimensionless size parameter defined in Section 2.

The complex function routine ANF evaluates the complex function $A_n(Y)$ (Equation 19 of Section 2) and is used by both the MIE and MISCAT routines. Computer listings for ANF are also included here.

95

```
      SUBROUTINE MISCAT( XN, DR, DI, QBS, QEXT, QSCA )
C
C     THIS IS A MODIFIED WOE ROUTINE - MODEL EQUATIONS DOCUMENTED IN
C                                      REPORT GE77TMP-22
C
C     THIS ROUTINE USES MIE  THEORY TO CALCULATE THE EFFICIENCIES FOR
C     SCATTER(TOTAL), BACKSCATTER AND EXTINCTION FOR A SINGLE UNIFORM
C     SPHERICAL PARTICLE
C
C         INPUTS
C     XN       = NORMALIZED SIZE PARAMETER, WHICH EQUALS TWO PI TIMES
C                THE RADIUS OF THE SPHERE DIVIDED BY THE WAVELENGTH OF THE
C                INCIDENT RADIATION
C     DR       = REAL PART OF THE COMPLEX INDEX OF REFRACTION OF THE
C                SPHERE
C     DI       = IMAGINARY PART OF THE COMPLEX INDEX OF REFRACTION OF THE
C                SPHERE
C     NOTE THAT THE COMPLEX INDEX OF REFRACTION IS ASSUMED TO BE
C     N = DR - I*DI
C
C         OUTPUTS
C     QSCA     = SCATTER(TOTAL) EFFICIENCY, WHICH EQUALS THE (TOTAL)
C                SCATTERING CROSS SECTION DIVIDED BY THE CROSS SECTIONAL
C                AREA OF THE SPHERE( SIGMA/(PI*RADIUS**2)
C     QBS      = BACKSCATTER EFFICIENCY, WHICH EQUALS THE SCATTERING CROSS
C                SECTION( IN THE BACKWARDS DIRECTION) DIVIDED BY THE CROSS
C                SECTIONAL AREA OF THE SPHERE( SIGMA/(PI*RADIUS**2)
C     QEXT     = EXTINCTION EFFICIENCY, WHICH EQUALS THE TOTAL (SCATTERING
C                + ABSORPTION ) CROSS SECTION OF THE SPHERE DIVIDED BY THE
C                CROSS SECTIONAL AREA OF THE SPHERE
C
C
      DIMENSION ANR(200)
      COMPLEX D,Z,EM1,EM2,EN,ANF,ANR,ANZ,AN,BN,QBSC
      D = CMPLX( DR, -DI )
      X=AMIN1( 100., XN )
      Z = X * D
      EM1 = CMPLX( SIN( X ), COS( X ) )
      EM2 = CMPLX( COS( X ), -SIN( X ) )
      QBSC = ( 0., 0. )
      QEXT = 0.
      QSCA=0.0
      NX = 1.5 * X
      NX=MAX0( 2, NX )
      ANR(NX) = ANF( NX, Z )
      NXM1 = NX - 1
      DO 10 I = 1, NXM1
      N = NX + 1 - I
      CN = FLOAT( N )
      ANR(N-1) = CN / Z - (1.,0.) / ( CN / Z + ANR(N) )
   10 CONTINUE
      X2 = X ** 2
```

```
      ONE = -1.
      DO 30 N = 1, 200
      ONE = -ONE
      FN = N
      C1 = 2. * FN - 1.
      FN = C1 * EM1 / X - EM2
      IF ( N .LE. NX ) ANZ = ANR(N)
      IF ( N .GT. NX ) ANZ = ANF( N, Z )

      CFNOX = FN / X
      C1 = REAL( EN )
      C2 = REAL( EM1 )
      AN = ( ( ANZ / D + CFNOX ) * C1 - C2 ) /
     1      ( ( ANZ / D + CFNOX ) * EN - EM1 )
      BN = ( ( D * ANZ + CFNOX ) * C1 - C2 ) /
     1      ( ( D * ANZ + CFNOX ) * EN - EM1 )
      XFACT = 2. * FN + 1.
      XFACB = ONE * ( FN + 0.5 )
      QEXT = QEXT + XFACT * REAL( AN + BN )
      QSCA=QSCA+XFACT* (CABS(AN)**2+CABS(BN)**2)
      QBSC = QBSC + XFACB * ( AN - BN )
      EM2 = EM1
      EM1 = FN
      IF( N .EQ. 1 .OR. FN .LT. 1.2 * X ) GO TO 20
      IF ( ABS( 1. - AMAX1( QEXT, QEXTST ) / AMIN1( QEXT, QEXTST ) )
     1      .LE. 1.E-3 ) GO TO 40
   20 QEXTST = QEXT
   30 CONTINUE
   40 QEXT = 2. * QEXT / X2
      QSCA=2.0*QSCA/X2
      QBS = 4. * ( CABS( QBSC ) ** 2 ) / X2
      RETURN
      END
```

```
      SUBROUTINE MIE( X, DR, DI, QSCA, QEXT, S )
C
C     THIS IS A WDE ROUTINE - MODEL EQUATIONS ARE DOCUMENTED IN REPORT
C                          GF77TMP-2?
C
C     THIS ROUTINE USES MIE  THEORY TO CALCULATE THE EFFICIENCIES FOR
C     SCATTERING AND ABSORPTION AND THE SCATTERING PATTERN FOR A SINGLE
C     UNIFORM SPHERICAL PARTICLE
C
C        INPUTS
C     X        = NORMALIZED SIZE PARAMETER, WHICH EQUALS TWO PI TIMES
C                THE RADIUS OF THE SPHERE DIVIDED BY THE WAVELENGTH OF THE
C                INCIDENT RADIATION
C     DR       = REAL PART OF THE COMPLEX INDEX OF REFRACTION OF THE
C                SPHERE
C     DI       = IMAGINARY PART OF THE COMPLEX INDEX OF REFRACTION OF THE
C                SPHERE
C     NOTE THAT THE COMPLEX INDEX OF REFRACTION IS ASSUMED TO BE
C     N = DR - I*DI
C
C        OUTPUTS
C     QSCA     = SCATTERING EFFICIENCY, WHICH EQUALS THE SCATTERING CROSS
C                SECTION OF THE SPHERE DIVIDED BY THE CROSS SECTIONAL AREA
C                OF THE SPHERE ( SIGMA/(PI*RADIUS**2)
C     QEXT     = EXTINCTION EFFICIENCY, WHICH EQUALS THE TOTAL ( SCATTERING
C                + ABSORPTION ) CROSS SECTION OF THE SPHERE DIVIDED BY THE
C                CROSS SECTIONAL AREA OF THE SPHERE
C     S        = SCATTERING PATTERN OF THE RADIATION SCATTERED BY THE
C                SPHERE, ASSUMING INCIDENT UNPOLARIZED RADIATION. S(J) =
C                SCATTERING FUNCTION FOR THE SCATTERING ANGLE WHOSE COSINE
C                IS 0.1*(J-11). S IS UN-NORMALIZED, THAT IS, THE INTEGRAL
C                OF S OVER 4 PI STERADIANS EQUALS PI*QSCA*X**2
C
C
      DIMENSION S(21), XMU(21), S1(21), S2(21), PP1(21), PP2(21),
     1     PT1(21), PT2(21), PT(21), PP(21)
      DIMENSION ANR(200)
      COMPLEX D, Z, EM1, EM2, FN, S1, S2, ANR
      COMPLEX ANR, CN, ANZ, AN, BN
      COMPLEX CA, C1, C2, CENOX, CXFACT
      DATA XMU / -1., -.9, -.8, -.7, -.6, -.5, -.4, -.3, -.2, -.1, 0.,
     1     .1, .2, .3, .4, .5, .6, .7, .8, .9, 1. /
C
C
C     SET VALUES OF COMPLEX INDEX OF REFRACTION, SIZE PARAMETER, AND
C     MIE VARIABLE
      D = CMPLX( DR, -DI )
      CX = X
      Z = CX * D
C
C     SET INITIAL VALUES OF RICCATI-BESSEL FUNCTION
      EM1 = CMPLX( SIN( X ), COS( X ) )
```

98

```
      EM2 = CMPLX( COS( X ), -SIN( X ) )
C
C     ZERO OUT EFFICIENCY VARIABLES AND SCATTERING PATTERN VARIABLES
      DO 5 I = 1, 21
      S1(I) = 0.
      S2(I) = 0.
      PP1(I) = 0.
      PT1(I) = 0.
      PP2(I) = 0.
      PT2(I) = 0.
    5 CONTINUE
      QSCA = 0.
      QEXT = 0.
C
C     SET UP ARRAY OF ANR VALUES - USE LENTZ BACKWARDS RECURSION
C     TECHNIQUE
      NX = 1.5 * X
      NX = MAX0( 2, MIN0( NX, 200 ) )
      ANR(NX) = ANF( NX, Z )
      NXM1 = NX - 1
      DO 10 I = 1, NXM1
      N = NX + 1 - I
      CN = FLOAT( N )
      ANR(N-1) = CN / Z - (1.,0.) / ( CN / Z + ANR(N) )
   10 CONTINUE
C
C
C     CALCULATE THE EFFICIENCIES AND SCATTERING PATTERN USING THE MIE
C     INFINITE SERIES EXPANSION FORMULAS
      DO 1 N = 1, 200
      FN = N
      C1 = 2. * FN - 1.
      EN = C1 * EM1 / CX - EM2
      IF ( N .LE. NX ) ANZ = ANR(N)
      IF ( N .GT. NX ) ANZ = ANF( N, Z )

      CFNOX = FN / X
      C1 = REAL( EN )
      C2 = REAL( EM1 )
      AN = ( ( ANZ / D + CFNOX ) * C1 - C2 ) /
     1      ( ( ANZ / D + CFNOX ) * EN - EM1 )
      BN = ( ( D * ANZ + CFNOX ) * C1 - C2 ) /
     1      ( ( D * ANZ + CFNOX ) * EN - EM1 )
      XFACT = ( 4. * FN + 2. ) / X **2
      QSCA = QSCA + XFACT * ( CABS( AN ) **2 + CABS( BN ) **2 )
      QEXT = QEXT + XFACT * REAL( AN + BN )
      EM2 = EM1
      EM1 = EN
      DO 4 I = 1, 21
      IF ( N .GT. 2 ) GO TO 6
      IF ( N .EQ. 2 ) GO TO 7
      PP(I) = 1.
```

99

```
      PT(I) = XMU(I)
      GO TO 8
    7 PP(I) = 3. * XMU(I)
      PT(I) = 6. * XMU(I) **2 - 3.
      GO TO 8
    6 PP(I) = ( ( 2. * FN - 1. ) * XMU(I) * PP1(I) - FN * PP2(I) ) /
     1        ( FN - 1. )
      PT(I) = XMU(I) * ( PP(I) - PP2(I) ) - ( 2. * FN - 1. ) *
     1        ( 1. - XMU(I) **2 ) * PP1(I) + PT2(I)
    8 CXFACT = ( 2. * FN + 1. ) / ( FN **2 + FN )
      C1 = PP(I)
      C2 = PT(I)
      S1(I) = S1(I) + CXFACT * ( AN * C1 + BN * C2 )
      S2(I) = S2(I) + CXFACT * ( BN * C1 + AN * C2 )
      PP2(I) = PP1(I)
      PT2(I) = PT1(I)
      PP1(I) = PP(I)
      PT1(I) = PT(I)
    4 CONTINUE
      IF( N .EQ. 1 .OR. FN .LT. 1.2 * X ) GO TO 2
C
C     CHECK IF THE INIFINITE SERIES HAS CONVERGED
      IF ( ABS( 1. - AMAX1( QEXT, QEXTST ) / AMIN1( QEXT, QEXTST ) )
     1        .LE. 5.E-3 ) GO TO 3
C
C     CONVERGENCE HAS NOT BEEN REACHED, COMPUTE NEXT TERM IN SERIES
    2 QSCAST = QSCA
      QEXTST = QEXT
    1 CONTINUE
C
C     SERIES HAS CONVERGED, COMPUTE THE UNPOLARIZED SCATTERING PATTERN
    3 DO 9 I = 1, 21
      S(I) = 0.5 * ( CABS( S1(I) ) **2 + CABS( S2(I) ) **2 )
    9 CONTINUE
C
      RETURN
      END
```

```
            COMPLEX FUNCTION ANF( INDEX, Z )
C
C       THIS IS A WOE ROUTINE - DOCUMENTED IN REPORT GE77TMP-22
C       THIS ROUTINE IS CALLED BY MISCAT
C
C       THIS FUNCTION EVALUATES THE  COMPLEX QUANTITY A(N,Z) WHICH IS USED
C       IN THE MIE FORMULAS, WHERE
C       A(N,Z) = -N/Z + J(N-1/2,Z)/J(N+1/2,Z)
C       Z       = M*ALPHA
C       M       = M(REAL)-I*M(IMAGINARY) = COMPLEX INDEX OF REFRACTION
C       ALPHA   = 2*PI*R/WAVELENGTH = NORMALIZED SIZE PARAMETER
C       R       = RADIUS OF SPHERE
C       N       = ORDER OF THE FUNCTION
C       J       = BESSEL FUNCTION OF COMPLEX ARGUMENT AND HALF-INTEGER
C                 ORDER
C
C       THE METHOD OF EVALUATION USES THE CONTINUED FRACTION ALGORITHM OF
C       WILLIAM J LENTZ - GENERATING BESSEL FUNCTIONS IN MIE SCATTERING
C                         CALCULATIONS USING CONTINUED FRACTIONS
C                         APPLIED OPTICS, VOL. 15, NO. 3, MARCH 1976
C
C
C           INPUTS
C       INDEX = ORDER OF A(N,Z), THAT IS, INDEX = N
C       Z       = COMPLEX ARGUMENT
C
C           OUTPUT
C       ANF     = A(N,Z)
C
C
        COMPLEX Z, N, D, T, PN, PD, T1, T2 , E
C
C       DEFINE ARITHMETIC STATEMENT
        C( X ) = 2. * S * ( FN - 0.5 + XI )
C
C       SET VALUE OF FIRST PARTIAL FRACTION TERM FOR NUMERATOR (PN)
        FN = INDEX
        S = -1.
        CP = 2. * FN + 1.
        PN=CP/Z
C
C       SET VALUE OF FIRST PARTIAL CONVERGENT FOR NUMERATOR (N)
        N=PN
C
C       CALCULATE SECOND PARTIAL FRACTION AND CONVERGENT FOR NUMERATOR
        CP = -2. * FN - 3.
        T=CP/Z
        PN=T+(1.,0.)/PN
        N=N*PN
C
C       SET VALUE OF FIRST PARTIAL FRACTION (PD) AND CONVERGENT (D) FOR
C       DENOMINATOR
```

```
      PD=T
      D=PD
C
C
C     CALCULATE THE HIGHER ORDERS OF THE PARTIAL FRACTIONS AND
C     CONVERGENTS
      XI=2.
      DO 30 J = 1 , 100
      XI=XI+1.
      S = -S
      T = C( X ) / Z
      PN=T+(1.,0.)/PN
      PD=T+(1.,0.)/PD
C
C
C     IN THE RARE INSTANCE THAT THE NUMERATOR PARTIAL FRACTION TERM IS
C     NEAR ZERO, USE THE LENTZ ALGORITHM IMPROVEMENT METHOD TO INSURE
C     ACCURACY
      IF ( CABS( PN ) .GT. 1.E-4 ) GO TO 20
      S = -S
      XI = XI + 1.
      T1 = C( X ) / Z
      E = T1 * PN + (1.,0.)
      N = N * E
      S = -S
      XI = XI + 1.
      T2 = C( X ) / Z
      PN = T2 + PN / E
C
C     IF THE DENOMINATOR PARTIAL FRACTION TERM IS NEAR ZERO, USE THE
C     ALGORITHM IMPROVEMENT METHOD
      IF ( CABS( PD ) .GT. 1.E-4 ) GO TO 10
      E = T1 * PD + (1.,0.)
      D = D * E
      PD = T2 + PD / E
      GO TO 20
C
   10 D = D * PD
      PD=T1+(1.,0.)/PD
      D = D * PD
      PD=T2+(1.,0.)/PD
C
C
   20 N = N * PN
      D = D * PD
C
C     CHECK IF CONVERGENCE HAS BEEN REACHED
      IF ( ABS( CABS( PN ) / CABS( PD ) - 1. ) .LE. 1.E-6 ) GO TO 40
   30 CONTINUE
C
C
C     CONVERGENCE HAS BEEN REACHED, SET VALUE OF ANF
C
   40 ANF = -FN / Z + N / D
C
      RETURN
      END
```

102

APPENDIX B

IMPLEMENTATION OF THE GENERALIZED POWER LAW SIZE DISTRIBUTION

The power law size distribution for nuclear produced dust particles is given by Equation 26, where p is the power law exponent. In the present WEPH model, p is taken as 4.0, a value representative of dust particles generated from loose unconsolidated soils. The present fixed p model is easily generalized to an arbitrary p. We first present those model equations which are changed due to an arbitrary exponent; then we give a computer listing of the revised computer routine PGROUP. PGROUP calculates the extinction and backscatter cross sections per particle for a given size interval of dust particles.

The generalized model equations are:

Number distribution

$$f(a) = K_s \, a^{-p} \tag{B-1}$$

Total number of particles

$$N_{PT} = \frac{K_s}{p-1} \left[a_s^{1-p} - a_\ell^{1-p} \right] \tag{B-2}$$

Fraction of particles in size group i

$$F_{Ni} = \frac{N_{p_i}}{N_{PT}} = \frac{a_i^{1-p} - a_{i+1}^{1-p}}{a_s^{1-p} - a_\ell^{1-p}} \tag{B-3}$$

Total mass

$$M_T = \frac{\pi \rho_b K_s}{6} \begin{cases} \dfrac{1}{4-p} \left[a_\ell^{4-p} - a_s^{4-p} \right] & p \neq 4 \\[2ex] \ell n \, \dfrac{a_\ell}{a_s} & p = 4 \end{cases} \tag{B-4}$$

Normalization constant

$$K_s = \frac{5.44 \times 10^{12}\, F_M W}{\pi \rho_b} \begin{cases} \dfrac{4-p}{a^{4-p} - a_s^{4-p}} & p \neq 4 \\[4mm] \dfrac{1}{\ln \dfrac{a_\ell}{a_s}} & p = 4 \end{cases} \tag{B-5}$$

Backscatter cross section

$$\overline{\sigma}_{bi} = \frac{10^{-4}\, \pi (p-1)}{4(a_i^{1-p} - a_{i+1}^{1-p})} \sum_{j=1}^{J} \sigma_{bj} \tag{B-6}$$

$$\sigma_{bj} = K_b(a_j) \begin{cases} \dfrac{\exp\left[(x_{bj}+3-p)\ln \dfrac{a_{j+1}}{a_j}\right]-1}{a_j^{p-3}(x_{bj}+3-p)} & x_{bj} \neq p-3 \\[6mm] \dfrac{1}{a_j^{x_{bj}}} \ln \dfrac{a_{j+1}}{a_j} & x_{bj} = p-3 \end{cases} \tag{B-7}$$

Extinction cross section

$$\overline{\sigma}_{ei} = \frac{10^{-4}\pi (p-1)}{4(a_i^{1-p} - a_{i+1}^{1-p})} \sum_{j=1}^{J} \sigma_{ej} \tag{B-8}$$

$$\sigma_{ej} = K_e(a_j) \begin{cases} \dfrac{\exp\left[(x_{ej}+3-p)\ln \dfrac{a_{j+1}}{a_j}\right]-1}{a_j^{-3}(x_{ej}+3-p)} & x_{ej} \neq p-3 \\[6mm] \dfrac{1}{a_j^{x_{ej}}} \ln \dfrac{a_{j+1}}{a_j} & x_{ej} = p-3 \end{cases} \tag{B-9}$$

The computer listing of subroutine PGROUP follows.

```
      SUBROUTINE PGROUP( JGROUP, FREQ, DIECR, DIECI, P )
C
C     RANC ROUTINE MODIFIED FOR USE IN WEPH
C     THIS ROUTINE COMPUTES THE AVERAGE BACKSCATTER AND EXTINCTION
C     CROSS SECTIONS FOR A SPECIFIED DUST PARTICLE GROUP
C
C         INPUTS FROM CALL STATEMENT
C     FREQ   = FREQUENCY, MHZ
C     JGROUP = NUMBER OF DUST PARTICLE GROUP
C     DIECR  = REAL PART OF COMPLEX INDEX OF REFRACTION
C     DIECI  = IMAGINARY PART OF COMPLEX INDEX OF REFRACTION ( NOTE THAT
C              THE INDEX OF REFRACTION IS M = DIECR - I*DIECI SO THAT
C              BOTH DIECR AND DIECI ARE POSITIVE )
C     P      = EXPONENT OF GENERALIZED POWER LAW PROBABILITY
C              DISTRIBUTION
C
C         OUTPUTS TO TEST COMMON AREA
C     SIGE   = AVERAGE EXTINCTION CROSS SECTION, M2
C     SIGB   = AVERAGE BACKSCATTER CROSS SECTION, M2
C     SIGS   = AVERAGE SCATTER CROSS SECTION, M2
C
      COMMON /TEST/ NPG,ABAR(11),SIGB(10),SIGE(10),SIGS(10)
C
C     INITITALIZE VARIABLES FOR COMPUTING AVERAGE BACKSCATTER AND
C     EXTINCTION CROSS SECTIONS
C
      PI=3.1415927
      XLAMDA=3.E4/FREQ
      FX=PI/XLAMDA
      IPG=JGROUP
      IPG1=IPG+1
      A1=ABAR(IPG)
      X=A1*FX
      CALL MISCAT( X, DIECR, DIECI, XKBI, XKEI, XKSI )
      A2=ABAR(IPG1)
      A3=A2**(1.-P)
      A3I=A1**(1.0-P)
      FNP1=(A3I-A3)
      DELTA=A2-A1
      JMAX=MAXO(1,5*IFIX(AMIN1(1.0,(A2/A1)/X)))
      DELTA=DELTA/FLOAT(JMAX)
      SGB=0.
      SGE=0.
      SGS=0.0
      DO 100 J=1,JMAX
      A2=A1+DELTA
      X=A2*FX
      CALL MISCAT( X, DIECR, DIECI, XKB, XKE, XKS )
C
C     COMPUTE POWER LAW APPROXIMATION FOR BACKSCATTER AND EXTINCTION
C     EFFICIENCES
```

```
C
      ALOGA=ALOG(A2/A1)
      XB=ALOG(XKB/XKBI)/ALOGA
      XE=ALOG(XKE/XKEI)/ALOGA
      XS=ALOG(XKS/XKSI)/ALOGA
C
C     COMPUTE SCATTER CROSS SECTION
      X1=XS-P+3.0
      IF( X1 .EQ. 0.0 ) GO TO 2
      SGSJ=XKSI*(EXP(X1*ALOGA)-1.0)/(X1*A1**(P-3.0))
      GO TO 4
    2 SGSJ=XKSI*ALOGA/A1**XS
    4 CONTINUE
C     COMPUTE BACKSCATTER CROSS SECTION
      X1=XB-P+3.
C
      IF(X1)10,20,10
   10 SGBJ=XKBI*(EXP(X1*ALOGA)-1.)/(X1*A1**(P-3.))
      GO TO 40
   20 SGBJ=XKBI*ALOGA/A1**XB
C
C     COMPUTE EXTINCTION CROSS SECTION
C
   40 X1=XE-P+3.
      IF(X1)50,60,50
   50 SGEJ=XKEI*(EXP(X1*ALOGA)-1.)/(X1*A1**(P-3.))
      GO TO 80
   60 SGEJ=XKEI*ALOGA/A1**XE
C         ACCUMULATE CROSS SECTIONS
   80 SGB=SGB+SGBJ
      SGE=SGE+SGEJ
      SGS=SGS+SGSJ
      A1=A2
      XKBI=XKB
      XKEI=XKE
      XKSI=XKS
  100 CONTINUE
C
C     COMPUTE AVERAGE BACKSCATTER AND EXTINCTION CROSS SECTIONS CROSS
C     SECTIONS FER PARTICLE (M**2)
C
      SIGB(IPG)=7.854E-5*(P-1.0)*SGB/FNP1
      SIGE(IPG)=7.854E-5*(P-1.0)*SGE/FNP1
      SIGS(IPG)=7.854E-5*(P-1.0)*SGS/FNP1
      RETURN
      END
```

APPENDIX C
SOLUTION TO CUBIC MIXING RULE EQUATIONS

The two mixing rule equations are (see Section 4)

$$\varepsilon^{*3} - 3\,\varepsilon_d^* \varepsilon^{*2} + (3\,\varepsilon_d^{*2} - C)\varepsilon^* - \varepsilon_d^{*3} = 0 \tag{C-1}$$

$$\varepsilon_m^{*3} - 3\,\varepsilon_d^* \varepsilon_m^{*2} + (3\,\varepsilon_d^{*2} - D)\,\varepsilon_m^* - \varepsilon_d^{*3} = 0 \tag{C-2}$$

where

$$C = \frac{(1-\phi)^3(\varepsilon_m^* - \varepsilon_d^*)^3}{\varepsilon_m^*} \tag{C-3}$$

$$D = \frac{(\varepsilon^* - \varepsilon_d^*)^3}{(1-\phi)^3 \varepsilon_m^*} \quad . \tag{C-4}$$

The cubic equations (C-1 and C-2) can be solved for ε^* and ε_m^*, respectively (the other parameters assumed known) by the standard cubic equation formulas. Some care must be taken because the coefficients are complex. Let

$$z = \begin{cases} \varepsilon^* & \text{for Equation C-1} \\[2mm] \varepsilon_m^* & \text{for Equation C-2} \end{cases} \tag{C-5}$$

$$P = -3\,\varepsilon_d^* \tag{C-6}$$

$$Q = \begin{cases} 3\,\varepsilon_d^{*2} - C & \text{for Equation C-1} \\[2mm] 3\,\varepsilon_d^{*2} - D & \text{for Equation C-2} \end{cases} \tag{C-7}$$

$$R = -\,\varepsilon_d^{*3} \quad . \tag{C-8}$$

Our cubic equations are now in the standard form

$$z^3 + Pz^2 + Qz + R = 0 \tag{C-9}$$

but with all quantities complex. As in the case of real coefficients, define

$$a = \frac{1}{3}\left(3Q - P^2\right) \tag{C-10}$$

$$b = \frac{1}{27}\left(2P^3 - 9PQ + 27R\right) \tag{C-11}$$

$$e = \sqrt{\frac{b^2}{4} + \frac{a^3}{27}} \tag{C-12}$$

$$f = -\frac{1}{2}b + e \tag{C-13}$$

$$g = -\frac{1}{2}b - e \tag{C-14}$$

$$A = f_1, \text{ the first complex root of } (f)^{1/3} \tag{C-15}$$

$$g_1, g_2, g_3 = \text{ three complex roots of } (g)^{1/3} \quad . \tag{C-16}$$

It does not matter which of the two complex roots is taken for e. By convention we take the first root. The three complex roots of f and g are ordered in the following manner. Write

$$f = f_R + if_I = re^{i\theta} , \tag{C-17}$$

where

$$r = \sqrt{f_R^2 + f_I^2} \tag{C-18}$$

$$i = \sqrt{-1}$$

$$-\pi < \theta \leq \pi$$

$f_R, f_I, r,$ and θ are all real quantities.

The three roots of $(f)^{1/3}$ are ordered as

$$f_1 = r^{1/3} e^{i\theta/3} \tag{C-19}$$

$$f_2 = r^{1/3} e^{i(\theta/3 + 2/3\pi)} \tag{C-20}$$

$$f_3 = r^{1/3} e^{i(\theta/3 + 4/3\pi)} \tag{C-21}$$

The three roots of $(g)^{1/3}$ are similarly ordered. Form the three trial solutions,

$$t_1 = A + g_1 \tag{C-22}$$

$$t_2 = A + g_2 \tag{C-23}$$

$$t_3 = A + g_3 \quad . \tag{C-24}$$

Substitute the trial solutions into the reduced complex cubic equation

$$t^3 + at + b = 0 \quad . \tag{C-25}$$

One of the three trial solutions will satisfy the reduced equation. Let B be that value of g_1, g_2, g_3 of the successful trial solution. Then the three complex solutions to the complex cubic Equation C-9 are

$$Z_1 = A + B - \frac{1}{3} P \tag{C-26}$$

$$Z_2 = -\frac{1}{2} (A + B) + \frac{i\sqrt{3}}{2} (A - B) - \frac{1}{3} P \tag{C-27}$$

$$Z_3 = -\frac{1}{2} (A + B) - \frac{i\sqrt{3}}{2} (A - B) - \frac{1}{3} P \quad . \tag{C-28}$$

A computer program has been written to solve Equations C-1 and C-2. The inputs for Equation C-1 are ϵ_d^*, ϵ_m^*, and ϕ; for Equation C-2 the inputs are ϵ_d^*, ϵ^*, and ϕ. The input format is I1,E9.0,4E10.0, and the input parameters are arranged on the data cards as shown below:

Column 1	10	20	30	40	50	60	70	80
1 $\quad Re(\varepsilon_d^*)$	$Im(\varepsilon_d^*)$	$Re(\varepsilon_m^*)$	$Im(\varepsilon_m^*)$	ϕ				
2 $\quad Re(\varepsilon_d^*)$	$Im(\varepsilon_d^*)$	$Re(\varepsilon^*)$	$Im(\varepsilon^*)$	ϕ				

Re ≡ real part of   Im ≡ imaginary part of

The 1 in column 1 indicates that it is Equation C-1 that is to be solved; a 2 in column 1 indicates that Equation C-2 is to be solved. As many cases may be stacked as desired; a blank data card is placed at the end of the data deck to signal end of data. Note that the input for the imaginary parts of the relative permittivities are negative. That is, for

$$\varepsilon_d^* = \varepsilon_d' - i\,\varepsilon_d'' \quad ,$$

then

$$Re(\varepsilon_d^*) = \varepsilon_d' > 0$$

$$Im(\varepsilon_d^*) = -\varepsilon_d'' \le 0 \quad .$$

The output consists of

    1. The input parameters

    2. The real and imaginary parts of P, Q, R of the cubic Equation C-9

    3. The real and imaginary parts of the complex solutions Z1, Z2, Z3 of Equations C-26, C-27, and C-28

    4. The real and imaginary parts of the square roots of Z1, Z2, Z3.

One of the three solutions Z_1, Z_2, Z_3 is the proper solution for ε^* for Equation C-1, or ε_m^* for Equation C-2. We have arranged the program so that for all cases we have run, the proper solution has been Z_1. It is conceivable that on a different computer or for some special input values, the proper root may not be Z_1. Therefore as a precaution, we print out all three roots. Generally the proper solution is obvious. The proper solution for ε^* or ε_m^* must have a positive real part (ε') and a negative imaginary part ($-\varepsilon''$). Two of the solutions may satisfy the

positive real and negative imaginary criteria, but in our experience
the proper solution is obvious from the magnitudes. The square root of
the relative permittivity is also computed since this is the index of
refraction, which is needed for propagation calculations,

$$m = \sqrt{\epsilon^*} \quad . \tag{C-29}$$

Note that m is normally written

$$m = m_R - im_I \quad , \tag{C-30}$$

so that

$$m_R = \text{Re}(m) \tag{C-31}$$

$$m_I = -\text{Im}(m) \quad . \tag{C-32}$$

As in the case of ϵ^* and ϵ_m^*, the output for m has a positive real part
and a negative imaginary part.

The listing of the computer program follows. The program consists
of a driver routine and the two routines which solve the complex cubic
Equation C-9. The complex cubic equation routines are general routines
which can be separated from the mixing rule driver and used to solve any
complex cubic equation.

111

```
C       THIS IS THE DRIVER ROUTINE FOR THE COMPLEX CUBIC MIXING RULE
C
C
C       DOCUMENTATION IS GIVEN IN APPENDIX C OF
C               DUST CLOUD MODELING AND PROPAGATION EFFECTS
C               FOR RADAR AND COMMUNICATIONS CODES
C               GE78TMP-81 OCTOBER 1978
C               BY JAMES H THOMPSON, GENERAL ELECTRIC - TEMPO
C
C
        COMPLEX E, FM, ED, C, D, P, Q, R, Z1, Z2, Z3
C
C       ITAPE IS THE INPUT TAPE NUMBER, JTAPE IS THE OUTPUT TAPE NUMBER.
C       THE VALUES HAVE BEEN SET AT ITAPE = 5 AND JTAPE = 6 BUT THESE CAN
C       BE CHANGED FOR ANY COMPUTER BY RESETTING THE FOLLOWING ITAPE AND
C       JTAPE STATEMENTS
        ITAPE = 5
        JTAPE = 6
C
C
C       READ INPUT FOR FIRST CASE
   10   READ( ITAPE, 11 ) MODE, XR1, XI1, XR2, XI2, PHI
   11   FORMAT( I1, F9.0, 4E10.0 )
C
C       CHECK IF ALL CASES HAVE BEEN RUN
        IF( MODE .LE. 0 ) STOP
C
C       SET VALUE OF ED
        ED = CMPLX( XR1, XI1 )
C
C       CHECK WHICH EQUATION IS TO BE SOLVED, C-1 OR C-2
        IF( MODE .EQ. 2 ) GO TO 20
C
C
C       EQUATION C-1 IS TO BE SOLVED
        FM = CMPLX( XR2, XI2 )
        C = ( 1.0 - PHI )**3 * ( FM - ED )**3 / FM
        Q = 3. * ED**2 - C
        GO TO 30
C
C
C       EQUATION C-2 IS TO BE SOLVED
   20   E = CMPLX( XR2, XI2 )
        D = ( E - ED )**3 / ( ( 1. - PHI )**3 * E )
        Q = 3. * ED**2 - D
C
C
   30   P = -3. * ED
        R = -ED**3
C
        CALL CCUBIC( P,Q,R,Z1,Z2,Z3 )
C
```

112

```
C     WRITE OUT INPUT, R-G-H VALUES, AND THE THREE COMPLEX ROOTS TO THE
C     MIXING RULE EQUATION
      IF( MODE .EQ. 2 ) GO TO 50
C
      WRITE( JTAPE, 40 ) MODE, XR1, XI1, XR2, XI2, PHI
   40 FORMAT(1H0,81HEW INDEX       REAL(FD)   IMAGINARY(FD)      REAL(FM)
     1IMAGINARY(FM) VOLUME FRACTION /
     21H ,I5,3X,1P5E14.3)
      GO TO 60
C
   50 WRITE( JTAPE, 51 ) MODE, XR1, XI1, XR2, XI2, PHI
   51 FORMAT(1H0,81HED INDEX       REAL(FD)   IMAGINARY(FD)       REAL(F)
     1IMAGINARY(F)  VOLUME FRACTION /
     21H ,I5,3X,1P5E14.3)
C
   60 WRITE( JTAPE, 61 ) P, Q, R
   61 FORMAT(1H0,55H                         STANDARD CUBIC EQUATION COEFFICIE
     1NTS /
     21H ,72H    REAL(P)  IMAGINARY(P)    REAL(Q)   IMAGINARY(Q)    REAL(R)
     3 IMAGINARY(R) /
     41H ,1P6E14.3)
C
      IF( MODE .EQ. 2 ) GO TO 80
      WRITE( JTAPE, 70 ) Z1, Z2, Z3
   70 FORMAT(1H0,76H                         THREE ROOTS OF COMPLEX CUBIC
     1MIXING RULE EQUATION F-1 /
     21H ,85H    (1) REAL(F)  IMAGINARY(F)   (2) REAL(F)  IMAGINARY(F)
     3 (3) REAL(F)  IMAGINARY(F) /
     21H ,1P6E14.3)
      GO TO 90
C
   80 WRITE( JTAPE, 81 ) Z1, Z2, Z3
   81 FORMAT(1H0,76H                         THREE ROOTS OF COMPLEX CUBIC
     1MIXING RULE EQUATION F-2 /
     21H ,85H    (1) REAL(FM) IMAGINARY(FM)  (2) REAL(FM) IMAGINARY(FM)
     3(3) REAL(FM) IMAGINARY(FM) /
     41H ,1P6E14.3)
C
C     COMPUTE INDEX OF REFRACTION
   90 Z1=CSQRT(Z1)
      Z2=CSQRT(Z2)
      Z3=CSQRT(Z3)
C
      WRITE( JTAPE, 91 ) Z1, Z2, Z3
   91 FORMAT(1H0,51H                              INDEX OF REFRACTION/
     21H ,85H    (1) REAL(M)  IMAGINARY(M)   (2) REAL(M)  IMAGINARY(M)
     3 (3) REAL(M)  IMAGINARY(M) /
     31H ,1P6E14.3////)
C
C
      GO TO 10
C
      END
```

```fortran
      SUBROUTINE CCUBIC( P,Q,S,Z1,Z2,Z3 )
C
C     THIS ROUTINE CALCULATES THE THREE ROOTS OF A CUBIC EQUATION WITH
C     COMPLEX COEFFICIENTS
C
C     THE CUBIC EQUATION IS ASSUMED TO BE OF THE FORM
C     Z**3+P*Z**2+Q*Z+S=0
C
C
C     INPUTS
C     P  = CONSTANT COMPLEX COEFFICIENT MULTIPLYING Z**2
C     Q  = CONSTANT COMPLEX COEFFICIENT MULTIPLYING Z
C     S  = CONSTANT COMPLEX COEFFICIENT
C
C     OUTPUTS
C     Z1 = FIRST COMPLEX ROOT
C     Z2 = SECOND COMPLEX ROOT
C     Z3 = THIRD COMPLEX ROOT
C
C
      COMPLEX P,Q,S,Z1,Z2,Z3,A,B,C,D,E,F,T
C
      A=(3.0*Q-P*P)/3.0
      B=(2.0*P*P*P-9.0*P*Q+27.0*S)/27.0
      E=CSQRT(B*B/4.0+A*A*A/27.0)
      F=-B/2.0+E
      X=REAL(F)
      Y=AIMAG(F)
      CALL POLAR( X,Y,R,THETA )
      R=R**(1./3.)
      THETA=THETA/3.0
      C=CMPLX( R*COS(THETA), R*SIN(THETA) )
      F=-B/2.0-E
      X=REAL(F)
      Y=AIMAG(F)
      CALL POLAR( X,Y,R,THETA )
      R=R**(1./3.)
      THETA=THETA/3.0
      D=CMPLX( R*COS(THETA), R*SIN(THETA) )
      Z1=C+D
      T=Z1*Z1*Z1+A*Z1+B
      IF( CABS(T) .LT. 1.E-3*AMAX1( CABS(A*Z1) , CABS(B) ) ) GO TO 10
      PI23=8.0*ATAN(1.0)/3.0
      D=CMPLX( R*COS(THETA+PI23) , R*SIN(THETA+PI23) )
      Z1=C+D
      T=Z1*Z1*Z1+A*Z1+B
      IF( CABS(T) .LT. 1.E-3*AMAX1( CABS(A*Z1) , CABS(B) ) ) GO TO 10
      PI43=2.0*PI23
      D=CMPLX( R*COS(THETA+PI43) , R*SIN(THETA+PI43) )
      Z1=C+D
      T=Z1*Z1*Z1+A*Z1+B
      IF( CABS(T) .LT. 1.E-3*AMAX1( CABS(A*Z1) , CABS(B) ) ) GO TO 10
```

```fortran
      WRITE(6,5)
    5 FORMAT(39H NO PROPER SOLUTION FOUND FOR THIS CASE)
   10 F=CMPLX( 0.0, SQRT(3.0) )*(C-D)/2.0
      Z2=-Z1/2.0 +F -P/3.0
      Z3=-Z1/2.0 -F -P/3.0
      Z1=Z1-P/3.0
      RETURN
      END
```

```
      SUBROUTINE POLAR( X,Y,R,THETA )
C
C     THIS ROUTINE CONVERTS A COMPLEX NUMBER FROM RECTANGULAR(Z=X+IY)
C     TO POLAR(Z=R*EXP(I*THETA) ) NOTATION
C
C
C     INPUTS
C     X      = REAL PART OF COMPLEX NUMBER
C     Y      = IMAGINARY PART OF COMPLEX NUMBER
C
C     OUTPUTS
C     R      = ABSOLUTE MAGNITUDE OF COMPLEX NUMBER
C     THETA = POLAR ANGLE OF COMPLEX NUMBER(RADIANS)
C             THETA IS BETWEEN -PI AND +PI
C
C
      R=SQRT( X**2 + Y**2 )
      IF( X .EQ. 0.0 ) GO TO 10
      IF( ABS(Y) .GT. ABS(1.E12*X) ) GO TO 10
      THETA=ATAN(Y/X)
      IF( X .GE. 0.0 ) RETURN
      THETA=THETA+SIGN(1.0,Y)*4.0*ATAN(1.0)
      RETURN
   10 THETA=2.0*ATAN(1.0)
      IF( Y .LT. 0.0 ) THETA=-THETA
      RETURN
      END
```

DISTRIBUTION LIST

DEPARTMENT OF DEFENSE

Assistant Secretary of Defense
Comm, Cmd, Cont & Intell
    ATTN: J. Babcock
    ATTN: M. Epstein

Assistant to the Secretary of Defense
Atomic Energy
    ATTN: Executive Assistant

Command & Control Technical Center
Department of Defense
    ATTN: C-312, R. Mason
    ATTN: C-650, G. Jones
    ATTN: C-650, W. Heidig

Defense Advanced Rsch Proj Agency
    ATTN: TIO

Defense Communications Agency
    ATTN: Code R1033, M. Raffensperger
    ATTN: Code 101B
    ATTN: Code 810, J. Barna
    ATTN: Code 480
    ATTN: Code 205

Defense Communications Engineer Center
    ATTN: Code R720, J. Worthington
    ATTN: Code R410, J. McLean
    ATTN: Code R123

Defense Documentation Center
12 cy ATTN: DD

Defense Intelligence Agency
    ATTN: DT-1B7, R. Morton
    ATTN: HQ-TR, J. Stewart
    ATTN: DC-7D, W. Wittig
    ATTN: DT-1B
    ATTN: RT-5
    ATTN: DB, A. Wise
    ATTN: DB-4C, E. O'Farrell

Defense Nuclear Agency
    ATTN: DDST
    ATTN: STVL
4 cy ATTN: TITL
3 cy ATTN: RAAE
2 cy ATTN: SPAS

Field Command
Defense Nuclear Agency
    ATTN: FCPR

Field Command
Defense Nuclear Agency
Livermore Division
    ATTN: FCPRL

Interservice Nuclear Weapons School
    ATTN: TTV

Joint Chiefs of Staff
    ATTN: J-3, WWMCCS Evaluation Office

DEPARTMENT OF DEFENSE (Continued)

Joint Strat Tgt Planning Staff
    ATTN: JLTW-2

National Security Agency
    ATTN: W32, O. Bartlett
    ATTN: R52, J. Skillman
    ATTN: B3, F. Leonard

Under Secy of Def for Rsch & Engrg
    ATTN: Strategic & Space Systems (OS)

WWMCCS System Engineering Org
    ATTN: T. Neighbors
    ATTN: R. Crawford

DEPARTMENT OF THE ARMY

Atmospheric Sciences Laboratory
U.S. Army Electronics R & D Command
    ATTN: DELAS-EO, F. Niles
    ATTN: DELAS-AS, H. Holt

BMD Advanced Technology Center
Department of the Army
    ATTN: ATC-T, M. Capps
    ATTN: ATC-O, W. Davies
    ATTN: ATC-R, D. Russ

BMD Systems Command
Department of the Army
2 cy ATTN: BMDSC-HW

Electronics Tech & Devices Lab
U.S. Army Electronics R & D Command
    ATTN: DELET-ER, H. Bomke

Harry Diamond Laboratories
Department of the Army
    ATTN: DELHD-N-RB, R. Williams
    ATTN: DELHD-N-P, F. Wimenitz
    ATTN: DELHD-I-TL, M. Weiner
2 cy ATTN: DELHD-N-P

U.S. Army Comm-Elec Engrg Instal Agency
    ATTN: CCC-EMEO, W. Nair
    ATTN: CCC-EMEO-PED, G. Lane

U.S. Army Communications Command
    ATTN: CC-OPS-WR, H. Wilson

U.S. Army Foreign Science & Tech Ctr
    ATTN: DRXST-SD

U.S. Army Materiel Dev & Readiness Cmd
    ATTN: DRCLDC, J. Bender

U.S. Army Missile Intelligence Agency
    ATTN: J. Gamble

U.S. Army Missile R & D Command
    ATTN: Redstone Scientific Info Ctr

U.S. Army Nuclear & Chemical Agency
    ATTN: Library

117

DEPARTMENT OF THE ARMY (Continued)

U.S. Army Satellite Comm Agency
    ATTN: Document Control

U.S. Army TRADOC Systems Analysis Activity
    ATTN: ATAA-PT
    ATTN: ATAA-TCC, F. Payan, Jr.

DEPARTMENT OF THE NAVY

Naval Electronic Systems Command
    ATTN: Code 501A
    ATTN: PME 117
    ATTN: PME 117-T
    ATTN: NAVELEX 3101, T. Hughes
    ATTN: Code 5011

Naval Intelligence Support Center
    ATTN: NISC-50

Naval Ocean Systems Center
    ATTN: M. Paulson
    ATTN: Code 4151, C. Baggett
3 cy ATTN: Code 5324, W. Moler

Naval Research Laboratory
    ATTN: Code 2627
    ATTN: Code 7555
    ATTN: Code 7551
    ATTN: Code 7580
    ATTN: Code 7500, B. Wald
    ATTN: Code 6700, T. Coffey
    ATTN: Code 6707, J. Davis
    ATTN: Code 6730, E. McClean
    ATTN: Code 6701, J. Brown

Naval Space Surveillance System
    ATTN: J. Burton

Naval Surface Weapons Center
    ATTN: Code F31

Naval Surface Weapons Center
    ATTN: Code F-14, R. Butler

Office of Naval Research
    ATTN: Code 465
    ATTN: Code 420
    ATTN: Code 421

Office of the Chief of Naval Operations
    ATTN: OP 604
    ATTN: OP 941D

Strategic Systems Project Office
Department of the Navy
    ATTN: NSSP-2722, F. Wimberly
    ATTN: NSP-2141
    ATTN: NS-43

DEPARTMENT OF THE AIR FORCE

Aerospace Defense Command
    ATTN: DC, Mr. Long

Aerospace Defense Command
    ATTN: XP
    ATTN: XPDQ

DEPARTMENT OF THE AIR FORCE (Continued)

Air Force Avionics Laboratory
    ATTN: AAD
    ATTN: AAD, A. Johnson

Air Force Geophysics Laboratory
    ATTN: OPR-1, J. Ulwick
    ATTN: OPR, H. Gardiner
    ATTN: LKB, K. Champion
    ATTN: OPR, A. Stair
    ATTN: PHP, J. Aarons
    ATTN: PHI, J. Buchau
    ATTN: PHP, J. Mullen

Air Force Weapons Laboratory
    ATTN: DYC, J. Barry
    ATTN: CA
    ATTN: DES, G. Ganong
    ATTN: DYC, J. Frasier
    ATTN: SUL
    ATTN: DYC, J. Kamm
    ATTN: DES, C. Needham

Air Logistics Command
    ATTN: OO-ALC/MM, R. Blackburn

Assistant Chief of Staff
Intelligence
Department of the Air Force
    ATTN: INED

Deputy Chief of Staff
Operations Plans and Readiness
Department of the Air Force
    ATTN: AFXOXED
    ATTN: AFXOKCD

Deputy Chief of Staff
Research, Development, & Acq
Department of the Air Force
    ATTN: AFRDQ
    ATTN: AFRDSS
    ATTN: AFRDSP

Deputy Chief of Staff
Studies & Analysis
Department of the Air Force
    ATTN: SASC, R. Paul

Electronic Systems Division, AFSC
    ATTN: YSEA
    ATTN: XRW, J. Deas
    ATTN: DCKC, J. Clark

Foreign Technology Division, AFSC
    ATTN: TQTD, B. Ballard
    ATTN: NIIS, Library

Rome Air Development Center, AFSC
    ATTN: OCS, V. Coyne
    ATTN: Documents Library/TSLD

Rome Air Development Center, AFSC
    ATTN: EEP

Space & Missile Systems Organization
Air Force Systems Command
    ATTN: RSP

DEPARTMENT OF THE AIR FORCE (Continued)

Space & Missile Systems Organization
Air Force Systems Command
 ATTN: MNNL, S. Kennedy
 ATTN: MNX

Space & Missile Systems Organization
Air Force Systems Command
 ATTN: SKA, M. Clavin
 ATTN: SKA, C. Rightmyer

Space & Missile Systems Organization
Air Force Systems Command
 ATTN: SZJ
 ATTN: SZJ, L. Doan

Strategic Air Command
 ATTN: DCX, Chief Scientist
 ATTN: ADWATE, B. Bauer
 ATTN: NRT
 ATTN: XPFS
 ATTN: XPFS, B. Stephan
 ATTN: OOKSN

DEPARTMENT OF ENERGY

Department of Energy
 ATTN: D. Sherwood

Department of Energy
 ATTN: A. Labowitz

DEPARTMENT OF ENERGY CONTRACTORS

Lawrence Livermore Laboratory
University of California
 ATTN: L-96, T. Donich
 ATTN: L-389, R. Ott
 ATTN: L-31, R. Hager
 ATTN: Technical Information Dept Library

Los Alamos Scientific Laboratory
 ATTN: F. Jones
 ATTN: J. Zinn
 ATTN: R. Taschek
 ATTN: P. Keaton
 ATTN: J. Malik
 ATTN: D. Westervelt

Sandia Laboratories
Livermore Laboratory
 ATTN: B. Murphey
 ATTN: T. Cook

Sandia Laboratories
 ATTN: Space Project Division
 ATTN: 3141
 ATTN: D. Thornbrough
 ATTN: T. Wright
 ATTN: W. Brown
 ATTN: C. Williams
 ATTN: D. Dahlgren
 ATTN: C. Mehl

OTHER GOVERNMENT AGENCIES

Central Intelligence Agency
 ATTN: OSI/PSID

OTHER GOVERNMENT AGENCIES (Continued)

Department of Commerce
National Bureau of Standards
 ATTN: R. Moore

Department of Commerce
National Oceanic & Atmospheric Admin
Environmental Research Laboratories
 ATTN: D. Williams
 ATTN: R. Grubb
 ATTN: Aeronomy Lab, G. Reid

Department of Transportation
Office of the Secretary
 ATTN: R. Lewis
 ATTN: R. Doherty

Institute for Telecommunications Sciences
National Telecommunications & Info Admin
 ATTN: A. Jean
 ATTN: D. Crombie
 ATTN: W. Utlaut
 ATTN: L. Berry

DEPARTMENT OF DEFENSE CONTRACTORS

Aerospace Corp.
 ATTN: F. Morse
 ATTN: N. Stockwell
 ATTN: A. Morse
 ATTN: G. Anderson
 ATTN: W. Grabowsky
 ATTN: V. Josephson
 ATTN: T. Salmi
 ATTN: D. Olsen
 ATTN: I. Garfunkel
 ATTN: J. Carter
 ATTN: P. Slaughter
 ATTN: S. Bower

Analytical Systems Engineering Corp.
 ATTN: Radio Sciences

Berkeley Research Associates, Inc.
 ATTN: J. Workman

Boeing Co.
 ATTN: D. Murray
 ATTN: G. Hall
 ATTN: S. Tashird
 ATTN: J. Kenney
 ATTN: G. Keister

University of California at San Diego
 ATTN: H. Booker

Charles Stark Draper Lab, Inc.
 ATTN: D. Cox
 ATTN: J. Gilmore

Computer Sciences Corp.
 ATTN: H. Blank

Comsat Labs
 ATTN: G. Hyde
 ATTN: R. Taur

Cornell University
Department of Electrical Engineering
 ATTN: D. Farley, Jr.

119

DEPARTMENT OF DEFENSE CONTRACTORS (Continued)

EG&G, Inc.
    ATTN: J. Fu
    ATTN: J. Breedlove
    ATTN: J. Walker

Electrospace Systems, Inc.
    ATTN: P. Phillips
    ATTN: H. Logston

ESL, Inc.
    ATTN: J. Marshall
    ATTN: J. Roberts
    ATTN: C. Prettie

Ford Aerospace & Communications Corp.
    ATTN: J. Mattingley

General Electric Co.
Space Division
    ATTN: M. Bortner
    ATTN: R. Edsall

General Electric Co.
    ATTN: G. Millman
    ATTN: F. Reibert

General Electric Company-TEMPO
Center for Advanced Studies
    ATTN: W. McNamara
    ATTN: M. Stanton
    ATTN: D. Chandler
    ATTN: DASIAC
    ATTN: W. Knapp
    ATTN: T. Stevens
    ATTN: J. Thompson

General Electric Tech Services Co., Inc.
HHMES
    ATTN: G. Millman

General Research Corp.
    ATTN: J. Garbarino
    ATTN: J. Ise, Jr.

Geophysical Institute
University of Alaska
    ATTN: N. Brown
    ATTN: Technical Library
    ATTN: T. Davis

GTE Sylvania, Inc.
Electronics Systems Grp-Eastern Div
    ATTN: M. Cross

HSS, Inc.
    ATTN: D. Hansen

University of Illinois
    ATTN: K. Yeh

Information Science, Inc.
    ATTN: W. Dudziak

Institute for Defense Analyses
    ATTN: E. Bauer
    ATTN: J. Bengston
    ATTN: H. Wolfhard
    ATTN: J. Aein

DEPARTMENT OF DEFENSE CONTRACTORS (Continued)

International Tel & Telegraph Corp.
    ATTN: Technical Library

Jaycor
    ATTN: S. Goldman

Johns Hopkins University
Applied Physics Lab
    ATTN: T. Evans
    ATTN: T. Potemra
    ATTN: Document Librarian
    ATTN: J. Newland
    ATTN: P. Komiske

Kaman Sciences Corp.
    ATTN: F. Foxwell
    ATTN: T. Meagher
    ATTN: N. Beauchamp

Linkabit Corp.
    ATTN: I. Jacobs

Litton Systems, Inc.
Amecom Division
    ATTN: R. Grasty

Lockheed Missiles & Space Co., Inc.
    ATTN: D. Churchill
    ATTN: Dept 60-12

Lockheed Missiles & Space Co., Inc.
    ATTN: R. Johnson
    ATTN: M. Walt
    ATTN: W. Imhof
    ATTN: B. Au

M.I.T. Lincoln Lab
    ATTN: L. Loughlin
    ATTN: J. Evans
    ATTN: D. Towle

Martin Marietta Corp.
    ATTN: R. Heffner

McDonnell Douglas Corp.
    ATTN: N. Harris
    ATTN: R. Halprin
    ATTN: G. Mroz
    ATTN: J. Moule
    ATTN: W. Olson

Mission Research Corp.
    ATTN: R. Bigoni
    ATTN: M. Scheibe
    ATTN: D. Sappenfield
    ATTN: D. Crevier
    ATTN: R. Fischer
    ATTN: C. Lytsche
    ATTN: R. Hendrick
    ATTN: D. Sappenfield
    ATTN: C. Longmire
    ATTN: F. Fajen
    ATTN: R. Bogusch
    ATTN: D. Towle

Mitre Corp.
    ATTN: C. Callahan
    ATTN: G. Harding
    ATTN: T. Horwath

DEPARTMENT OF DEFENSE CONTRACTORS (Continued)

Mitre Corp.
    ATTN: A. Hall
    ATTN: J. Wheeler
    ATTN: A. Foster
    ATTN: M. Horrocks

Pacific-Sierra Research Corp.
    ATTN: E. Field, Jr.

Pennsylvania State University
Ionosphere Research Lab
    ATTN: Ionospheric Research Lab

Photometrics, Inc.
    ATTN: I. Kofsky

Physical Dynamics, Inc.
    ATTN: A. Thompson

Physical Dynamics, Inc.
    ATTN: E. Fremouw

R & D Associates
    ATTN: F. Greifinger
    ATTN: B. Gabbard
    ATTN: J. MacDonald
    ATTN: H. Ory
    ATTN: P. Gilmore
    ATTN: R. Lelevier
    ATTN: R. Turco
    ATTN: A. Karzas
    ATTN: W. Wright, Jr.

Rand Corp.
    ATTN: E. Bedrozian
    ATTN: C. Crain

Raytheon Co.
    ATTN: G. Thome

Riverside Research Institute
    ATTN: V. Trapani

Science Applications, Inc.
    ATTN: R. Lee
    ATTN: J. McDougall
    ATTN: L. Linson
    ATTN: E. Straker
    ATTN: D. Hamlin
    ATTN: C. Smith
    ATTN: D. Sachs

Science Applications, Inc.
    ATTN: D. Divis

Science Applications, Inc.
    ATTN: SZ

Science Applications, Inc.
    ATTN: J. Cockayne

DEPARTMENT OF DEFENSE CONTRACTORS (Continued)

Space Data Corp.
    ATTN: E. Allen

SRI International
    ATTN: R. Livingston
    ATTN: M. Baron
    ATTN: R. Leadabrand
    ATTN: R. Leonard
    ATTN: W. Chesnut
    ATTN: W. Jaye
    ATTN: J. Depp
    ATTN: G. Smith
    ATTN: A. Burns
    ATTN: G. Price
    ATTN: C. Rino
    ATTN: G. Carpenter
    ATTN: D. Neilson

SRI International
    ATTN: F. Perkins

Technology International Corp.
    ATTN: W. Boquist

Teledyne Brown Engineering
    ATTN: R. Deliberis
    ATTN: N. Passino

Tri-Com, Inc.
    ATTN: D. Murray

TRW Defense & Space Systems Group
    ATTN: S. Altschuler
    ATTN: R. Plebuch
    ATTN: D. Dee

Utah State University
Contract/Grant Office
Space Science Lab
    ATTN: K. Baker
    ATTN: L. Jensen

Visidyne, Inc.
    ATTN: C. Humphrey
    ATTN: J. Carpenter